# Study on Water Film Cooling for PWR's Passive Containment Cooling System

Zur Erlangung des akademischen Grades
**Doktor der Ingenieurwissenschaften**
der Fakultät für Maschinenbau
Karlsruher Institut für Technologie (KIT)

genehmigte
**Dissertation**
von

M.Sc. Xi Huang aus
Chengdu, VR. China

Tag der mündlichen Prüfung: 10. September 2015

Hauptreferent: Prof. Dr.-Ing. Xu Cheng

Korreferent: Prof. Dr.-Ing. Thomas Schulenberg

Karlsruher Institut für Technologie (KIT)
Institut für Fusionstechnologie und Reaktortechnik (IFRT)
Institut für Kern- und Energietechnik (IKET)

# *Eidesstattliche Erklärung*

Hiermit erkläre ich, dass ich die vorliegende Arbeit selbständig angefertigt und keine anderen als die angegebenen Quellen und Hilfsmittel benutzt sowie die wörtlich und inhaltlich übernommenen Stellen als solche kenntlich gemacht und die Satzung des Karlsruher Institutes für Technologie (KIT) zur Sicherung guter wissenschaftlicher Praxis in der jeweils gültigen Fassung beachtet habe.

Karlsruhe, 01. Juli 2015

Xi Huang

# *Acknowledgements*

# Abstract

Falling water film has been employed for the passive containment cooling of Generation III pressurized water reactor designs. In the thesis the characteristics and evolutionary process of falling liquid film have been investigated.

By reviewing the literature studying the features and phenomena of falling liquid film, the behavior of the film on the containment exterior surface is subdivided into several stages. Thereafter, models simulating each stage are proposed and evaluated. Accordingly, a new integrated water film model is developed and presented in the thesis. The new model considers different flow regimes of falling liquid as it flows downward and is being evaporated. The integrated model has been adapted to the lumped parameter code and then implemented into the containment code COCOSYS, which can simulate plant states during design basis accidents as well as severe accidents in the containment of light water reactors.

This new model enables the containment code to capture phenomena which are not considered before, including: The behavior of film breakup due to the mass reduction, which is predicted on the basis of minimum total energy principle; the formation of rivulets, which is determined according to the assumptions of the rivulet configuration and mass/energy equilibrium; the change of coverage rate and the development of rivulets, which is modeled based on the experimental observations and empirical correlations; the change of the velocity distribution as well as film thickness by considering the interfacial shear stress created by the countercurrent air imposed on the film surface; the processes of hysteresis of rivulets, i.e., the process of advancing and retreating, involving the change of contact angles.

The new model is validated in the current work stage by stage against existing test results and experimental observations. It is revealed that the film thickness with and without countercurrent air calculated by the new model agrees well with the experimental data; the critical thickness of falling film calculated with the new model is also in accordance with the test results; the rivulet behavior calculated with new model, even though is not validated quantitatively, matches

well with the descriptions of the rivulet behavior in the experimental studies.

The developed water film model in COCOSYS is then assessed based on simple test nodalizations. The expected phenomena are obtained in these test cases thus ensure the applicability of the integrated new water film model.

Finally, the new model is applied to evaluate the performance of PCCS film cooling employed in the AP1000 containment with different nodalization strategies and in the Generic containment. The new model also helps optimize the water flow rate of PCCS over time enhancing the cooling capability of the cooling approach.

It is concluded that the original film model tends to underestimate the pressure loads due to the absence of film breakup, rivulets and shear stress model. The coverage rate, as a new factor, can be captured in the new model. It limits the evaporation rate and therefore restricts the cooling efficiency of the falling film. The sensitivity analyses reveal that the contact angle and hysteresis phenomenon, which are not considered in the original version of the code, play significant roles in PCCS film cooling. The advancing contact angle of the rivulets is a decisive factor for the peak pressure while the retreating contact angle is influential in the long term cooling.

The results of sensitivity studies also suggest that the cooling efficiency of PCCS can be optimized by increasing the PCCS injection rate initially and reducing the flow rate during the late phase without changing the water inventory in the PCCS storage tank.

It can be inferred according to the study that the ideal situation for PCCS cooling is that the water film is reaching the bottom and is approaching the complete dry out at the bottom of the containment. The newly developed liquid film model helps to improve the accuracy and reliability of the simulation results.

# Catalogue

# List of Figures

**IV**

VI

# List of Tables

# Nomenclature

$a$        Semi width of circular arc part of rivulet ($m$)

$b$        Width of film sheet part of rivulet ($m$)

$D_h$        Hydraulic diameter of the channel ($m$)

$E$        Energy ($J$)

$f$        Drag force factor used to calculate shear stress at liquid/gas interface (-)

$g$        Gravity acceleration ($m \cdot s^{-2}$)

$M$        Mass flow rate per unit width ($kg \cdot m^{-1} \cdot s^{-1}$)

$m$        Evaporation rate ($kg \cdot m^{-2} \cdot s^{-1}$)

$p$        Pressure ($Pa$)

$R$        Radius of the circular segment of rivulet ($m$)

Re        Reynolds number (-)

$\mathrm{Re}_r$        Reynolds number dependent on the mean velocity (-)

$t$        Time ($s$)

$T$        Temperature ($K$)

$U^*$        Dimensionless velocity ($= uv_l / \left[ \mathrm{g}\left(15\mu_l^2 \sigma / (\rho_l^3 \mathrm{g}^2)\right)^{0.4} \right]$) (-)

$u$        Velocity ($ms^{-1}$)

$V_{r,mean}$        Dimensionless average velocity ($V_{r,mean} = u_{r,mean}\mu_l / (\rho_l \mathrm{g}\delta_r^2)$) (-)

$z$        Length of the wall structure ($m$)

**Greek symbols**

$\alpha$        Film coverage rate ($\alpha = (2a+b)/(2a+b+\lambda)$) (-)

| $\beta$ | Mass transfer coefficient (-) |
|---|---|
| $\gamma$ | Inclination of the substrate (°) |
| $\delta$ | Liquid film thickness / liquid rivulet height ($m$) |
| $\mu$ | Dynamic viscosity ($N \cdot s \cdot m^{-2}$) |
| $\mu_R$ | Reference liquid viscosity ($N \cdot s \cdot m^{-2}$) |
| $\nu$ | Kinematic viscosity ($m^2 s^{-1}$) |
| $\rho$ | Density ($kg \cdot m^{-3}$) |
| $\phi$ | Profile of rivulet / film ($m$) |
| $\tau$ | Shear stress ($Pa$) |
| $\Delta$ | Dimensionless film thickness for critical state ($= \delta / \left[ 15\mu_l^2 \sigma / (\rho_l^3 g^2) \right]^{0.2}$) (-) |
| $\Delta_2$ | Dimensionless film thickness ($\Delta_2 = \delta \left( \rho_l^2 g \sin\gamma / \mu_l^2 \right)^{1/3}$) (-) |
| $\Gamma$ | Dimensionless flow rate per unit width ($= M / \left[ \rho_l \mu_l \sigma^3 / g \right]^{0.2}$) (-) |
| $\theta$ | Contact angle between liquid and substrate (°) |
| $\sigma$ | Surface tension ($N/m$) |
| $\lambda$ | Width of dry patch ($m$) |
| $\lambda_{Film}$ | Thermal conductivity of liquid film ($W / (m \cdot K)$) |

**Subscripts**

| $arc$ | Circular part of the rivulet |
|---|---|
| $A$ | Advancing |
| $crit$ | Critical |
| $l$ | Liquid |
| $f$ | Film |
| $g$ | Gas |
| $i$ | Interface between liquid and gas |

**X**

| | |
|---|---|
| *k* | Kinetic |
| *r* | Rivulet |
| *r,crit* | At the critical state of rivulet |
| *R* | Retreating |
| *s* | Solid |
| *sat* | Saturated |
| *sheet* | Film sheet |
| *sur* | Film surface |
| *tot* | Total |

**Abbreviations**

| | |
|---|---|
| ADS | Automatic Depressurization System |
| COCOSYS | German COntainment COde SYStem |
| CFD | Computational Fluid Dynamics |
| FB | Force Balance |
| GRS | Gesellschaft für Anlagen- und Reaktorsicherheit |
| L-P | Lumped-Parameter |
| MTE | Minimum Total Energy |
| PCCS | Passive Containment Cooling System |
| PXS | Passive Core Cooling System |
| SG | Steam Generator |
| SNL | Sandia National Laboratories |
| PCCWST | Passive Containment Cooling Water Storage Tank |

# 1  OVERVIEW

## 1.1  Motivation

The Generation III nuclear reactor designs have incorporated evolutionary improvements featured by upgraded safety standards and economic efficiency. Passive safety or inherent safety features are highlighted as well. These safety features of nuclear reactors require no operational intervention or electronic feedback so as to avoid accidents and shut down the reactor safely in the event of particular types of emergency. The accident mitigation measures may rely on physical phenomena such as pressure difference, gravity drive and natural convection [1].

One of the representative designs of Generation III nuclear power plants is AP1000, which is designed by Westinghouse Electric Company in accordance with the concept of passive nuclear safety. Currently several reactors of this type are under construction. AP1000 is a progressive design based on AP600 with similar design concepts and with increased power [2]. The layout of the plant is demonstrated in Fig. 1-1.
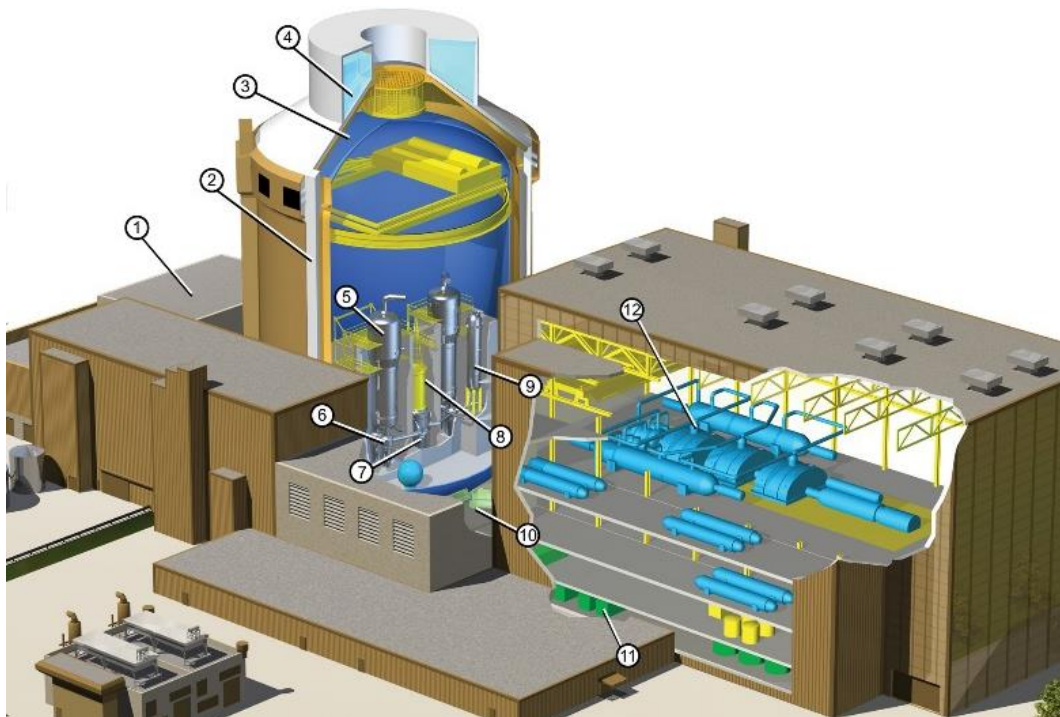


*Fig. 1-1 Layout of the AP 1000 reactor plant [3]*

1. Fuel handling area
2. Concrete shield building
3. Steel containment

**1**

4. Passive containment cooling water tank
5. Steam generator
6. Reactor cooling pumps
7. Reactor vessel
8. Integrated heat package
9. Pressurizer
10. Main control room
11. Feed water pumps
12. Turbine generator

The AP1000 nuclear power plant is a two-loop pressurized water reactor (PWR) and its passive safety systems mainly include Passive Core Cooling System (PXS), passive safety injections with different water storage tanks, passive residual heat removal, Automatic Depressurization System (ADS) and Passive Containment Cooling System (PCCS) [4].

Among which PCCS plays a critical role in nuclear reactor accidents and is the final barrier to prevent radioactive release. The PCCS is designed to maintain containment pressure below the design limit for at least 72 hours without action by the reactor operators [5].

The containment system of AP1000 has applied steel containment and concrete shield building surrounding it. The major components of the passive containment cooling system include: the passive containment cooling water storage tank, which is placed above the containment steel vessel and filled with demineralized water; the water distribution system installed on the exterior surface of the steel containment vessel in order to distribute and balance the water flow at different regions on the containment; the air flow path used to direct vapor and air along the exterior surface of the steel containment shell; the passive containment cooling ancillary water storage tank located at ground level used for makeup to the PCCS water storage tank and the spent fuel pool [4].

During the accidents, steam is released and comes in contact with the containment steel vessel wall which is much cooler. Heat is transferred to the interior surface of the containment by convection and steam condensation. Then heat is transferred through the containment steel wall by conduction and afterwards transferred from the containment exterior surface by evaporating the thin liquid film which is formed by delivering cooling water from water storage tank above the containment vessel dome. Air in the annular channel is heated by convection and introducing steam from the liquid film which is being evaporated. The heated air and steam in the annular space rise due to natural circulation and finally exit the concrete shield building through the outlets at the center top, as shown in Fig. 1-2.
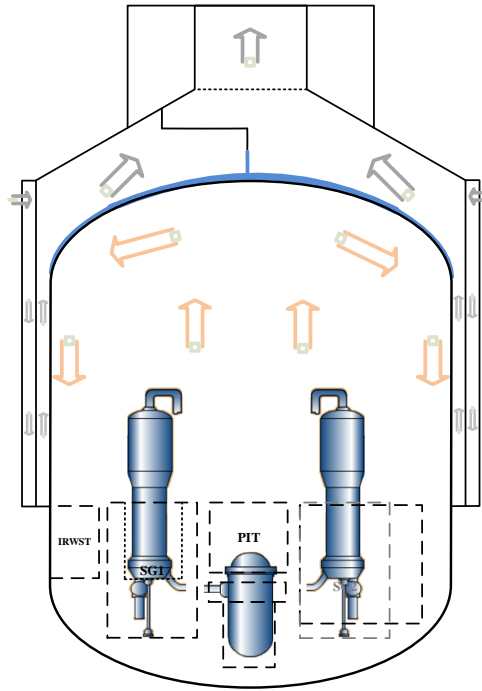
*Fig. 1-2 Schematic Diagram of Passive Containment Cooling System*

The concept of film cooling on the exterior surface of the containment is quite novel for the containment design and determines the performance of PCCS. In order to evaluate its efficiency and reliability, it's necessary to systematically investigate the containment response under accident scenarios with the activation of PCCS. Presently specialized physical models describing film behavior have been developed and implemented into computer codes, e.g. CDW model in COCOSYS [6], and Film Tracking model in MELCOR [7]. Nevertheless, some film behaviors such as the breakup, development of rivulets and the change of velocity distribution under countercurrent shear are not considered in these models. This may bring about inaccuracies and therefore lack the reliability of the prediction. Accordingly, behaviors of the film including its formation, development, transformation and the resultant influences on the PCCS cooling capability are of crucial significance to be investigated.

## 1.2  Objectives and structure of the thesis

In order to predict the thermal hydraulic transient inside the vessel and on the exterior surface of the containment shell during accidents and thus to confirm the reliability of the safety features of the containment, simulations with computer codes should be capable of capturing different phenomena and covering different scenarios since the beginning of the accident and activation of safety facilities. Moreover, a relatively large time scale usually from hours up to days after the onset of the accident should be simulated with reasonable computational effort [8]. Presently only so called Lumped

Parameter (L-P) codes meet the requirements of evaluating the long term transient and considering complicated phenomena during the whole process of accidents simultaneously. Different physical models considering various phenomena have been developed and integrated into L-P codes.

Since the Generation III nuclear reactors have introduced new design concepts such as passive safety features, some of the existing models in L-P codes may lack the capability to simulate some specific phenomena for the new design. Among these new features, particularly, the PCCS with film cooling contains plenty of physical processes. It is so novel that some film behaviors including the formation process, coverage form as well as the influence of shear stress are not taken into account so far in the water film models in different L-P codes. All these phenomena may have strong effect on the heat removal capability.

The main objective of the thesis is to investigate and then develop an integrated water film model considering the following phenomena:

The effect of interfacial shear stress, which is created by the countercurrent gas flow, on the velocity distribution and film thickness.

The behavior of film breakup and the coverage rate.

The formation and behavior of rivulets.

The new water film model is then implemented into the L-P code COCOSYS. Validation of the new model is also carried out on the basis of existing test results and experimental observations. The developed water film model is applied to evaluate the performance of PCCS employed in AP1000 containment and the European Generic containment [9]. The new model can therefore help to define and optimize the water flow rate of PCCS over time.

The thesis consists of six chapters. The first chapter briefly introduces the background and motivation of the research. The second chapter presents the literature review and the state of the art. The third chapter introduces the methodology of the modification in detail. In the fourth chapter the new model is validated against experimental data and is then assessed with test cases. In the fifth chapter the new model is applied for the PCCS of AP1000 passive containment and the Generic containment to evaluate its reliability, possible optimization of the flow rate of PCCS over time is studied as well. The sixth chapter draws conclusions and puts forward the outlook.

# 2  LITERATURE REVIEW

The evaporating thin liquid film flowing down a vertical or an inclined heated surface, due to its relatively small mass flow rate, large heat and mass transfer efficiency, has been widely utilized in various industrial processes including gas-liquid contacting equipment in distillation, rainwater runoff from building facades [10], liquid film drainage from the stator blades of steam turbine, wash down of aerosols in nuclear containment as well as liquid film cooling in PCCS to effectively remove heat from containment vessel [11]. A large number of hydrodynamic phenomena can be observed on the liquid film depending on the characteristics of the liquid - solid contact. Various phenomena including the formation of periodic waves, the breakup of the film, the formation and development of rivulets as well as shear stress acting on the interface between gas and liquid, may result in the change of the features of flow and heat transfer.

The film breakup refers to the conditions that the liquid film sheet splits into a series of stable liquid rivulets, leaving the substrate surface partially uncovered by the liquid, as shown in Fig. 2-1. Moreover, in the case of countercurrent vapor and gas flow, a thickening of the film may occur as well.
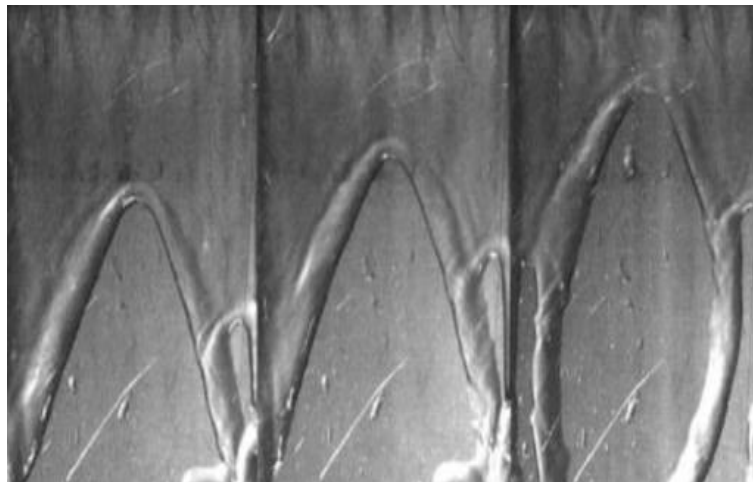


*Fig. 2-1 Film breakup with the decrease of the liquid loads on a stainless steel plate [12]*

Plenty of theoretical and experimental investigations regarding falling film have been carried out. Although the actual mechanism remains poorly understood, these attempts have revealed that the flow regime and patterns of water film are dependent on different factors including viscosity of the liquid, surface tension, physical properties of substrate as well as the environmental conditions [12-18]. Furthermore, some liquid film models considering film thickness, evaporation and condensation have been developed for

some simulation tools for the engineering level use [6, 18, 19].

## 2.1 Different regimes of falling liquid film

The falling liquid film is presented on the substrate either in the form of rivulet or film sheet. The liquid flowing down a vertical or inclined surface forms a free surface between liquid and gas phase. The profile of the surface depends on the forces acting on the interface. Rivulet refers to the condition that the free surface contacts the solid surface when the liquid of relatively small amount flows downward. The curve outlining the free surface on the rivulet cross section is the rivulet profile. When the mass flow rate is large enough and the substrate is completely covered by the water film, the flow pattern is regarded as film sheet, which also refers to the flat region presented in the central area of the rivulet when it is wide enough.

### 2.1.1 Film sheet

For the film sheet, Nusselt had provided his theory predicting the relationship between mass flow rate and film thickness as early as 1916 [20]. In the theory, assumptions have been made that the film flow is laminar, in absence of wave and without shear stress on the interface. For the film flow in Fig. 2-2, the Navier-Stokes equation can be expressed as:

$$\rho_l \frac{du}{dt} = -\nabla P + \rho_l g + \mu_l \nabla^2 u \tag{2-1}$$

It is assumed that:

$$u_y = u_x = 0 \tag{2-2}$$

$$\frac{\partial u_z}{\partial z} = 0 \tag{2-3}$$

With the assumption of no pressure change, Eq. (2-1) can be simplified as:

$$\mu_l \frac{\partial^2 u_z}{\partial y^2} = -\rho_l g \tag{2-4}$$

With the boundary conditions, as illustrated in Fig. 2-2.
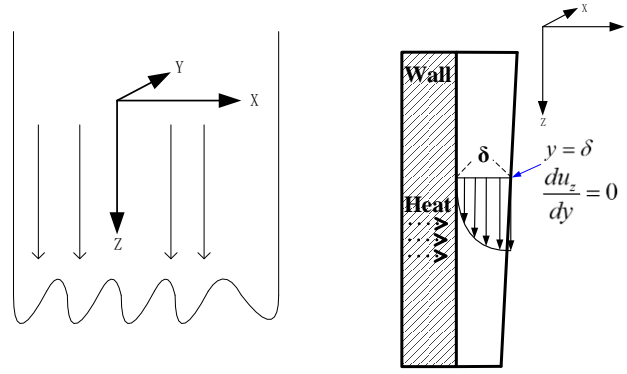
*Fig. 2-2 Velocity distribution in free falling film*

$$u_z = 0 \tag{2-5}$$

at the wall surface, and

$$\frac{du_z}{dy} = 0 \tag{2-6}$$

at the film surface. By integrating Eq. (2-4), it yields

$$u_z(y) = \frac{\rho_l g \delta^2}{2\mu_l}\left[\frac{2y}{\delta} - \left(\frac{y}{\delta}\right)^2\right] \tag{2-7}$$

Where $\delta$ stands for the film thickness. This indicates that the velocity distribution depends only on y, and can be regarded as one-dimensional. With Eq. (2-7), the relationship between mass flow rate per unit width and film thickness can be obtained and is expressed in Eq. (2-8),

$$M = \int_0^\delta \rho_l u_z(y)dy \tag{2-8}$$

Thus the film thickness is expressed as

$$\delta = \left(\frac{3}{4}\right)^{1/3} Re^{1/3}\left(\frac{v_l^2}{g}\right)^{1/3} \tag{2-9}$$

The reliability of Nusselt's theory in predicting the falling film thickness with a given mass flow rate has been confirmed when the film Reynolds number, defined as

$$Re = \frac{4M}{\mu} \tag{2-10}$$

is relatively small. Furthermore, based on Nusselt's theory, the following form of the expression,

$$\delta = a \, \mathrm{Re}^{b} \left( \frac{\nu^{2}}{g} \right)^{1/3} \tag{2-11}$$

has been widely used for empirical correlations in predicting the thickness of falling film sheet.

### 2.1.2 Rivulet

When the mass flow rate is not large enough, water film is presented in the form of rivulet rather than film sheet. The profile of the rivulet surface depends on the forces acting on the interface and therefore the contact angle, defined geometrically as the angle formed by the rivulet at the three-phase boundary, as shown in Fig. 2-3, is a significant factor which determines the profile of the rivulet.

### 2.1.3 Contact angle

The contact angle can be considered as the balance of three forces, namely, the surface tensions between solid and liquid $\sigma_{sl}$, that between solid and vapor $\sigma_{sg}$ and between liquid and vapor $\sigma_{lg}$ and given in Young's equation:

$$\sigma_{sg} = \sigma_{sl} + \sigma_{lg} \cos\theta \tag{2-12}$$
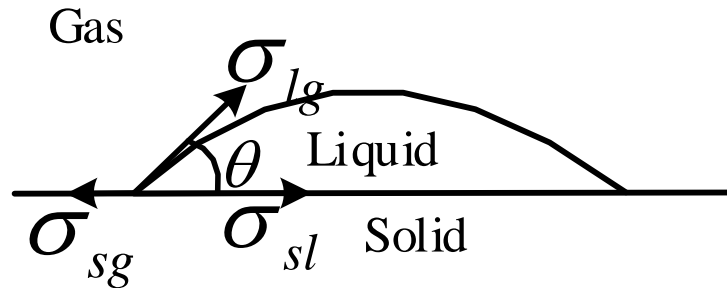


*Fig. 2-3 Contact angle balance on the rivulet cross-section*

The contact angle of falling rivulet depends on many factors including the substrate surface properties such as roughness, the preparation of the substrate (wetted before or dry), the speed of motion, liquid properties such as viscosity, density etc. and state of motion (advancing or receding) and so on [59].

Plenty of experiments reveal that for any postulated solid-liquid interaction there exists a range of contact angle. When the three-phase boundary or contact line of the rivulet is moving, the angle is referred to either as 'advancing' or 'retreating' angle when the wetting area is expanding or shrinking, respectively. The difference between the advancing and retreating contact angle leads to the phenomenon called hysteresis. When the contact angle is ranging between the advancing and retreating value, the

contact line usually stays invariable, as depicted in Fig. 2-4.



*Static behavior of hysteresis*

*Contact angle behavior with velocity*
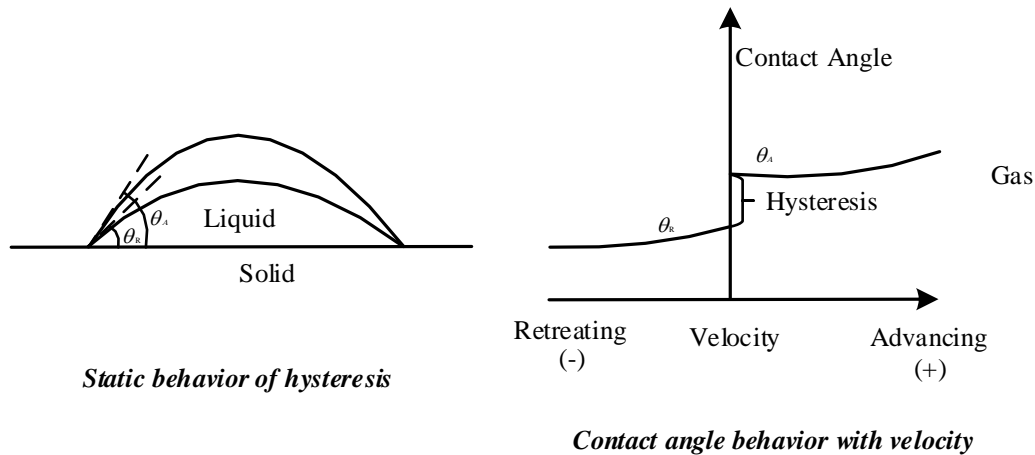
**Fig. 2-4 Hysteresis of Contact angle [59]**

Typically, better wetting occurs on surfaces with smaller contact angles. In practice, contact angles are measured for both advancing and retreating films. Usually the two values are quite different, the advancing contact angle is normally significantly larger than the retreating contact angle [59].

Andrzej Gajewski [21] presented experimental results of contact angle of rivulets on aluminum, brass and copper surface. The measurements were taken by increasing and decreasing the flow rate respectively. As a result, the hysteresis of the contact angle was observed. It was noticed that aluminum and brass surface at certain flow conditions can lose their hydrophobic properties and become hydrophilic materials. The worst wetting properties were observed for copper surface. It's also concluded that lower temperature improves the wetting property of metals.

The phenomenon of hysteresis is related to the friction force resisting the motion of the rivulets. A threshold of force at the contact line between three phases should be overcome before the rivulets start to move. Many works have theoretically or experimentally studied this phenomenon, however the mechanism is still under investigation [81-85].

### 2.1.3.1 Geometry of rivulet

The specific narrow rivulet on a flat plate is shown in Fig. 2-5, where 2a indicates the rivulet width and $\delta_r$ stands for the rivulet height at a certain inclination of the plate $\alpha$. $u$ represents the mean velocity of the rivulet and $\theta$ the contact angle between rivulet and substrate.
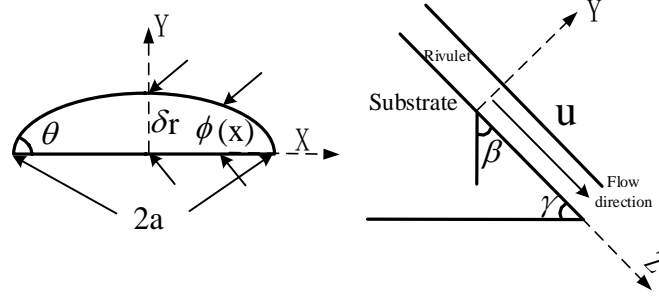
***Fig. 2-5 Rivulet profile***

The current research is focusing on the laminar steady rivulet flowing downward on a flat plate. Assumptions are made that the flow is incompressible, one dimensional, fully developed and parallel to the plate as shown in Fig. 2-5. In addition, the pressure is considered constant in x direction, i.e., Eq. (2-13) and the pressure gradient in y direction is expressed with Eq. (2-14). The momentum equation in z direction is given by Eq. (2-15). As indicated in Fig. 2-5, the height of the rivulet is represented with $\delta_r$ while the profile is denoted by $\phi(x)$.

$$\frac{\partial p}{\partial x} = 0 \tag{2-13}$$

$$\frac{\partial p}{\partial y} = -\rho g \cos\gamma \tag{2-14}$$

$$\frac{\partial^2 u}{\partial x^2} + \frac{\partial^2 u}{\partial y^2} = -\frac{g\sin\gamma}{\nu} \tag{2-15}$$

Plenty of studies [19, 20, 22-29, 86] have been done regarding either the height, width, velocity distribution or the profile of rivulets on the basis of these assumptions.

**Al-Khalil and Kern's study**

Based on the assumptions from Eq. (2-13) to Eq. (2-15), and the boundary conditions including no slip at the liquid-solid interface, symmetrical geometry and no shear at the liquid-gas interface, Kern [22, 23] proposed two correlations predicting the height of rivulets on the vertical plate for the laminar rivulet flow and turbulent flow respectively, which are expressed as functions of Reynolds number:

$$\delta_{r,\text{laminar}} = 1.645\,\text{Re}_r^{1/3}\left(\frac{\mu_l^2}{\rho_l^2 g}\right)^{1/3} \tag{2-16}$$

$$\delta_{r,\text{turbulent}} = 0.815\,\text{Re}_r^{7/15}\left(\frac{\mu_l^2}{\rho_l^2 g}\right)^{1/3} \tag{2-17}$$

where $\text{Re}_r$ refers to Reynolds number and is dependent on the mean velocity defined

as:

$$\mathrm{Re}_r = \frac{\rho_l u_{r,mean} \delta_r}{\mu_l} \tag{2-18}$$

With same assumptions and boundary conditions, in the study of Al-Khalil et al. [24], the velocity distribution is numerically calculated with the Finite Element Method, a dimensionless average and a maximum velocity in the rivulet are derived as expressed in Eq. (2-19) and Eq. (2-20).

$$V_{r,mean} = \frac{u_{r,mean} \mu_l}{\rho_l g \delta_r^2} \tag{2-19}$$

$$V_{r,max} = \frac{u_{r,max} \mu_l}{\rho_l g \delta_r^2} \tag{2-20}$$

They assume that the rivulet is presented on a vertical plate and with small contact angles. For the laminar film flow, the averaged and maximum dimensionless velocities are defined as 1/3 and 0.5 respectively.

**Bentwich's study**

Bentwich et al. also [25] proposed an analytical solution for the velocity distribution of rivulet flowing down a vertical plate. In addition, a polynomial is obtained in this work with the numerical method for the rivulet on the incline plate.

The cross section was assumed as elliptical and the contact angel is up to 150°. The rivulet profiles of cross section on the vertical and inclined plates are shown in Fig. 2-6 (top). When the rivulet is present on the vertical substrate and being expanded, the contact angle is reducing while the height doesn't change. On the other hand, when the rivulet is placed on the inclined substrate, the height is increasing as the rivulet is expanded as shown in Fig. 2-6 (bottom).
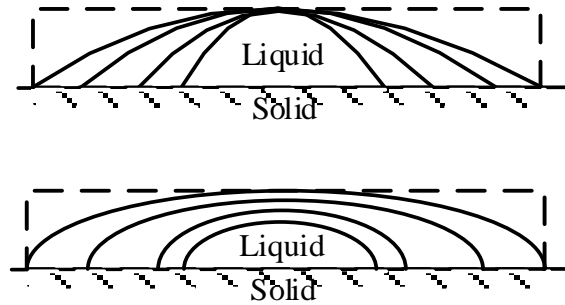


*Fig. 2-6 Bentwich predictions for the rivulet profile shapes on vertical (top) and inclined (bottom) flat plate*

**Bankoff and Mikielewicz & Moszynski's study**

Bankoff [30] and Mikielewicz & Moszynski [31] assumed that for a relatively low mass flow rate, the rivulet cross-section is a segment of a circle. A comparison of their results shows that the assumption is an adequate one, in agreement with the analysis of Towell & Rothfeld [32]. Cross-section of a rivulet was considered to be a segment of a circle of radius R and is shown in Fig. 2-7. The height of the rivulet $\delta(x)$, is given by

$$\delta_r(x) = R(\cos\theta' - \cos\theta) \tag{2-21}$$

where $\theta$ denotes the solid-liquid contact angle, as shown in Fig. 2-7.
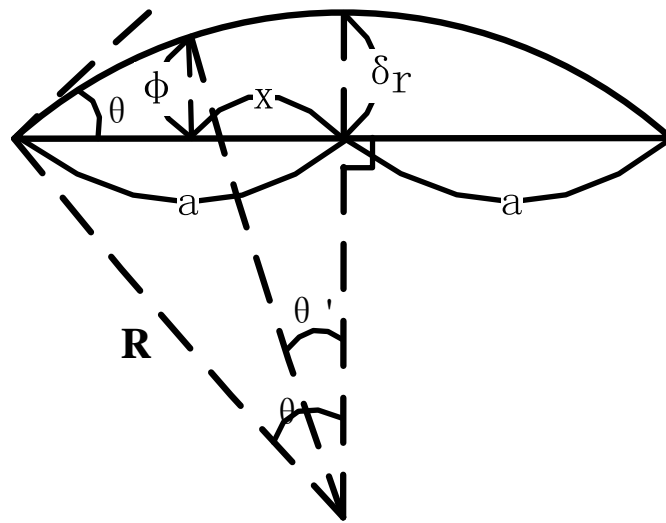


*Fig. 2-7 Bankoff's assumption of rivulet profile*

**Doniec's study**

As proposed by Doniec [14], and also applied and/or experimentally observed by other studies [12, 15-17], the profile of the rivulet cross section is regarded as a circular segment and a rectangular film sheet in the middle, as indicated in Fig. 2-8, where 2a and b are the width of circular segment and width of rectangular part respectively. $\phi(x)$ represents the profile of rivulet and $\delta_{r,crit}$ is the height of the stabilized rivulet. In the figure, $\theta$ indicates the contact angle between rivulet and substrate, which reflects the overall effect of environment as well as physical properties of liquid and substrate and determines the height of the stabilized rivulets.
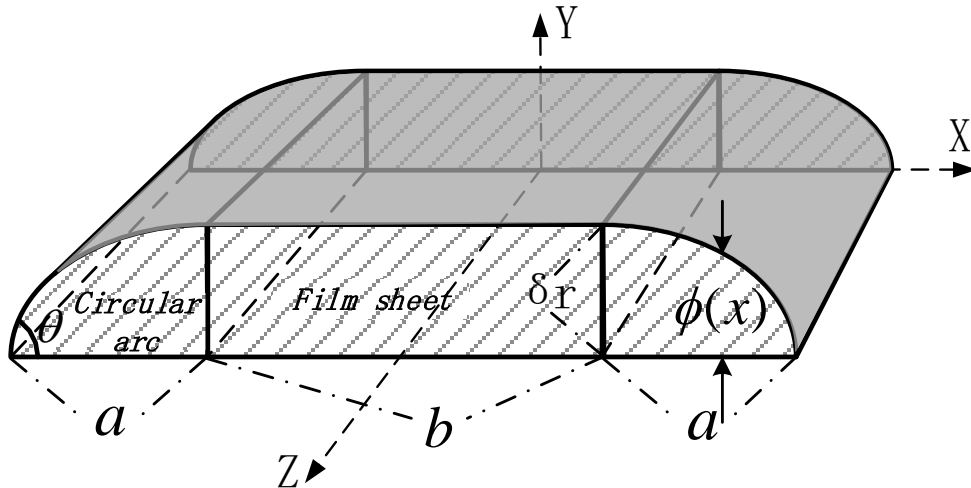
*Fig. 2-8 Doniec's rivulet profile*

### 2.1.4 Wave on the film surface

One of the limitations of Nusselt's theory is the assumption of smooth surface. However, instability is one of the most significant characteristics of film flow, which results in the generation of surface wave. The small disturbance is produced on the film surface as it flows down and gradually develops into big solitary waves. Thus, the velocity distribution in the smooth film is deformed.

Yu et al. [33] concluded that falling film flow usually consists of film substrates, large solitary waves, and small capillary waves in front of solitary waves. The sketch of film flow structure considering the wave on surface is shown in Fig. 2-9.
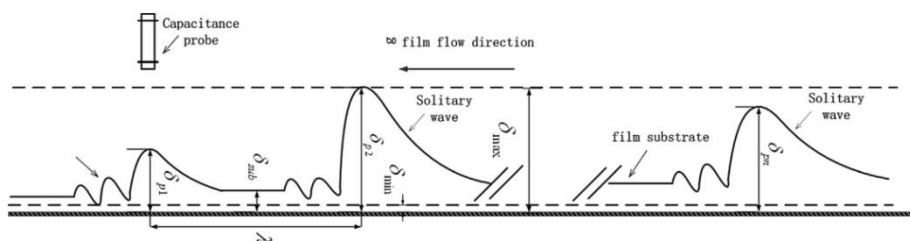


*Fig. 2-9 Sketch of film flow structure [87]*

Moran et al. [34] experimentally investigated instantaneous hydrodynamic characteristics of laminar falling films on an inclined plate with a photochromic dye activation technique. The Reynolds number ranges from 11 to 220. In the experiment the instantaneous velocity distribution on the laminar film was measured. The data indicated that the maximum velocity at the crest of the wave is over-predicted by Nusselt's theory, while the time-averaged film thickness is only slightly under-predicted. The instantaneous velocity profile in different regions of the wavy film also indicated

that the velocity profiles in the film substrate (the very thin layer of film attaching the structure) was in agreement with Nusselt's theory, as depicted in Fig. 2-10. Based on the velocity profile, it's concluded that substantial liquid mass was transported by the waves.
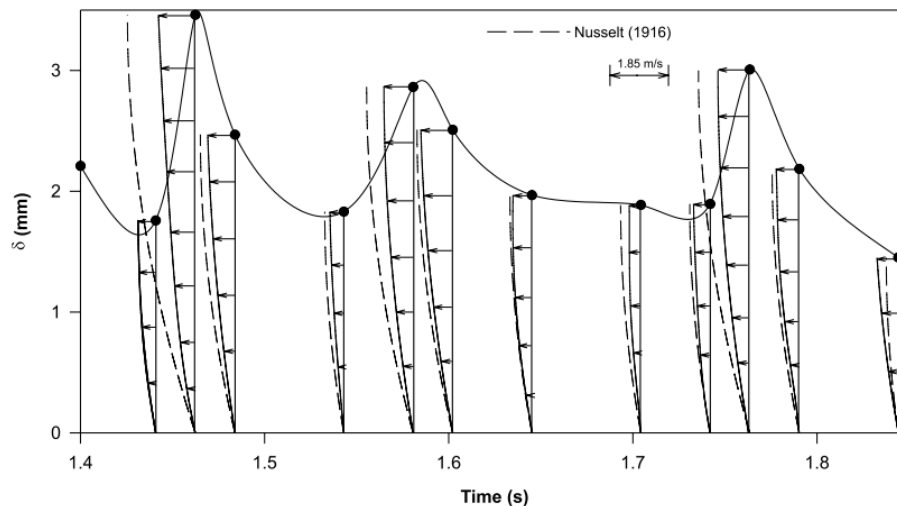


*Fig. 2-10 Variations of instantaneous velocity profile and film thickness at Re = 220 [34]*

Park et al. [35] and Nosoko et al. [36] had also experimentally observed the evolution of solitary waves on a flat plate with Re from 10 to 100, and studied the transition of flow patterns as well as hydrodynamic features. The measurements also pointed out that the surface wave enhances mass transfer.

Wave behavior on film flow has been studied for several decades, but the fundamentals are still not fully understood. As a result of chaotic characteristic of film flow [37], wave behavior on the film flow is quite random. Therefore, it is reasonable and feasible to describe the film flow behavior statistically, especially when the study focuses on the large scale surface such as containment film cooling.

Numerous studies have been conducted to statistically analyze the characteristics of falling liquid film such as the study of Ambrosini et al. [38], which investigated the behaviors of water film freely falling down a vertical and inclined flat plate. In the work, time-averaged, minimum and maximum film thickness and wave velocity are statistically analyzed with the Re number from 140 to 3200 and different water temperature. Yu et al. [33] had also experimentally studied the water film falling and spreading on a large vertical flat plate. The experiments aim at investigating the flow characteristics of a falling film. The Reynolds number of falling film ranges from 50 to 900. The water film thickness and wave velocity are measured. Experimental results on film thickness, its probability density function, as well as coverage rate and wave velocity are presented and discussed. Many of such studies had approximated the results of time averaged film thickness with empirical correlations, as listed in Table 2-1.

*Table 2-1 Empirical correlations for averaged film thickness*

| Author | Re range | Relations |
|---|---|---|
| Nusselt [20] | 0 < Re < 1000 ~ 2000 | $\delta = 0.909\,\mathrm{Re}^{1/3}\left(v^2/g\right)^{1/3}$ |
| Jiang [39] | 400 < Re < 5000 | $\delta = 0.295\,\mathrm{Re}^{0.498}\left(v^2/g\right)^{1/3}$ |
| Takahama [40] | Re > 1472 | $\delta = 0.228\,\mathrm{Re}^{0.526}\left(v^2/g\right)^{1/3}$ |
| Brauer [41] | | $\delta = 0.208\,\mathrm{Re}^{0.533}\left(v^2/g\right)^{1/3}$ |
| Karapantsios [42] | 500 < Re < 13000 | $\delta = 0.214\,\mathrm{Re}^{0.538}\left(v^2/g\right)^{1/3}$ |
| Yu [12] | 80 < Re < 900 | $\delta = 0.462\,\mathrm{Re}^{0.422}\left(v^2/g\right)^{1/3}$ |

Most of these experimental results have indicated that for the flow regime with Reynolds number smaller than about 1500, even though waves on the film surface have been generated, Nusselt's prediction is in good accordance with the test data. This fact may imply that liquid films are characterized by wavy laminar flow within this range [40].

### 2.1.5   Liquid film under shear stress

Interfacial shear stress at film surface, created by the countercurrent flow of gas in the channel of passive containment system, may change the characteristics of film flow and heat transfer at the film surface.

According to Aiello and Ciofalo et al. [18], for the air-water system such as PCCS, if the physical properties are evaluated at the ambient temperature, flooding takes place only if the mean air speed is beyond 15 m/s. Kang and Park [44] also denoted that significant entrainment on the water film does not occur when the countercurrent air velocity has been increased up to 8.5 m/s, which is more than the expected air velocity of 3 - 4 m/s in PCCS vertical channel [43]. The possibility of flooding by hydrodynamic instability can therefore be ruled out from the key concerns of countercurrent gas flow. However, the interfacial shear may change the velocity distribution inside the film, as indicated in Fig. 2-11.
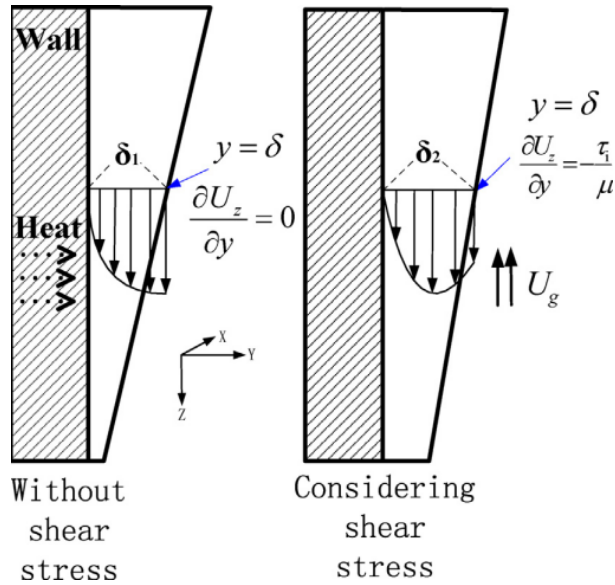
*Fig. 2-11 Film thickness influenced by shear stress*

When the falling water film has completely covered the plate, it can be considered as one dimensional under steady state. The boundary condition at the interface is:

$$\frac{\partial u_l(\delta)}{\partial y} = -\frac{\tau_i}{\mu_l} \tag{2-22}$$

where

$$\tau_i = \frac{1}{2} f \rho_g \left( u_i - u_g \right)^2 \tag{2-23}$$

where $f$ is the drag force factor. Lots of experiments have been conducted regarding liquid film behavior under countercurrent gas flow, many of which have obtained expressions for the drag force factor. Nevertheless, it can be seen that the drag force factor relies strongly on the experimental conditions and flow patterns of the experimental fluids. Table 2-2 summarizes the drag force factors obtained from literature.

**Table 2-2 Predictions of interfacial drag force factor of film flow.**

| Authors | Geometry | Pattern | $f$ - drag force factor |
|---|---|---|---|
| White [45] | Parallel plates | Countercurrent, Turbulent | $(\frac{1}{4f})^{0.5} = 2\log_{10}(\text{Re}_l(4f)^{0.5}) - 1.19$ |
| Moeck and Stachiewicz [46] | Annular flow, two-phase flow | Co-current | $f = 0.05\left[1 + 545(\bar{\delta}/R)^{1.42}\right]$ <br> Where $R$ is the hydraulic radius while $\bar{\delta}$ indicates the mean film thickness |
| Grolmes Lambert and Fauske [47] | Vertical circular tube | Countercurrent | $f = 0.006 + \bar{A}\delta^2(\mu_l/\mu_R)^{-0.44}$ <br> $A = 2 \times 10^6 m^{-2}$ <br> Where $\mu_l$ represents a reference liquid viscosity |
| Drosos et al. [48] | Circular tube | Countercurrent | $f = 0.008\left[1 + c_3(\frac{\delta}{d})^{c_4}\right]$ <br><br> $Bo = \left[\frac{(\rho_l - \rho_g)g}{\sigma}\right]^{1/2} \cdot d$ <br><br> $c_3 = 41.3Bo^{(c_4+0.25)} \cdot 10^{9.07/Bo}$ <br><br> $c_4 = 1.63 + \frac{4.74}{Bo}$ |
| Wallis [49] | Annular flow | Co-current | $f = 0.005(1 + 300(\frac{\delta}{d}))$ |
| Zapke and Kröger [50] | Ducts, H = 50-150mm, b = 20 mm | Countercurrent, Laminar | $f = \frac{96}{\text{Re}_l}$ |
| Bharathan et al. [51] | Annular flow, ID =51mm | Countercurrent | $f = 0.005 + 406(\frac{\delta}{d})^{2.04}$ |
| Vijayan et al. [52] | Annular flow, ID = 25.67 and 99 mm | Countercurrent | $f = 400\sqrt{\text{Re}_l}d^*\delta^*/\text{Re}_g^{1.2}$ <br><br> $d^* = \frac{d}{L_L}, \delta^* = \frac{\delta}{L_L}$ |
| Fore et al. [53] | Annular flow, ID = 5.08mm, L = 101.6mm | Countercurrent | $f = 0.005\left\{1 + 300\left[(1 + \frac{17500}{\text{Re}_g})\frac{\delta}{d} - 0.0015\right]\right\}$ |
| Maharudrayya and Jayanti [54] | Annular flow, ID = 25mm and L = 60 – 2000mm | Countercurrent | $f = 15.7(\text{Re}_l)^{0.85}(\text{Re}_g)^{0.85}(d^+)^{-1.7}$ <br><br> $d^+ = \frac{d}{\sqrt{\frac{\sigma}{(\rho_l - \rho_g)g}}}$ |
| Stephan and Mayinger [55] | Rectangular flow | Countercurrent | $f = 0.079\text{Re}_g^{-0.25}(1 + 115\delta^{*N})$ <br><br> $N = 3.95/(1.8 + \frac{3}{Bo}), Bo = \frac{D_h}{L_L}, \delta^* = \frac{\delta}{L_L}$ <br><br> $L_L = (\frac{\sigma}{(\rho_l - \rho_g)g\sin\varphi})^{1/2}$ |

## 2.1.6 Critical state of liquid film

One of the noteworthy phenomena of falling water film is its breakup. During the accidents of reactors with PCCS activation, the inner surface temperature of the containment will increase due to the heat release from reactor cooling loops, and the evaporating water film is getting thinner as it flows downward on the exterior surface of containment. Ideally, the efficiency of film cooling reaches its maximum if the water film is dried out exactly at the bottom of containment. However as many experiments indicate [12, 56], the water film will split into rivulets with the formation of dry patches before it has been completely evaporated, as illustrated in Fig. 2-12. This could limit the fraction of surface covered by film and thus reduce cooling effectiveness.
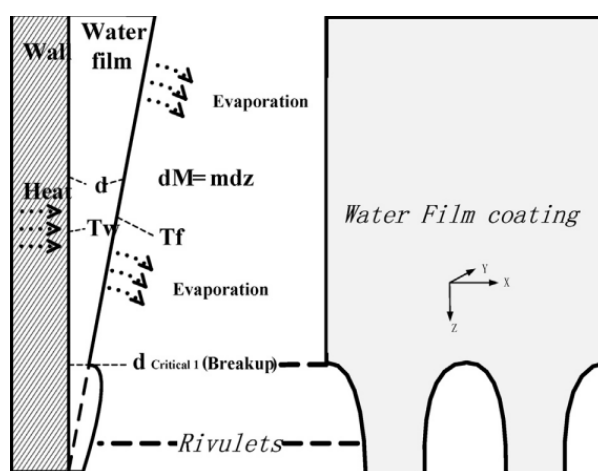


*Fig. 2-12 Scheme of film breakup*

Plenty of theoretical and experimental investigations [13-17] regarding falling film breakup have been carried out and it is revealed that a critical film thickness for breakup exists and is dependent on surface tension and film stability, determined by its physical properties. Nevertheless, the actual mechanism remains poorly understood.

### 2.1.6.1 Critical state of fully covered film

One of typical ways of investigating film breakup is to analyze film stability by imposing a small disturbance on the laminar film, which may result in rupture [57]. However the theory is available only for the disturbances of the same order of film thickness whereas not valid for the small perturbations.

Another commonly used approach proposed by Hartley and Murgatroyd [13] is through the analysis of force balance at the three-phase stagnation point of dry patch formed after film breakup. The force balance (FB) criterion has considered contact angle between liquid and substrate, which is believed to reflect the wall influence on the breakup process. However, the profile of liquid-gas interface near the stagnation point is not accounted for in this theory. The thickness predicted with this criterion is proved

to be much higher than the measurements.

Application of minimum total energy (MTE) principle to the prediction of water film critical state is also originated with the work of Hartley and Murgatroyd [13]. It is suggested that a stable film configuration is reached when the total energy, which consists of kinetic and surface energy, is minimized. For fully covered situation, the critical thickness predicted with the minimum total energy criterion without counter-current air reported by Hartley and Murgatroyd [13] is expressed as:

$$\delta_{Critical} = 1.34 \left( \frac{\sigma}{\rho_l} \right)^{0.2} \left( \frac{\mu_l}{\rho_l g \sin\gamma} \right)^{0.4} \tag{2-24}$$

Based on Nusselt's velocity distribution, the corresponding critical mass flow rate is:

$$M_{Crit} = \frac{\rho_l^2 g \sin\gamma}{3\mu_l} \delta_{Crit}^3 \tag{2-25}$$

The results with MTE principle exhibit better agreement with measurements than those with force balance (FB) evaluations.

### 2.1.6.2 *Critical height of rivulets*

The critical height of rivulet, which is denoted by $\delta_{riv,crit}$, refers to the height of rivulets when the equilibrium, stationary state of the flowing rivulet is reached [14, 15]. The MTE principle has been widely used also for the studies of rivulet critical state [14-17, 30, 31]. These works mainly focus on the critical state of a rivulet by specifying its profile of cross section and calculating the corresponding velocity distribution, and all have taken contact angle into account. Table 2-3 summarizes some expressions predicting critical state of liquid rivulets.

*Table 2-3 Predictions of critical thickness of a rivulet in literatures.*

| Authors | Expressions | Comments |
|---------|-------------|----------|
| Hobler [58] | $\Delta_{riv,crit} = \left(3/2\right)^{1/5}\left(1-\cos\theta\right)^{1/5}$ | Based on minimum total energy theory for a stable liquid rivulet; Zero order velocity approximation; $\Gamma_{riv,crit}$ is calculated according to Nusselt's approximation |

| | | |
|---|---|---|
| Bankoff [30] | $\Delta_{riv,crit}^5 + (1-\cos\theta)$ $-G^*(\theta_0)\Delta_{riv,crit}^3 = 0$ $\Gamma_{riv,crit} = 1.693\Delta_{riv,crit}^3$ | Based on MTE theory; Zero order velocity approximation; Rivulet profile assumed as circular; $\Gamma_{riv,crit}$ is calculated according to Nusselt's approximation |
| Doniec [14, 15] | $\Delta_{riv,crit} = (3/7)^{1/5}(1-\cos\theta)^{1/5}$ $\Gamma_{riv,crit} = 1.693\Delta_{riv,crit}^3$ | Based on MTE theory; Zero order velocity approximation; $\Gamma_{riv,crit}$ is calculated according to Nusselt's approximation |
| El-Genk and Saber [16] | $\Delta_{riv,crit} = (1-\cos\theta)^{0.22}$ $\Gamma_{riv,crit} =$ $0.67\Delta_{riv,crit}^{2.83} + 0.26\Delta_{riv,crit}^{9.51}$ | Based on MTE theory; Two dimensional velocity distribution; Rivulet profile assumed as circular; $\Gamma_{riv,crit}$ is calculated based on two dimensional velocity distribution |

Where

$$\Delta_{riv,crit} = \delta_{riv,crit} / \left[15\mu_l^2\sigma / (\rho_l^3 g^2)\right]^{0.2} \qquad (2\text{-}26)$$

specifies the dimensionless film thickness for critical state, and

$$\Gamma_{riv,crit} = M_{riv,crit} / \left[\rho_l\mu_l\sigma^3 / g\right]^{0.2} \qquad (2\text{-}27)$$

indicates the dimensionless flow rate per unit width.

Some other works [30, 31] have accounted for the transition process. Nevertheless, the profile of the rivulet cross section, which is simply assumed as a circular segment in these works, is not consistent with the observations of experiments such as those conducted by Gajewski and Yu as well as the large scale experiment [12, 21, 59], especially when the flow rate of rivulet is relatively large.

Moreover, when countercurrent air is imposed on the surface of flat film or rivulets, the velocity profile and the stability of falling film are changed, subsequently the critical state is changed. Regarding the influence of interfacial shear, Hartley and Murgatroyd [13] derived the critical state of fully covered film under surface shear on the horizontal plate. Chung and Bankoff [30] developed a model of falling liquid film breakup considering the transition process from film to rivulets under shear stress. The model is based on FB criterion and the profile of rivulet is assumed as circular segment. Saber and El- Genk [17] have derived the critical state of falling rivulet under countercurrent flow with MTE criterion by approximating two dimensional velocity approximation. Other experimental studies including those conducted by Yu and Roy [12, 61] which

have taken countercurrent flow on the film surface into account.

## 2.2 Falling Film Cooling for Passive Containment Cooling System

### 2.2.1 Introduction of PCCS

Passive safety features have been employed in both AP600 and AP1000. The passive containment cooling system can restrict the temperature and pressure inside containment in case of the loss of coolant accident (LOCA) or main steam line break (MSLB) accident by removing thermal energy from the containment atmosphere and transferring heat to the ultimate heat sink. In addition, this cooling approach also limits the release of radioactivity due to the reduction of the pressure differential between the containment and external environment[1].
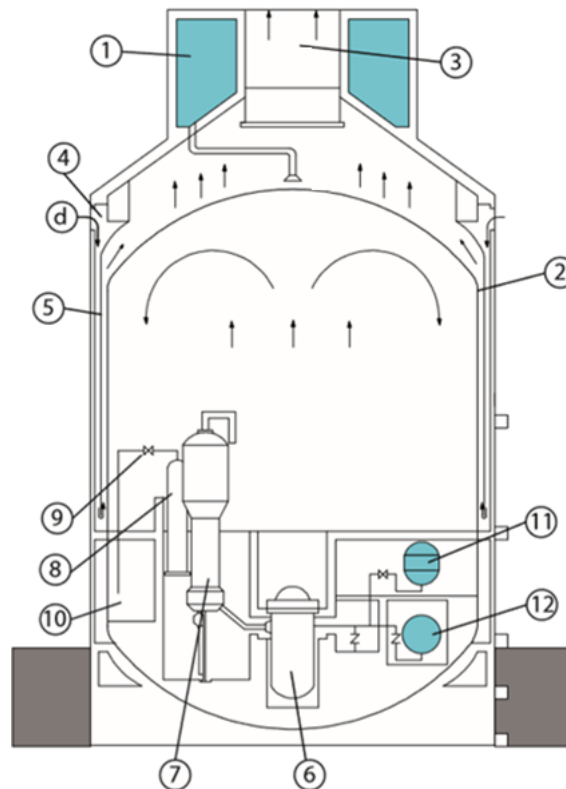


*Fig. 2-13 Layout of AP 1000 containment [3]*

1. Cooling water storage tank
2. Steel containment
3. Air outlet
4. Air inlet
5. PCCS baffle plate
6. Reactor Pressure Vessel
7. Steam generator
8. Pressurizer
9. Safety valves

21

10. IRWST
11. Core makeup tank
12. Accumulators

Fig. 2-13 displays the layout of the containment of AP1000, while the sketch of Passive Containment Cooling System is illustrated in Fig. 2-14.
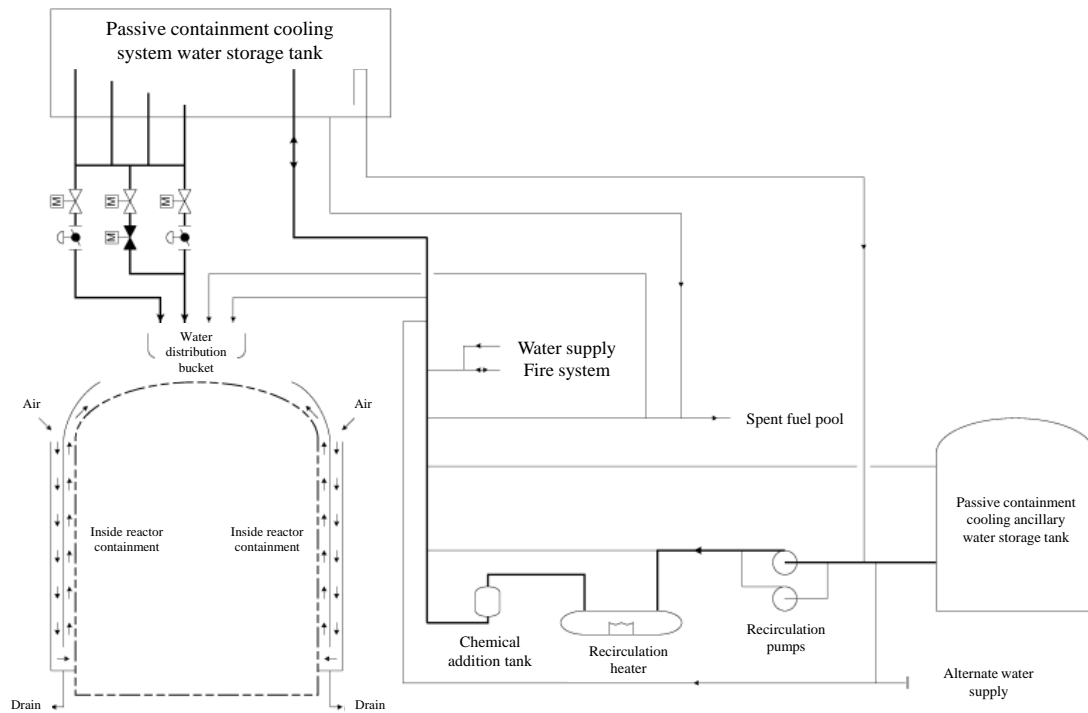


*Fig. 2-14 Simplified Sketch of Passive Containment Cooling System [4]*

The passive containment cooling system has utilized steel containment and concrete shield building around it. The major components of the passive containment cooling system include [4]:

**Passive containment cooling water storage tank (PCCWST)**

The passive containment cooling water storage tank is placed above the steel containment vessel and is integrated into the shield building structure. The storage tank is filled with demineralized water of minimum required volume, which can provide liquid film cooling for at least 72 hours for the cooling function.

**Water distribution system**

The water distribution system is installed on the exterior surface of the steel containment vessel in order to distribute water flow on the containment. Above the containment dome, a water distribution bucket is hung from the roof of the shield building, to deliver cooling water to the exterior surface of the steel containment.

The passive containment cooling water source can be discharged into the bucket. Then

the water is delivered to the center top of the containment dome by the water distribution bucket. As it flows over the dome, it's evenly distributed by slots in the distribution bucket.

Additionally, two sets of weirs are installed on the containment upper dome at different radius to collect and then redistribute the cooling water to increase the shell coverage. The distribution system can be functioning during very low PCCS flow rate or high ambient temperature conditions.

**Air Flow Path**

The air flow path is introduced to the design to direct the vapor and air along the exterior surface of the containment shell in order to enhance the heat convection and therefore the cooling performance. The air flow path consists of a screened shield building inlet and an air baffle defining the path of gas flow and separating the outer flow annulus and inner one. The air baffle is located between the concrete shield building and steel containment vessel.

During the accidents, the steam inside the containment comes in contact with the containment steel vessel wall and condensed due to the low surface temperature. Heat is then transferred to the exterior surface of the containment by conduction and removed by convection, evaporation of water film and radiation. As a result, the air in the inner annular space becomes less dense and rises due to natural circulation. Finally the hot air exits the concrete shield building through the outlet at the center top.

**Passive Containment Cooling Ancillary Water Storage Tank**

The passive containment cooling ancillary water storage tank is filled with demineralized water of sufficient volume for makeup to the spent fuel pool as well as passive containment cooling water storage tank. The tank is placed at the ground level close to the auxiliary building. Sufficient thermal inertia is assured for the tank that freezing is prevented for 7 days without heater operation in case of low environmental temperature. The piping system is also maintained dry to prevent freezing.

The operation of passive containment cooling system, as depicted in Fig. 2-14, is initiated either by the reception of containment pressure signals or operator's manual actuation. The isolation valves of passive containment cooling water storage tank are opened after the activation of the PCCS system. This allows the cooling water in PCCWST to be delivered to the top of the steel dome and as it is driven by gravity and flows downward, the water film is formed.

For the structure of the containment shell, a corrosion resistant coating for the containment vessel is utilized in order to enhance surface wettability and stabilize the film formation. When the film delivered to the containment shell is not completely evaporated, the rest water goes to the bottom of the inner annulus and is collected by the drains. The redundant annulus drains directs the rest water out of the annulus. The annulus drains are located on the shield building wall slightly above the floor level to avoid the clogging by debris.

During the operation of PCCS, water supply can be replenished by operator action from

the passive containment cooling ancillary water storage tank or alternative water source connected to the containment shell through the piping system. In PCCS ancillary water storage tank, the inventory sufficient to maintain the minimum flow rate for an 4 days in addition.

### 2.2.2 PCCS oriented studies on falling liquid film behaviors

Aiello and Ciofalo [18] studied the cooling of a hot vertical wall by a falling liquid film of large scale facilities such as Passive Containment Cooling System (PCCS) in AP600/AP1000 facilities. In their work, a system of a vertical channel is established where the liquid film can be delivered onto the wall surface. Air from the environment flows along the channel with a mass flow rate, which depends on the balance between hydraulic resistance and buoyancy force, as depicted in Fig. 2-15. A simplified computational model of the above system was developed and applied to the prediction of relevant quantities. Conclusions were also drawn on the cooling strategy to be adopted in the case when only a limited amount of coolant is available.
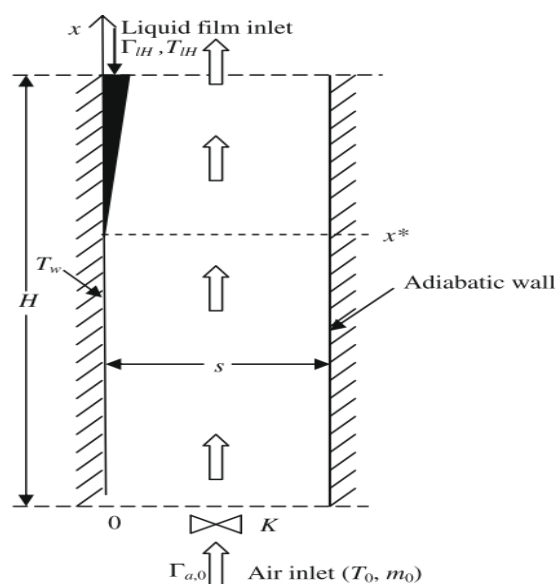


*Fig. 2-15 Schematic of PCCS film cooling [18]*

Based on the design of PCCS, Yu et al. [12, 33] conducted an experimental study of free falling water film flow on a vertical and an inclined flat plate ( $2 \times 5m$ and $0.4 \times 5m$ ) at $50 < \text{Re} < 3600$, as shown in Fig. 2-17. Many statistical variables of the film flow are presented, such as film thickness, wave length, wave frequency, and wave velocity etc. The test data are also compared with some empirical correlations. The effect of Reynolds number and inclination of the plate on film flow are studied. With the increase in Reynolds number, the solitary waves of film flow develop from low speed waves of high frequency and short wave length to high speed waves of low frequency and long wave length. Empirical correlations of film thickness and velocity of wave are obtained and can be applied to the safety analysis program for PCCS.
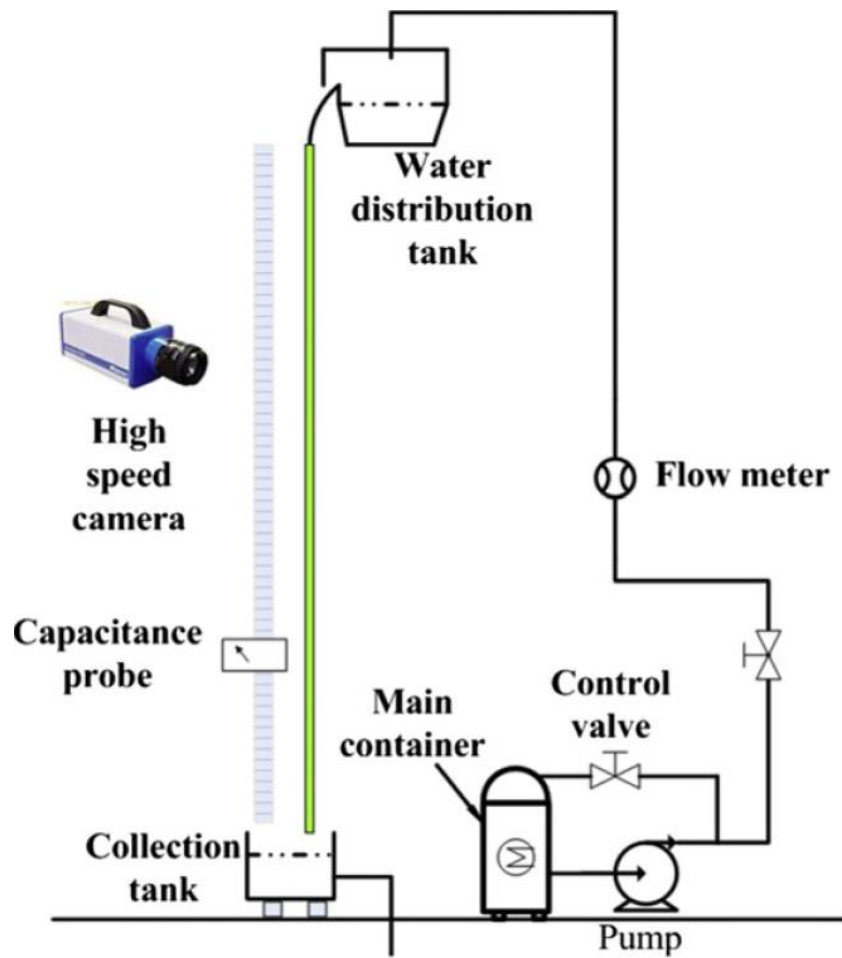
*Fig. 2-16 Schematic of the experimental setups of Yu [88]*
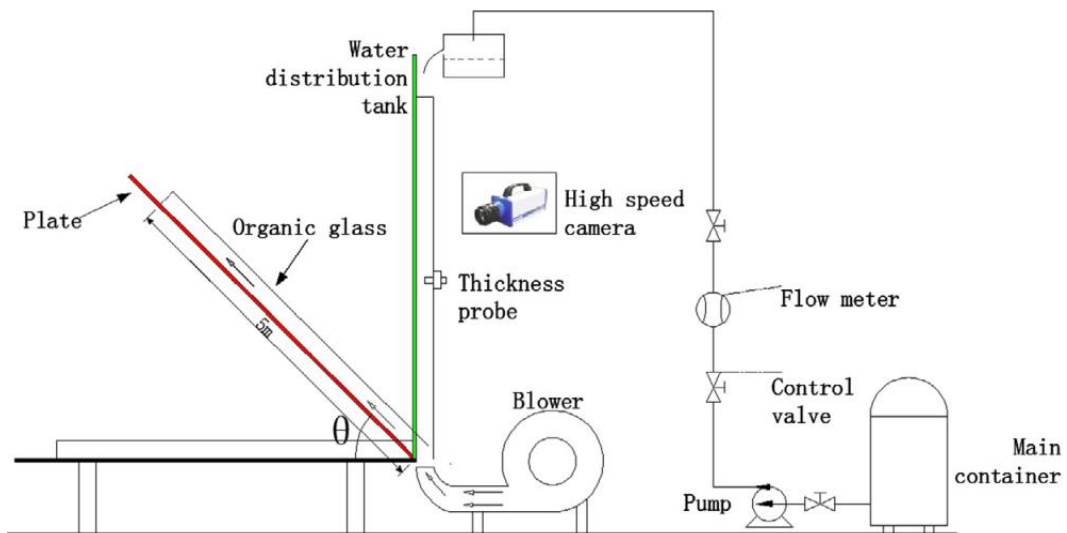


*Fig. 2-17 Schematic of the experimental setups of Huang [62]*

Aiming at investigating film flow behaviors under countercurrent flow of PCCS, Huang et al. [62] experimentally studied water-air countercurrent flow in a rectangular channel. The experiment is carried out in a large scale facility (Fig. 2-17) that consists of a large scale flow channel and a rotatable operating platform which provides different inclinations. The results show that the film thickness variation in the large scale channel under countercurrent flow condition is different from the results from small scale tests. The critical air velocity for the onset of flooding is discussed for different film Reynolds numbers.

Furthermore, Westinghouse had set up the large scale test facility (LST) [59] to integrally study the behavior of passive containment film cooling (Fig. 2-18). The experimental data are then used to validate their in-house version of the computer code W-GOTHIC. The basis for determining the PCCS flow rate input for WGOTHIC has been developed based on PCCS test data and observations. The portion of the containment shell perimeter that is wetted versus the amount of water being delivered from the PCCS water storage tank to the containment dome has been based on data from the water distribution test. This test was performed with prototypic water distribution devices on a full sized segment of the dome and top of sidewall. The relationship of wetted perimeter to delivered flow is conservatively bounded by a linear equation. The wetted perimeter used in the PCCS film coverage model is limited to a certain percentage of the containment circumference.
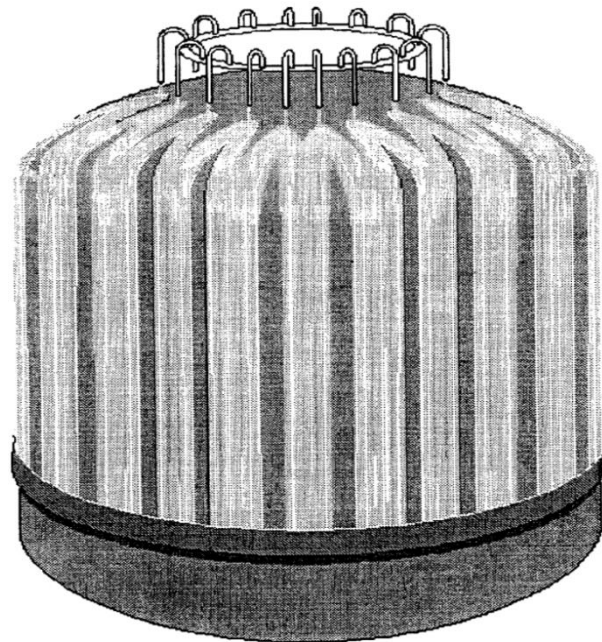


*Fig. 2-18 Water film Coverage Pattern of PCCS large scale test [59]*

## 2.3   Study of PCCS with Lumped-Parameter codes

The most commonly used tools to systematically analyze the long term thermal-hydraulic phenomena of NPP's containment are so called lumped-parameter (L-P) codes, which can comprehensively perform parametric analysis of accident scenarios and only limited computational resources are required. L-P codes are therefore suitable for level 2 probabilistic safety analysis, while the computational fluid dynamics (CFD) codes need much larger computer resources and are not yet developed sufficiently to simulate two-phase phenomena reliably [64], especially for multi-phenomena accident scenarios taking place in containment.

### 2.3.1   Introduction of Lumped-Parameter codes

The principle of the lumped-parameter codes is to replace mathematical model variables, which are assumed spatially distributed in the field, with single values. e.g., the temperature field may be subdivided into zones and described by averaged temperatures in each one [65]. When simulating the containment behaviors with L-P codes, the containment is usually subdivided into several large control volumes (zones). Several compartments may be contained in one control volume, while one compartment can also be divided into several control volumes in order to investigate local effects. Energy and mass equations are solved inside control volumes and these volumes are connected by the components called 'junctions' or 'flow paths' through which the hydrodynamic fluids are driven by a momentum equation. The essential difference to CFD codes is that the momentum equations are only for 'junctions' while not associated with control volumes (zones).

The application of L-P approach may therefore introduce inaccuracies, especially in the case of drastic mass transfer or when some parameters in the zones are not homogeneously distributed. Accordingly, when establishing a nodalization of the simulated system, processes which are likely to bring about inaccuracies should be predicted in advance and the corresponding parts of the system should be nodalized more in detail.

One of these L-P codes in common use is MELCOR, which has been developed by Sandia National Laboratories (SNL). As a fully integrated code it is developed to simulate the progression of postulated accidents in light water reactor power plants. Tills et al. [43] had evaluated the adequacy of containment thermal-hydraulic modeling with MELCOR code for application to PWR's passive containment film cooling. A code-to-code benchmark showed that MELCOR's prediction of containment response was equivalent to the containment code CONTAIN.

Another L-P code, the Containment Code System COCOSYS, which is developed by Gesellschaft für Anlagen- und Reaktorsicherheit (GRS), can also simulate plant states during design basis accidents as well as severe accidents in the containment of light water reactors [66]. The code consists of three modules covering thermal hydraulics,

fission products/iodine behavior, and corium behavior.

### 2.3.1.1   *Thermal hydraulic models in COCOSYS*

In the present work, the study of passive containment film cooling is based on thermal hydraulics module of COCOSYS. For this module, the structure of the considered containment or test facility is subdivided into zones.

The thermodynamic state of a zone is defined by the temperature(s) and masses of specified components. Each zone can be subdivided into several zone parts. A zone part can be mainly gaseous, liquid or solid. Gaseous zone parts can contain liquid or solid particles (fog or dust), liquid zone parts can contain dissolved gaseous and solid particles and solid zone parts may contain dissolved gases and liquids as illustrated in Fig. 2-19. In the module, several different zone models have been implemented.
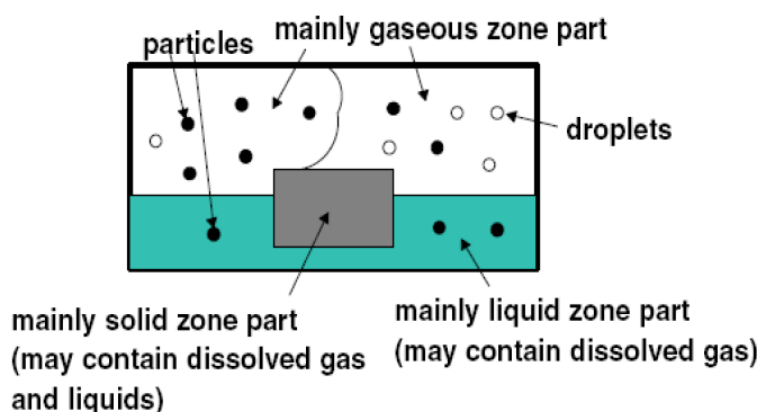


*Fig. 2-19 Generic zone concept in COCOSYS [66]*

**Equilibrium zone model:**

In the equilibrium zone model, all components (liquid water, vapor and other non-condensable gases) in one zone part are assumed to be mixed homogeneously. With the equilibrium zone model, the thermodynamic of the zone volume is determined by the zone temperature (only one value) and the masses of the components in this zone. The model distinguishes between saturated and superheated conditions. Fig. 2-22 presents the principles of this model for both cases. Because only one temperature exists in the zone, the water mass must be zero in the superheated case. If water is injected into a superheated zone, one part of the water flow will be evaporated and the rest will be distributed into other zones.

28

V     time dependent volume

T     temperature

$M_W$   total water mass

$M_{W_c}$   carried water mass

$M_D$   steam mass

$M_1, \ldots,$   total mass of non condensible gases

$M_{1L}, \ldots,$ dissolved mass

$M_{1c}, \ldots,$ gas masses in gas volume $V_{gas}$
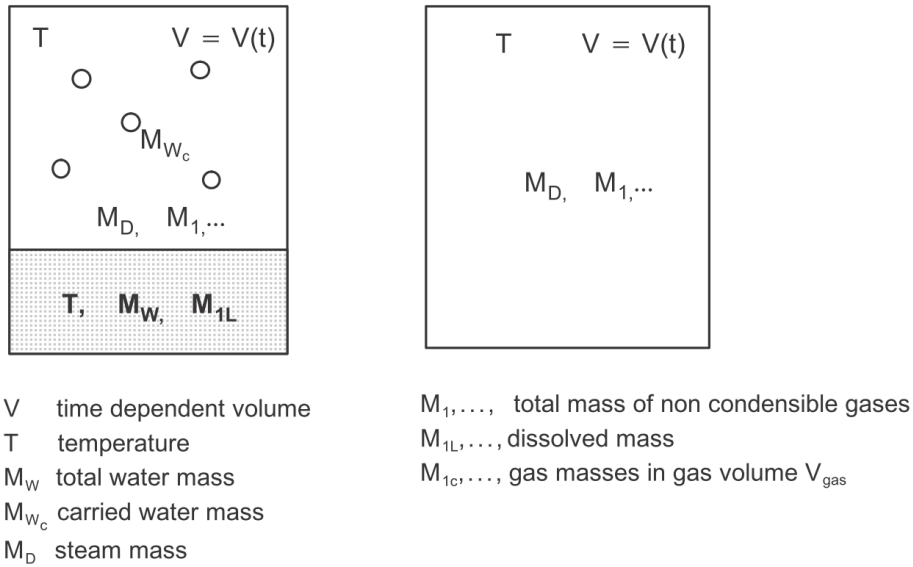
*Fig. 2-20 Concept of an equilibrium zone [66]*

**Non-equilibrium zone model:**

In some cases, the thermodynamic behavior in a containment cannot be described by using only equilibrium models. Due to the high heat capacity of water, it is important for the energy distribution to calculate a correct temperature of liquid water. The atmospheric temperature is a basic boundary condition for different aspects like aerosols, heat transfer to structures etc. Therefore, a zone model, which can provide a separate temperature for the atmosphere and liquid water, is necessary. The principle approach of the non-equilibrium zone model is shown in Fig. 2-21.

Using this model, the zone is subdivided into two parts: the atmosphere part similar to the equilibrium zone model and a sump part (if existing) specified by the temperature and water mass. Between both parts, heat exchange by convection and condensation (or evaporation) correlations is possible.
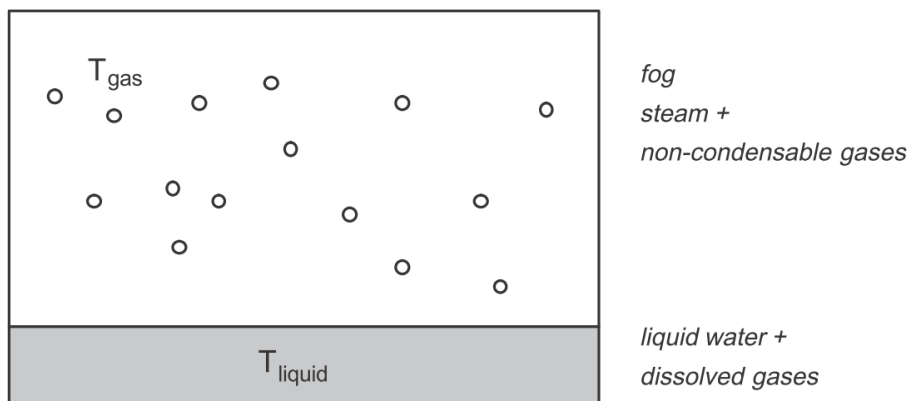


*Fig. 2-21 Principle approach of the non-equilibrium zone model NONEQUILIB*

The junction models in thermal hydraulics module are implemented to enable flow

interaction between zones. Different from other codes such as MELCOR, the gas flow and water drainage between zones in COCOSYS are strongly separated although water can be transported via atmospheric junctions by gas flow and dissolved gases can be transported via drain junctions [66].

Different specific junction models have been applied into the code to adequately provide boundary conditions and simulate specific systems, e.g. rupture discs, atmospheric valves, flaps and specific pressure relief valves. For the simulation of water drainage, several models are implemented, describing the sump balance, water flow through pipes and along walls.

The walls, floors, ceilings and other objects in the simulated system are described as 'structures' which include different types of heat sinks within or between zones. Plate type as well as cylinder type structures with different material properties can be simulated with 'structure' components. The heat flux through the structure is one-dimensional and can be subdivided into layers. The heat exchange between structures and their associated zones are calculated via convection, condensation or radiation, as shown in Fig. 2-22.
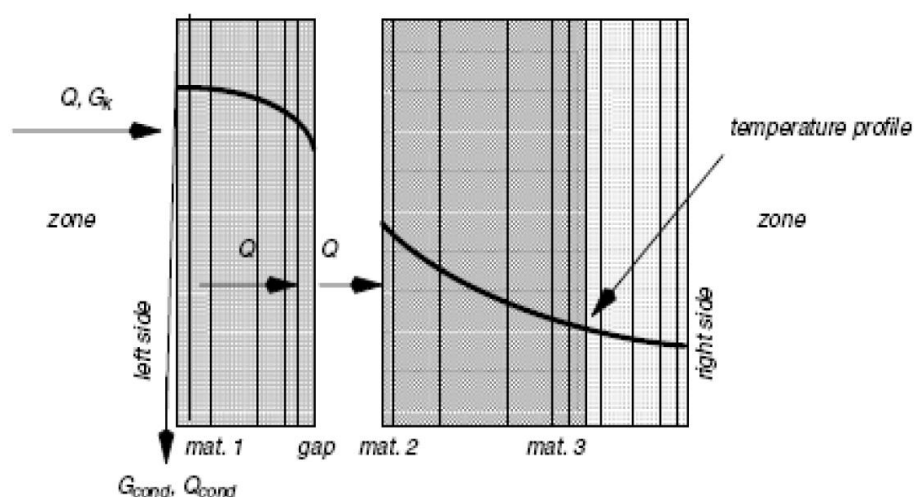


*Fig. 2-22 Generic structure concept in COCOSYS [66]*

Additionally, in order to simulate possible engineered safety features and accident mitigation measures, different types of spray systems, condensers, ventilation systems and catalytic recombiners have been modeled in the code.

## 2.3.2    Simple film model in COCOSYS

The wall condensation model CDW has been developed for COCOSYS to capture condensation of steam and evaporation of liquid film on surfaces of structures and also has been applied for investigating film cooling on the exterior surface of containment shell for AP1000 PCCS [6].

In some cases, the water runs downwards along the structure surface and it leads to a much stronger interaction with the structure and with the zone volume. This behavior can be treated with the DRAIN_WALL junction model in combination with the CDW heat transfer model. In DRAIN_WALL junction model the water flow is assumed to run along the given target structure (Fig. 2-23). In CDW model, velocity distribution complies with Nusselt's theory and water film thickness is calculated with Eq. (2-28) with a prescribed mass flow rate.

$$\delta = \left[ \frac{3\mu_l M}{\rho_l^2 g} \right]^{1/3} \tag{2-28}$$

Assuming condensation/evaporation rate $m_z$ is constant in one cell, as indicated in Fig. 2-23.
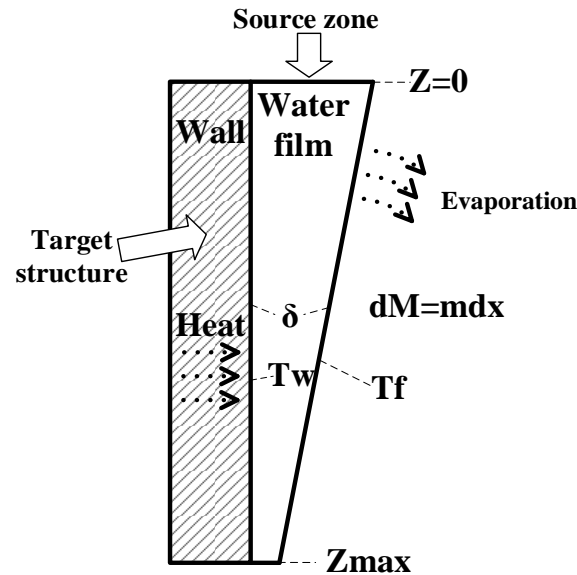


**Fig. 2-23 Evaporation of water film**

Then

$$\delta_z = \left[ \frac{3\mu_l}{\rho_l^2 g} (M + m \cdot z) \right]^{1/3} \tag{2-29}$$

Then the average thickness of water film on a wall control volume is calculated with Eq. (2-30).

$$\overline{\delta} = \frac{1}{Z_{max}} \int_0^{z_{max}} \delta_z dz = \frac{3}{4z} \left( \frac{3\mu_l}{\rho_l^2 g} \right)^{1/3} \cdot \left[ \left( M_{z=0} + mz \right)^{4/3} - \left( M \right)^{4/3} \right] \tag{2-30}$$

31

Where the evaporation/condensation rate $m$ is calculated with Stephan's law in the model: [75]

$$m = A \cdot \beta \cdot \rho_{gas,bulk} \cdot \ln \frac{p_{tot} - p_{Sat}(T_{Film})}{p_{tot} - p_{Vapor}}$$ (2-31)

The equation takes the mass transfer coefficient $\beta$ into account, which depends on a diffusion coefficient, the saturation pressure at the film temperature $p_{Sat}(T_{Film})$ and the partial pressures of vapor and gases, $p_{Vapor}$ and $p_{tot}$, in the bulk with the density $\rho_{gas,bulk}$. Thus, it is obvious that this equation considers the evaporation at surface $A$ as a diffusion problem. It is depending on the amount of non-condensable gases near the film surface. By applying the equivalence of heat and mass transfer, $\beta$ is linked to heat transfer correlations. The temperature difference between the wall temperature $T_{Wall}$ and the film temperature $T_{Film}$ is given by Eq. (2-32) based on the assumption that the convective heat transfer between the wall and film is negligible compared to the heat conduction. Thus, the heat flow into the structure is only dependent on the heat conducted through the film of the thickness $\bar{\delta}$ and the heat conductivity $\lambda_{Film}$.

$$T_{wall} - T_{film} = \frac{q_{evap} \cdot \bar{\delta}}{\lambda_{Film}}$$ (2-32)

The average film thickness $\bar{\delta}$ is depending on the incoming water flow and the condensation/evaporation rate. Heat flux for evaporation $q_{evap}$ is dependent on the temperature difference. Therefore, an iteration is performed to satisfy the energy balance and thus the surface temperature of film is calculated.

### 2.3.3 Study of PCCS film cooling with L-P codes

At SANDIA National Lab assessment of the AP1000 with passive containment film cooling has been conducted by using MELCOR [43]. The nodalization is presented in Fig. 2-24. An accident scenario of double ended guillotine break of the cold leg is considered and the pressure response inside containment is evaluated.
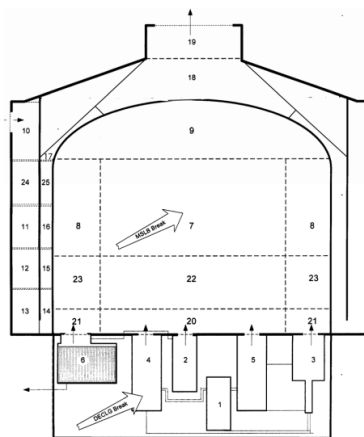


*Fig. 2-24 AP1000 Containment Nodalization Model [43]*

Broxtermann and Allelein [3] used COCOSYS to simulate the accident scenario under LOCA ejection with PCCS film cooling. In this study, the applicability of COCOSYS for the simulation of AP1000's passive containment water film cooling is presented as shown in Fig. 2-25. For this purpose, calculation results of an adopted nodalization from Westinghouse's WGOTHIC code and a nodalization featuring a plume modelling are validated against experimental data of the large scale test facility. Results of the validation show reproducibility of WGOTHIC results with COCOSYS and good agreement of the calculated values using a plume nodalization with the experimental values. The loss of coolant accident peak pressure of AP1000 containment is also evaluated and compared with those calculated with the codes MELCOR and WGOTHIC. The work has demonstrated that COCOSYS can deliver results with evaporating water film on the exterior surface of containment. However, with the original film model in COCOSYS, the effect of film breakup, coverage rate and countercurrent air flow are not taken into account.
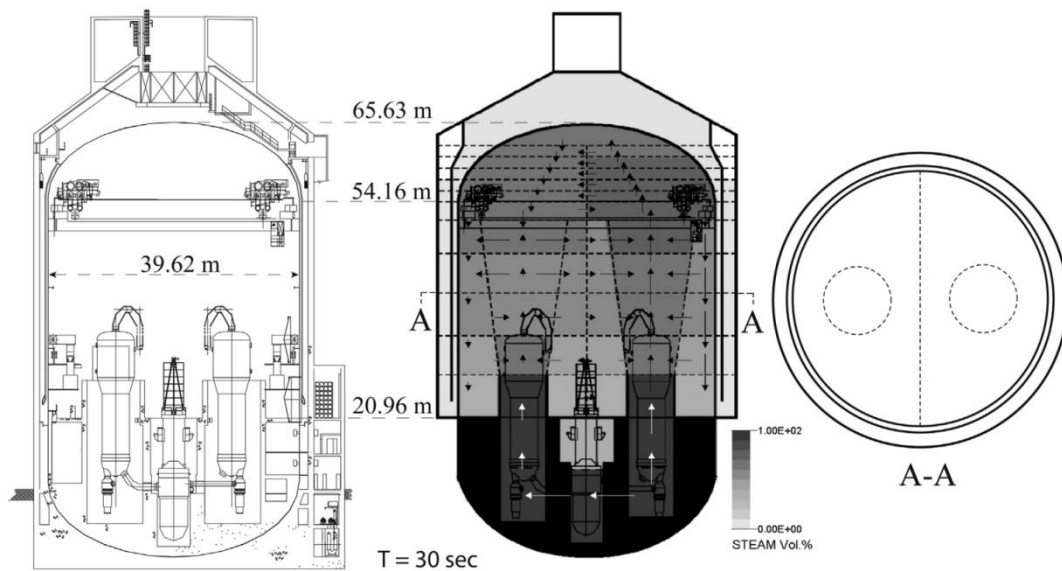


*Fig. 2-25 AP1000 cut view and nodalisation for COCOSYS [3]*

# 3 TEORETICAL BASICS AND METHODOLOGY OF MODELLING

## 3.1 Modelling of advanced film model

The new liquid film model, as an integrated model, involves the consideration of different scenarios of film progression which may occur during the operation of PCCS, e.g., shear stress on the film sheet, which results in a change of film velocity distribution; film breakup with or without countercurrent shear stress; configuration and transformation of film rivulets as well as the transition from fully covered film sheet into rivulets. The new film model introduces the film coverage rate as a new parameter, i.e., the effective fraction of the specific substrate coated with rivulets and film sheet. Different from arbitrarily specifying a coverage rate, which has been used in some containment codes, the new model can provide more realistic prediction and is applicable for the users to predict the film behaviors with different geometries and under different operational conditions.
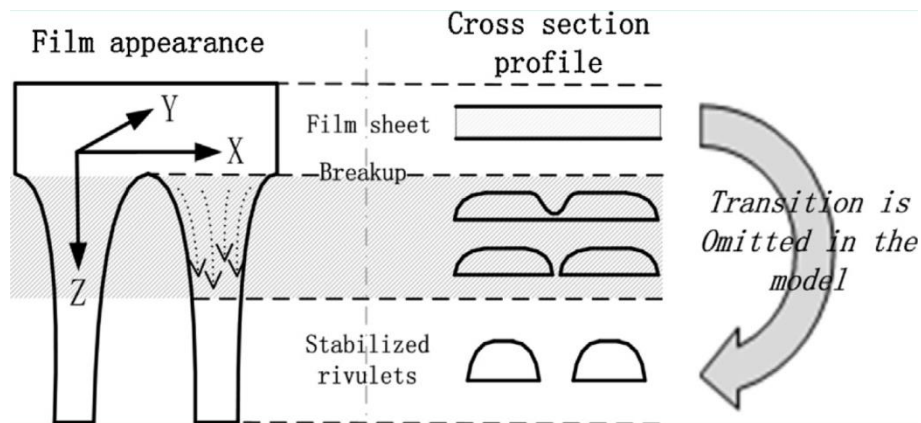


*Fig. 3-1 Formation of rivulets*

It is assumed in the new model that water film on vertical plates is presented either in the form of film sheet or rivulets. The vertical substrate is completely covered by film sheet when water film mass flow is large enough. As the fully covered film breaks up due to the reduction of mass flow rate, stabilized rivulets are formed after the expansion of dry patches and the increase in thickness as illustrated in Fig. 3-1. For COCOSYS, as a lumped parameter code, the scale of control volumes is large enough to omit the transition process from fully covered film to the stable rivulets. Therefore, the stabilized

rivulets are assumed in the new model to be directly connected to the fully covered water film of critical state. Table 3-1 provides the general scheme of the new water film model. The film flow is divided into several stages and all of them are taken into account in the new model. The following sections are specifying the new model stage by stage.

*Table 3-1 The scheme of the newly developed film model*

| Film coating progression | | | Appearance | Cross section | | Description | Contact angle θ |
|---|---|---|---|---|---|---|---|
| | | | | Profile | Equation | | |
| Fully covered water film | | | | | $\phi(x)=\delta$ | The thickness is calculated with the consideration of countercurrent shear at the film surface | N/A |
| Transition from fully covered film to rivulets | Critical thickness of film to break up | | | | $\phi(x)=\delta_{critical}$ | The critical state of the rivulet is reached when the minimum total energy of the film is reached | N/A |
| | Transition stage | | | | No consideration | Believed to be small in scale and omitted in the model | N/A |
| | Stabilized rivulets formed | | | | $\phi(x)=\begin{cases}\delta_{riv,crit}-\dfrac{\delta_{riv,crit}}{1-\cos\theta}\left\{1-\sqrt{1-\left(x-\dfrac{b}{2}\right)^2\left(\dfrac{1-\cos\theta}{\delta_{riv,crit}}\right)^2}\right\} & \left(-\dfrac{b}{2}-a<x<-\dfrac{b}{2}\right)\\ \delta_{riv,crit} & \left(-\dfrac{b}{2}<x<\dfrac{b}{2}\right)\\ \delta_{riv,crit}-\dfrac{\delta_{riv,crit}}{1-\cos\theta}\left\{1-\sqrt{1-\left(x+\dfrac{b}{2}\right)^2\left(\dfrac{1-\cos\theta}{\delta_{riv,crit}}\right)^2}\right\} & \left(\dfrac{b}{2}<x<\dfrac{b}{2}+a\right)\end{cases}$ | The profile of the rivulet is regarded as a circular segment and a film sheet in the middle | $\theta$ |
| Development of rivulets | Invariable width | | | | Ibid. | The contact line or width of the rivulet doesn't change during this process however the contact angle is decreasing as the mass flow rate is reduced, thus the thickness of rivulet is decreasing. When the contact angle reaches the receding contact angle, this process is finished | $\theta$ to $\theta_R$ |
| | Narrowing down of rivulets | Flat sheet | | | $\phi(x)=\begin{cases}\delta-\dfrac{\delta}{1-\cos\theta_R}\left\{1-\sqrt{1-\left(x-\dfrac{b}{2}\right)^2\left(\dfrac{1-\cos\theta_R}{\delta}\right)^2}\right\} & \left(-\dfrac{b}{2}-a<x<-\dfrac{b}{2}\right)\\ \delta & \left(-\dfrac{b}{2}<x<\dfrac{b}{2}\right)\\ \delta-\dfrac{\delta}{1-\cos\theta_R}\left\{1-\sqrt{1-\left(x+\dfrac{b}{2}\right)^2\left(\dfrac{1-\cos\theta_R}{\delta}\right)^2}\right\} & \left(\dfrac{b}{2}<x<\dfrac{b}{2}+a\right)\end{cases}$ | For this stage, the contact angle doesn't change and the rectangular part of the rivulet is shrinking, the height or thickness of rivulet doesn't change for this process | $\theta_R$ |
| | | Circular arc | | | $\phi(x)=\delta-\dfrac{\delta}{1-\cos\theta}\left\{1-\sqrt{1-x^2\left(\dfrac{1-\cos\theta}{\delta}\right)^2}\right\}$ | When rectangular part of the rivulet disappears, the profile will keep as a circular arc and the contact angle is decreasing as the mass flow decreases before the rivulet dries out | $\theta_R$ to 0 |
| Dry out | | | | N/A | N/A | | 0 |

| Film coating progression | | | Appearance | Profile | Film/Rivulets thickness δ or Δ, $\Delta = \delta\left(\rho^3\left(g\sin\alpha\right)^2 / \left(15\mu^2\sigma_{LV}\right)\right)^{1/5}$ | Mass flow rate M $M' = M / \left(\rho\mu\sigma_{LV}^{3} / g\right)^{1/5}$ | Comments |
|---|---|---|---|---|---|---|---|
| Fully covered water film | | |  |  | Solving $\delta^3 + \dfrac{3\tau_i}{2\rho g}\delta^2 - \dfrac{3\mu M}{\rho^2 g} = 0$ numerically | $M = \dfrac{\rho^2 g}{3\mu}\delta^3 + \dfrac{\rho\tau_i}{2\mu}\delta^2$ | Shear stress $\tau_i$ is dependent on thickness $\delta$ |
| Transition from fully covered film to rivulets | | Critical thickness of film to break up |  |  | Obtained by soving polynomial $a_7\delta_{Critical}^{7} + a_6\delta_{Critical}^{6} + \cdots + a_1\delta_{Critical} + a_0 = 0$ | $M_{critical} = \dfrac{\rho^2 g}{3\mu}\delta_{critical}^{3} + \dfrac{\rho\tau_i}{2\mu}\delta_{critical}^{2}$ | The polynomial is obtained based on the minimization of the total energy of liquid film $\left(\frac{E_k + E_s}{M}\right)' = 0$ |
| | | Transition stage |  |  | No consideration | No consideration | This transition stage is short and negligible compared to the scale of zones in L-P codes |
| | | Stabilized rivulets formed |  |  | $\Delta_{riv,crit} = \left(1-\cos\theta\right)^{0.22}\left[1+0.515 U_g^{*2.27}\left(1-\cos\theta\right)^{0.651}\right]$ | $\Gamma_{Critical} = \left(0.67\Delta^{2.83}+0.26\Delta^{9.51}\right)\begin{Bmatrix}1+0.473\left[U_g^{*1.938}\left(1-\cos\theta\right)^{0.556}\right] \\ -1.331\left[U_g^{*9.172}\left(1-\cos\theta\right)^{2.632}\right]\end{Bmatrix}$ for circular arc part and $M_{riv,crit} = \dfrac{\rho^2 g}{3\mu}\delta_{riv,crit}^{3} + \dfrac{\rho\tau_i}{2\mu}\delta_{riv,crit}^{2}$ for the rectangular part | One assumption is that the rivulet is composed of two parts, a circular segment and a rectangle sandwiched in the middle between each semi shape of the circular segment. The thickness of the rivulet part is determined by correlations calculated based on minimum total energy (MTE) theory |
| Development of rivulets | Invariable width | |  |  | Ibid. | Ibid. | Contact angle $\theta$ decreases during this process before retreating contact angle $\theta_R$ is reached at the end of this stage |
| | Narrowing down of rivulets | Flat sheet |  |  | $\Delta = \left(1-\cos\theta_R\right)^{0.22}\left[1+0.515 U_g^{*2.27}\left(1-\cos\theta_R\right)^{0.651}\right]$ | $\Gamma = \left(0.67\Delta^{2.83}+0.26\Delta^{9.51}\right)\begin{Bmatrix}1+0.473\left[U_g^{*1.938}\left(1-\cos\theta_R\right)^{0.556}\right] \\ -1.331\left[U_g^{*9.172}\left(1-\cos\theta_R\right)^{2.632}\right]\end{Bmatrix}$ for circular arc part and $M = \dfrac{\rho^2 g}{3\mu}\delta^3 + \dfrac{\rho\tau_i}{2\mu}\delta^2$ for the rectangular part | |
| | | Circular arc |  |  | | | According to the description of experiment results of Westinghouse [59], all the stripes evaporated completely without changing their characteristic near the point of complete dry out. Thus for the surface test, the liquid film doesn't snap, or draw up into a thick film. |
| Dry out | | |  | N/A | 0 | 0 | |
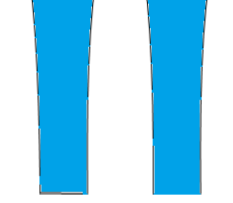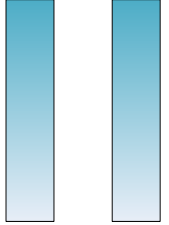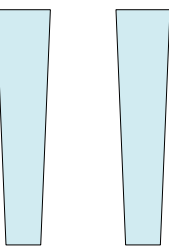
### 3.1.1 Effect of shear stress on film sheet

According to Nusselt's theory, at the film sheet surface, the partial derivative of velocity at the surface is 0.

$$\frac{du_z(y=\delta)}{dy}=0 \tag{3-1}$$

When the shear stress acts on the film surface, the boundary conditions as well as velocity distribution on the cross section are changed, as discussed in chapter 2 (Fig. 2-11). In order to predict the velocity profile, several assumptions have been made. Firstly, it is assumed to have no pressure change in the film along the direction horizontal or perpendicular to the plate. Secondly, there is no slip at the solid - liquid interface. Additionally, the film is assumed to be laminar. Interfacial boundary condition considering shear stress is expressed in Eq. (3-2), which implies the velocity gradient at the film surface is proportional to the shear stress.

$$-\phi'(x)\frac{\partial u(x,\phi)}{\partial x}+\frac{\partial u(x,\phi)}{\partial y}=-\frac{\tau_i(x)}{\mu_l} \tag{3-2}$$

Where $\phi(x)$ describe the profile of the film as shown in Fig. 3-2.
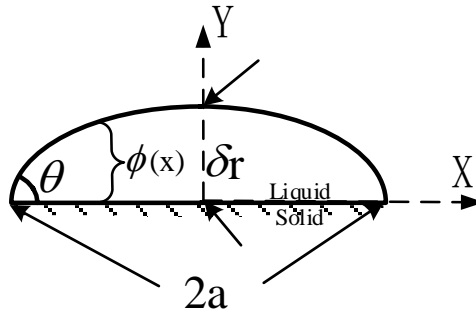


*Fig. 3-2 Cross section profile of film*

The two-dimensional momentum equation:

$$\frac{\partial^2 u}{\partial x^2}+\frac{\partial^2 u}{\partial y^2}=-\frac{\rho_l g \sin\gamma}{\mu_l} \tag{3-3}$$

can be simplified for one dimensional film sheet and expressed as:

$$\frac{\partial^2 u}{\partial y^2}=-\frac{\rho_l g \sin\gamma}{\mu_l} \tag{3-4}$$

Where $\alpha$ indicates the inclination of the targeted structure and $\alpha = 90°$ when the structure is vertical. For the water film sheet as it can be regarded as one-dimensional, the boundary condition Eq. (3-2) is written as:

$$\frac{\partial u(\delta)}{\partial y} = \frac{\tau_i}{\mu_l} \tag{3-5}$$

Then by integrating Eq. (3-4),

$$\frac{\partial u}{\partial y} = -\frac{\rho_l g \sin \gamma}{\mu_l} y + C_1 \tag{3-6}$$

when $y = \delta$,

$$-\frac{\rho_l g \sin \gamma}{\mu_l} \delta + C_1 = \frac{\tau_i}{\mu_l} \tag{3-7}$$

Therefore

$$\frac{\partial u}{\partial y} = -\frac{\rho_l g \sin \gamma}{\mu_l} y + \frac{\rho_l g \sin \gamma}{\mu_l} \delta + \frac{\tau_i}{\mu_l} \tag{3-8}$$

Then by integrating the expression again,

$$u = -\frac{\rho_l g \sin \gamma}{2\mu_l} y^2 + \left( \frac{\rho_l g \sin \gamma}{\mu_l} \delta + \frac{\tau_i}{\mu_l} \right) y + C_2 \tag{3-9}$$

With the non-slip boundary:

$$u(y = 0) = C_2 = 0 \tag{3-10}$$

gives

$$u = \frac{\rho_l g \sin \gamma \delta^2}{\mu_l} \left[ \frac{y}{\delta} - \frac{1}{2} \left( \frac{y}{\delta} \right)^2 \right] + \frac{\tau_i}{\mu_l} y \tag{3-11}$$

The interfacial liquid velocity:

$$u_i = \frac{\rho_l g \sin \gamma}{2\mu_l} \delta^2 + \frac{\tau_i}{\mu_l} \delta \tag{3-12}$$

Where

$$\tau_i = -\frac{1}{2} f_i \rho_g \left( u_i - u_g \right)^2 \tag{3-13}$$

In the case of countercurrent flow, $u_i$ can therefore be calculated:

$$u_i = \frac{\rho_l g \sin \gamma}{2\mu_l} \delta^2 - \frac{f_i \rho_g (u_i - u_g)^2}{2\mu_l} \delta \tag{3-14}$$

or

$$u_i = \left( u_g - \frac{\mu_l}{f_i \rho_g \delta} \right) \pm \sqrt{\left( u_g - \frac{\mu_l}{f_i \rho_g \delta} \right)^2 - \left( u_g^2 - \frac{\rho_l g \sin \gamma \delta}{f_i \rho_g} \right)} \tag{3-15}$$

When $u_i = u_g$, no interfacial shear stress is presented,

From Eq. (3-14),

$$u_i = u_g = \frac{\rho_l g \sin \gamma}{2\mu_l} \delta^2 \tag{3-16}$$

and from Eq. (3-15),

$$u_i = \left( u_g - \frac{\mu_l}{f_i \rho_g \delta} \right) + \sqrt{\left( \frac{\mu_l}{f_i \rho_g \delta} \right)^2 - \frac{2\mu_l u_g}{f_i \rho_g \delta} + \frac{\rho_l g \sin \gamma \delta}{f_i \rho_g}} \tag{3-17}$$

Then from Eq. (3-13),

$$\tau_i = -\frac{1}{2} f_i \rho_g \left( \sqrt{\left( \frac{\mu_l}{f_i \rho_g \delta} \right)^2 - \frac{2\mu_l u_g}{f_i \rho_g \delta} + \frac{\rho_l g \sin \gamma \delta}{f_i \rho_g}} - \frac{\mu_l}{f_i \rho_g \delta} \right)^2 \tag{3-18}$$

The mass flow rate per unit width,

$$
\begin{aligned}
\int_0^\delta \rho_l u(y) dy &= M \\
&= \int_0^\delta \rho_l \left( \frac{\rho_l g \sin \gamma \delta^2}{\mu_l} \left[ \frac{y}{\delta} - \frac{1}{2} \left( \frac{y}{\delta} \right)^2 \right] + \frac{\tau_i}{\mu_l} y \right) dy \\
&= \frac{\rho_l^2 g \sin \gamma}{3\mu_l} \delta^3 + \frac{\rho_l \tau_i}{2\mu_l} \delta^2
\end{aligned} \tag{3-19}
$$

or

$$\delta^3 + \frac{3\tau_i}{2\rho_l g \sin \gamma} \delta^2 - \frac{3\mu_l M}{\rho_l^2 g \sin \gamma} = 0 \tag{3-20}$$

By solving the cubic function, the real root gives the expression of thickness,

$$\delta = \sqrt[3]{\frac{3\mu_l M}{2\rho_l^2 g} - \left(\frac{\tau_i}{2\rho_l g}\right)^3 + \frac{1}{2\rho_l^2 g \sin\gamma}\sqrt{(3\mu_l M)^2 - \frac{3\mu_l M \tau_i^3}{2\rho_l(g\sin\gamma)^2}}}$$

$$+ \sqrt[3]{\frac{3\mu_l M}{2\rho_l^2 g} - \left(\frac{\tau_i}{2\rho_l g}\right)^3 - \frac{1}{2\rho_l^2 g \sin\gamma}\sqrt{(3\mu_l M)^2 - \frac{3\mu_l M \tau_i^3}{2\rho_l(g\sin\gamma)^2}}} - \frac{\tau_i}{2\rho_l g \sin\gamma} \tag{3-21}$$

Where $\tau_i$, as expressed in Eq.(3-18) is a function of $f_i$ determining the thickness of film sheet under interfacial shear.

According to Table 2-2, lots of experiments have been conducted regarding liquid film behavior under countercurrent flow and corresponding empirical expressions regarding $f_i$ are provided. However, most of them are with respect to pipes and tubes. Very few have been found focusing on water film on plates. Among these literatures, only Stephan and Mayinger's research [55] has geometry comparable with PCCS. The drag force coefficient is correlated as:

$$f_i = 0.079\,\mathrm{Re}_g^{-0.25}\left[1 + 115\left(\frac{\delta}{L_L}\right)^N\right] \tag{3-22}$$

where

$$N = 3.95/(1.8 + \frac{3}{Bo}) \tag{3-23}$$

$$Bo = \frac{D_h}{L_L} \tag{3-24}$$

and

$$L_L = (\frac{\sigma}{(\rho_l - \rho_g)g\sin\gamma})^{1/2} \tag{3-25}$$

Therefore the factor $f_i$ is dependent on film thickness. By iteration of the above expressions, with given mass flow rate and shear stress, film thickness and velocity distribution in a film sheet can be determined.

### 3.1.2 Breakup of fully covered film

#### 3.1.2.1 Prediction based on Nusselt's theory

In order to predict film breakup, as discussed in the previous chapter, typical ways including analyzing film stability by imposing a small disturbance on the laminar film, or force balance at the three-phase stagnation point of dry patch formed after film breakup, are both flawed by comparison to the MTE principle. Therefore, the current modification for film breakup is based on the work of Hartley et al. [13], who had obtained the critical thickness of one-dimensional film sheet by minimizing the sum of

kinetic energy and surface energy per unit film width. In this work, the velocity distribution is assumed complying with Nusselt's theory and critical film thickness is given as:

$$\delta_{critical} = 1.34\left(\sigma / \rho_l\right)^{0.2}\left(\mu_l / \rho_l g \sin\gamma\right)^{0.4}$$ (3-26)

And the corresponding critical mass flow rate is:

$$M_{critical} = \frac{\rho_l^2 g \sin\gamma}{3\mu_l}\delta_{critical}^3$$ (3-27)

According to this theory, when the total energy, or namely the sum of kinetic energy and surface energy per unit mass, as indicated in Eq. (3-28), reaches its minimum, the critical state is reached.

$$
\begin{aligned}
\frac{\partial}{\partial\delta}\left(\frac{E_k + E_{sur}}{M}\right) &= \frac{\partial}{\partial\delta}\left\{\frac{1}{M}\left[\int_0^\delta \frac{\rho_l u(y)}{2}u^2(y)dy + \sigma u(\delta)\right]\right\} \\
&= \frac{\partial}{\partial\delta}\left\{\frac{1}{M}\left[\frac{\rho_l}{2}\int_0^\delta u^3(y)dy + \sigma u(\delta)\right]\right\}
\end{aligned}
$$ (3-28)

However in Hartley's model, the velocity distribution is assumed in accordance with Nusselt's theory and the influence of countercurrent air is not taken into account. When a shear stress is present at the film surface, with the velocity distribution expressed in Eq. (3-11), then

$$u^3(y) = \left\{\frac{\rho_l g \sin\gamma\delta^2}{\mu_l}\left[\frac{y}{\delta} - \frac{1}{2}\left(\frac{y}{\delta}\right)^2\right] + \frac{\tau_i}{\mu_l}y\right\}^3$$ (3-29)

or

$$
\begin{aligned}
u^3(y) = &-\frac{\rho^3\left(g\sin\gamma\right)^3}{8\mu_l^3}y^6 + \frac{3\rho_l^2 g^2\left(\rho_l g \sin\gamma\delta + \tau_i\right)}{4\mu_l^3}y^5 \\
&-\frac{3\rho_l g\left(\rho_l g \sin\gamma\delta + \tau_i\right)^2}{2\mu_l^3}y^4 + \left(\frac{\rho_l g \sin\gamma\delta + \tau_i}{\mu_l}\right)^3 y^3
\end{aligned}
$$ (3-30)

When film presents on the vertical substrate, $\sin\gamma = 1$, therefore,

$$\frac{E_k + E_{sur}}{M} = \frac{\left(\begin{array}{l}\dfrac{1}{35}\rho_l^3 g^3\delta^5 + \dfrac{11}{80}\rho_l^2 g^2\tau_i\delta^4 + \dfrac{9}{40}\rho_l g\tau_i^2\delta^3 \\[2mm] +\dfrac{1}{8}\tau_i^3\delta^2 + \dfrac{\mu_l^2\sigma g}{2} + \dfrac{\mu_l^2\sigma}{\rho_l}\tau_i\delta^{-1}\end{array}\right)}{\dfrac{\mu_l^2\rho_l g}{3}\delta + \dfrac{\mu_l^2}{2}\tau_i}$$ (3-31)

Then

$$\frac{\partial}{\partial \delta}\left(\frac{E_k + E_{sur}}{M}\right) =$$

$$\frac{\left(\begin{array}{l}\dfrac{4}{105}\mu_l^2\rho_l^4 g^4\delta^5 + \dfrac{53}{1680}\mu_l^2\rho_l^3 g^3\tau_i'\delta^5 + \dfrac{117}{560}\mu_l^2\rho_l^3 g^3\tau_i\delta^4 + \dfrac{3}{20}\mu_l^2\rho_l^2 g^2\tau_i\tau_i'\delta^4 \\[2mm] +\dfrac{17}{40}\mu_l^2\rho_l^2 g^2\tau_i^2\delta^3 + \dfrac{19}{80}\mu_l^2\rho_l g\tau_i^2\tau_i'\delta^3 + \dfrac{91}{240}\mu_l^2\rho g\tau_i^3\delta^2 + \dfrac{1}{8}\mu_l^2\tau_i'\tau_i^3\delta^2 \\[2mm] +\dfrac{1}{8}\mu_l^2\tau_i^4\delta - \dfrac{2}{3}\mu_l^4 g\sigma\tau_i\delta^{-1} - \dfrac{1}{2}\dfrac{\mu_l^4\sigma}{\rho}\tau_i^2\delta^{-2} + \dfrac{1}{12}\mu_l^4 g\sigma\tau_i' - \dfrac{1}{6}\mu_l^4\rho g^2\sigma\end{array}\right)}{\left(\dfrac{\mu_l^2\rho_l g}{3}\delta + \dfrac{\mu_l^2}{2}\tau_i\right)^2}$$ (3-32)

When the minimum is reached,

$$\frac{\partial}{\partial \delta}\left(\frac{E_k + E_{sur}}{M}\right) = 0$$ (3-33)

or

$$\left(\frac{4}{105}\rho_l^4 g^4 + \frac{53}{1680}\rho_l^3 g^3\tau_i'\right)\delta^7 + \left(\frac{117}{560}\rho_l^3 g^3 + \frac{3}{20}\rho_l^2 g^2\tau_i'\right)\tau_i\delta^6$$

$$+\left(\frac{17}{40}\rho_l^2 g^2 + \frac{19}{80}\rho_l g\tau_i'\right)\tau_i^2\delta^5 + \left(\frac{91}{240}\rho_l g + \frac{1}{8}\tau_i'\right)\tau_i^3\delta^4 + \frac{1}{8}\tau_i^4\delta^3$$

$$+\left(\frac{1}{12}\mu_l^2 g\sigma\tau_i' - \frac{1}{6}\mu_l^2\rho_l g^2\sigma\right)\delta^2 - \frac{2}{3}\mu_l^2 g\sigma\tau_i\delta - \frac{1}{2}\frac{\mu_l^2\sigma}{\rho_l}\tau_i^2$$

$$= 0$$ (3-34)

When the shear stress is absent, $\tau = 0$,

Eq. (3-34) is simplified as,

$$\frac{4}{105}\rho_l^3 g^2\delta^5 - \frac{1}{6}\mu_l^2\sigma = 0$$ (3-35)

Then,

$$\delta = 1.343\left(\mu_l^2\rho_l^{-3} g^{-2}\sigma\right)^{0.2}$$ (3-36)

This is in consistence with the results predicted by D.E. Hartley as indicated in Eq. (3-26). In order to solve Eq. (3-34), the shear stress is linearized as,

$$\tau_i(\delta) \approx \tau_i\left(\delta_{critical}^*\right) + \frac{\partial \tau_i\left(\delta_{critical}^*\right)}{\partial \delta}\left(\delta - \delta_{critical}^*\right)$$ (3-37)

for simplification, where $\tau_i\left(\delta_{critical}^*\right)$ is calculated with Eq.(3-18), and $\tau'\left(\delta_{critical}^*\right)$ is calculated according to

$$\tau_i'(\delta) = -\frac{1}{2} f_i' \rho_g \left( \sqrt{\left(\frac{\mu_l}{f_i \rho_g \delta}\right)^2 - \frac{2\mu_l u_g}{f_i \rho_g \delta} + \frac{\rho_l g \delta}{f_i \rho_g} - \frac{\mu_l}{f_i \rho_g \delta}} \right)^2$$

$$-f_i \rho_g \left( \sqrt{\left(\frac{\mu_l}{f_i \rho_g \delta}\right)^2 - \frac{2\mu_l u_g}{f_i \rho_g \delta} + \frac{\rho_l g \delta}{f_i \rho_g} - \frac{\mu_l}{f_i \rho_g \delta}} \right) \cdot \left\{ \left[ \left(\frac{\mu_l}{f_i \rho_g \delta}\right)^2 - \frac{2\mu_l u_g}{f_i \rho_g \delta} + \frac{\rho_l g \delta}{f_i \rho_g} \right]^{-\frac{1}{2}} \cdot \left[ \begin{array}{c} -\dfrac{\mu_l^2 \rho_g (f_i' \delta + f_i)}{(f_i \rho_g \delta)^3} \\[2mm] +\dfrac{\mu_l u_g (f_i' \delta + f_i)}{\rho_g f_i^2 \delta^2} \\[2mm] +\dfrac{\rho_l g (f_i - \delta f_i')}{2\rho_g f_i^2} \end{array} \right] + \frac{\mu_l}{f_i \rho_g \delta^2} \right\} \qquad (3\text{-}38)$$

And $\delta_{critical}^*$ is the critical film thickness calculated from the previous iteration. For the first iteration step, the prediction of Hartley et al., similar to Eq. (3-26), is used.

$$\delta_{critical}^0 = 1.343 \left( \mu_l^2 \rho_l^{-3} g^{-2} \sigma \right)^{0.2} \qquad (3\text{-}39)$$

If

$a = \tau'\left(\delta_{critical}^*\right), b = \tau\left(\delta_{critical}^*\right) - \delta_{c0}\tau'\left(\delta_{critical}^*\right)$, then Eq. (3-34), can be simplified as:

$$a_7 \delta_{Critical}^7 + a_6 \delta_{Critical}^6 + \cdots + a_1 \delta_{Critical} + a_0 = 0 \qquad (3\text{-}40)$$

where

$$a_7 = \frac{4}{105} \rho_l^4 g^4 + \frac{101}{420} a \rho_l^3 g^3 + \frac{23}{40} a^2 \rho_l^2 g^2 + \frac{37}{60} a^3 \rho_l g + \frac{1}{4} a^4$$

$$a_6 = \frac{117}{560} b \rho_l^3 g^3 + ab \rho_l^2 g^2 + \frac{129}{80} a^2 b \rho_l g + \frac{7}{8} a^3 b$$

$$a_5 = \frac{17}{40} b^2 \rho_l^2 g^2 + \frac{11}{8} ab^2 \rho_l g + \frac{9}{8} a^2 b^2$$

$$a_4 = \frac{91}{240} b^3 \rho_l g + \frac{5}{8} ab^3$$

$$a_3 = \frac{1}{8} b^4 \qquad (3\text{-}41)$$

$$a_2 = -\frac{7}{12} \mu_l^2 g \sigma a - \frac{1}{6} \mu_l^2 \rho_l g^2 \sigma - \frac{1}{2} a^2 \frac{\mu_l^2 \sigma}{\rho_l}$$

$$a_1 = -\frac{2}{3} b \mu_l^2 g \sigma - ab \frac{\mu_l^2 \sigma}{\rho_l}$$

$$a_0 = -\frac{1}{2} \frac{\mu_l^2 \sigma}{\rho_l} b^2$$

The critical film thickness under shear stress created by countercurrent air can be obtained by numerically solving the Eq. (3-37) to Eq. (3-41). The critical mass flow rate is expressed as:

$$M_{Critical} = \int_0^{\delta_{Critical}} \rho_l u(y) dy$$

$$= \int_0^{\delta_{Critical}} \rho_l \left( \frac{\rho_l g \delta_{Critical}^2}{\mu_l} \left[ \frac{y}{\delta_{Critical}} - \frac{1}{2} \left( \frac{y}{\delta_{Critical}} \right)^2 \right] + \frac{\tau_{i,Critical}}{\mu_l} y \right) dy \qquad (3\text{-}42)$$

$$= \frac{\rho_l^2 g}{3\mu_l} \delta_{Critical}^3 + \frac{\rho_l \tau_{i,Critical}}{2\mu_l} \delta_{Critical}^2$$

where

$$\tau_{i,Critical}$$

$$= -\frac{1}{2} f_{i,\delta_{Critical}} \rho_g \left( \sqrt{\left( \frac{\mu_l}{f_{i,\delta_{Critical}} \rho_g \delta_{Critical}} \right)^2 - \frac{2\mu_l u_g}{f_{i,\delta_{Critical}} \rho_g \delta_{Critical}} + \frac{\rho_l g \delta_{Critical}}{f_i \rho_g}} - \frac{\mu_l}{f_i \rho_g \delta_{Critical}} \right)^2 \qquad (3\text{-}43)$$

When the breakup takes place at an inclined surface, $g$ is replaced by $g\sin\gamma$ in the equations.

### *3.1.2.2 Prediction based on other correlations*

As discussed in chapter 2, one of the limitations of Nusselt's theory is the assumption of smooth surface. When the wave is generated on the surface of water film, velocity distribution may be changed and doesn't comply with Nusselt's theory. Therefore the kinetic energy as well as critical film mass flow rate and critical film thickness may be changed. Accordingly, by taking this effect into consideration, the critical state of falling film without countercurrent air on the film surface is derived.

Table 2-1 provides empirical correlations which approximate the results of time averaged film thickness. Based on Nusselt's correlation, all these works have introduced the film thickness predictions with similar form:

$$\delta = a' \text{Re}^{b'} \left( v_l^2 / g \right)^{1/3} \qquad (3\text{-}44)$$

It's believed that the influence of wave is reflected with different coefficients $a'$ and $b'$ in these correlations. Assuming no slip exists at the solid - liquid interface and the velocity distribution in the film is parabolic:

$$u(y) = \alpha' y^2 + \beta' y \qquad (3\text{-}45)$$

When no shear stress is imposed on the surface:

$$\frac{\partial u(\delta)}{\partial y} = 0 \qquad (3\text{-}46)$$

Then the velocity distribution can be calculated and according to Eq. (3-28) and Eq. (3-33), when the total energy is minimized, the critical thickness can be calculated:

$$\delta_{Critital} = \left( \frac{9}{140} \right)^{\frac{b'}{b'-2}} a'^{\frac{2}{2-b'}} \left( \frac{1}{b'} - 1 \right)^{\frac{b'}{b'-2}} \mu_l^{\left( \frac{6b'-4}{3b'-6} \right)} \rho_l^{\left( \frac{4-3b'}{3b'-6} \right)} g^{\frac{2}{3b'-6}} (\sin\gamma)^{\frac{2}{3b'-6}} \sigma^{\frac{b'}{2-b'}} \qquad (3\text{-}47)$$

And the critical mass flow rate is given by:

$$M_{Critical} = \frac{1}{4}\mu_l a'^{-\frac{1}{b'}} \left(\frac{\mu_l^2}{\rho_l^2 g \sin \gamma}\right)^{-\frac{1}{3b'}} \delta_{Critical}^{\frac{1}{b'}}$$ (3-48)

Among these correlations in Table 2-1, the work of Yu is related to PCCS conditions and therefore can be used to replace Nusselt's expression in predicting critical film thickness. The critical thickness and mass flow rate are expressed as:

$$\delta_{Critital} = 0.72\mu_l^{0.31}\rho_l^{-0.578} \left(g \sin \gamma\right)^{-0.422} \sigma^{0.267}$$ (3-49)

$$M_{Critical} = 0.25\mu_l a'^{-2.37} \left(\frac{\mu_l^2}{\rho_l^2 g \sin \gamma}\right)^{-0.79} \delta_{Critical}^{2.37}$$ (3-50)

### 3.1.2.3 *Test of film breakup model under countercurrent air*

Saber et al. [17] have derived the critical rivulet height under interfacial shear by considering minimum total energy. Critical rivulet height, which is different from the critical thickness of fully covered water film, indicates the height of stable rivulet formed after the breakup. In their model, the drag force factor is predicted with Grolmes Lambert and Fauske's equation: [47]

$$f = 0.006 + \overline{A}\delta^2 \left(\mu_l / \mu_R\right)^{-0.44}$$ (3-51)

where $\overline{A} = 2 \times 10^6 m^{-2}$ and $\mu_R$ is a reference liquid viscosity $=1.0$cP [17]. In the present work, the drag force factor suggested by Stephan and Mayinger, [55] is applied for the prediction of critical thickness under countercurrent flow as well. Fig. 3-3 shows the comparison of critical film thickness/rivulet height with different models. Saber's model [17] is focusing on the critical height of rivulets and therefore the contact angles are specified. These results under different contact angles show sharp increase of critical thickness by increasing countercurrent air flow.

The model with Grolmes's drag force factor [47] for fully covered water film, as indicated by the green dotted curve, also presents a steep increase of critical rivulet height. As shown, use of Stephan's drag force factor demonstrates a much smaller increase in film thickness as the air flow increases as shown in Fig. 3-3.
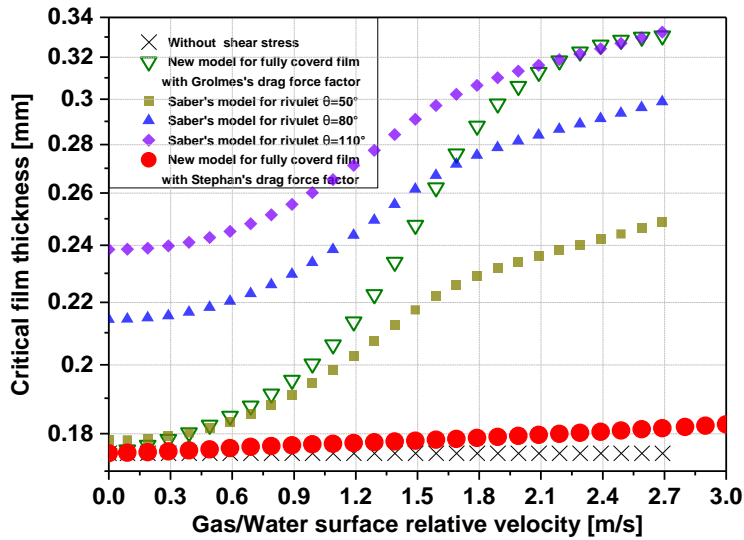
*Fig. 3-3 Change of critical film thickness over gas/water relative velocity*

According to Yu's experiment, the countercurrent gas doesn't significantly increase the critical thickness for the breakup of fully covered film and however, the critical mass flow rate for breakup will be even reduced under the countercurrent air flow for some cases. It's speculated that in these cases the countercurrent air may have flattened the wavy film [12]. This indicates that the contribution of interfacial shear stress to the critical film thickness is not significant.

### 3.1.3    Rivulet behavior

#### 3.1.3.1    Configuration of rivulets

After the breakup, the film coating goes to another stage that the fully covered film is transformed into numerous rivulets and dry patches appear among these rivulets. According to the theory of Doniec [14, 15], the equilibrium, stationary free surface of the flowing rivulet is formed when the minimum total energy of the system is fulfilled. The study also indicates that for each specific contact angle between the attaching liquid and substrate, there is one corresponding equilibrium/critical height of a rivulet [16, 30, 31, 58, 68 ].

This complicated pattern of rivulet flow is simplified in the new model. It's assumed that all the rivulets have identical profiles and are distributed unanimously on the substrate. Thus, several mean values of each rivulet including the contact angle and the profile should be specified.

As assumed in many previous studies on the profile of rivulets, when it reaches critical state, the profile of the critical state of rivulet is regarded as a circular segment in the new model, as demonstrated in Fig. 3-4, and expressed as:

48
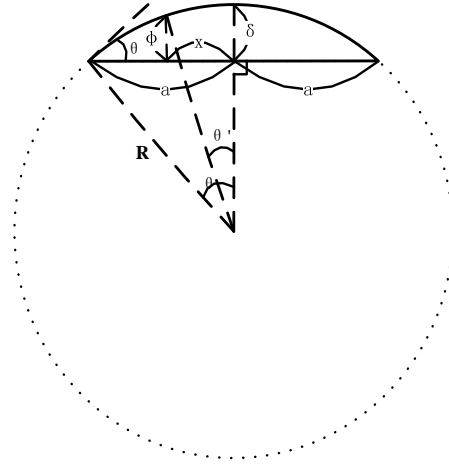
*Fig. 3-4 Cross section profile of the rivulet at critical state*

$$\phi(\theta') = R(\cos\theta' - \cos\theta)$$ (3-52)

Where $0 < \theta' < \theta$, the half width of the rivulet

$$a = R\sin\theta$$ (3-53)

and the rivulet height

$$\delta = R(1 - \cos\theta)$$ (3-54)

To convert it into Cartesian coordinates,

$$x = R\sin\theta$$ (3-55)

Combining Eq. (3-52) with Eq. (3-54) gives,

$$\phi = \frac{\delta}{1-\cos\theta}(\cos\theta' - \cos\theta)$$ (3-56)

and with Eq. (3-55) and Eq. (3-56),

$$x = \frac{\delta}{1-\cos\theta}\sin\theta'$$ (3-57)

Rearrange Eq. (3-57) yields,

$$\sqrt{1 - x^2\left(\frac{1-\cos\theta}{\delta}\right)^2} = \cos\theta'$$ (3-58)

Insert Eq. (3-58) into Eq. (3-56) gives,

$$\phi = \frac{\delta}{1-\cos\theta}\left(\sqrt{1 - x^2\left(\frac{1-\cos\theta}{\delta}\right)^2} - \cos\theta\right)$$ (3-59)

or

$$\phi = \delta - \frac{\delta}{1-\cos\theta}\left[1 - \sqrt{1 - x^2\left(\frac{1-\cos\theta}{\delta}\right)^2}\right]$$ (3-60)

The half width of rivulet is

$$a = R\sin\theta = \frac{\sin\theta}{1-\cos\theta}\delta \tag{3-61}$$

Based on the profile indicated in Eq.(3-60), El-Genk and Saber [16] has predicted the critical thickness of rivulet with a specified contact angle by using MTE principle. In their work, a direct method to find an approximate solution for boundary value problems, which is referred to as Ritz method, instead of zero order or first order approximation, is applied to approximate the velocity distribution in the rivulet. Semi-empirical dimensionless correlations in a simple form are obtained to express the relationship between contact angle and the minimum rivulet height and minimum rivulet mass flow rate.

$$\Delta_{Critical} = (1-\cos\theta)^{0.22} \tag{3-62}$$

$$\Gamma_{Critical} = 0.67\Delta_{critical}^{2.83} + 0.26\Delta_{critical}^{9.51} \tag{3-63}$$

It turns out that prediction with the expressions above shows much better accuracy by comparing with other previous correlations as listed in Table 2-3, especially for large values of contact angle. Therefore, the expressions proposed by El-Genk et al., Eq. (3-62) and Eq. (3-63), are used in the new model to predict the height and mass flow rate of the critical state of equilibrium state of stationary rivulet, where $\Delta = \delta / \left[15\mu_l^2\sigma/(\rho_l^3 g^2)\right]^{0.2}$ indicates dimensionless film thickness for critical state $\Gamma = M / \left[\rho_l\mu_l\sigma^3/g\right]^{0.2}$ denotes dimensionless flow rate per unit width.

Another question is that how the geometry of rivulet changes, assuming that the contact angle stays as constant, when the flow rate is beyond the critical value. Doniec [14, 15] proposed that the rivulet width would increase in such a case and its thickness would not change. This point of view is also supported by other studies, e.g. El-Genk & Saber [16]. Fig. 3-5 demonstrates the configuration of the rivulet with the flow rate beyond the critical value.
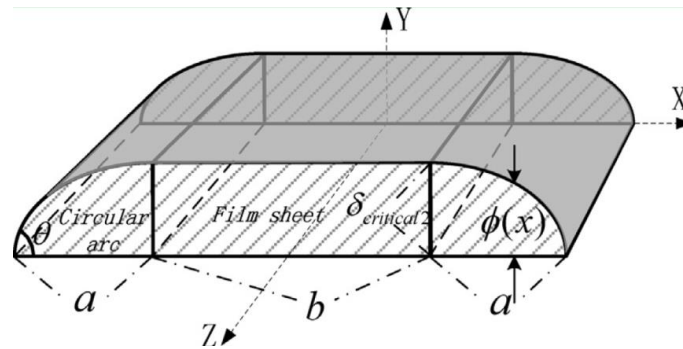


*Fig. 3-5 Profile of rivulet when a film sheet is present in the middle*

In this case, the profile of the rivulet cross section is regarded as a circular segment and a rectangular film sheet in the middle, where $a$ and $b$ are the width of circular segment and width of rectangular part respectively.

Similarly, when mass flow rate decreases down to the critical value, the rectangular part of the rivulet disappears by narrowing the width and the rivulet cross section profile consists of only a circular arc. At the same time, the critical or minimum mass flow rate for a typical contact angle is reached. Afterwards, if the mass flow rate keeps reducing,

according to the description of experiment results in the document [63], all the stripes evaporate completely without changing their characteristic for the surface test, the liquid film doesn't snap, or draw up into a thicker film.

Consequently, assumption is made that if the mass flow rate keeps reducing, in order to maintain its circular arc profile, and to satisfy the relationship between the contact angle and the minimum flow rate in terms of MTE method, the film thickness as well as the contact angle of the rivulet tends to decrease simultaneously. The rivulet would adjust its profile by reducing the contact angle in order to satisfy the corresponding flow rate, as illustrated in Fig. 3-6.
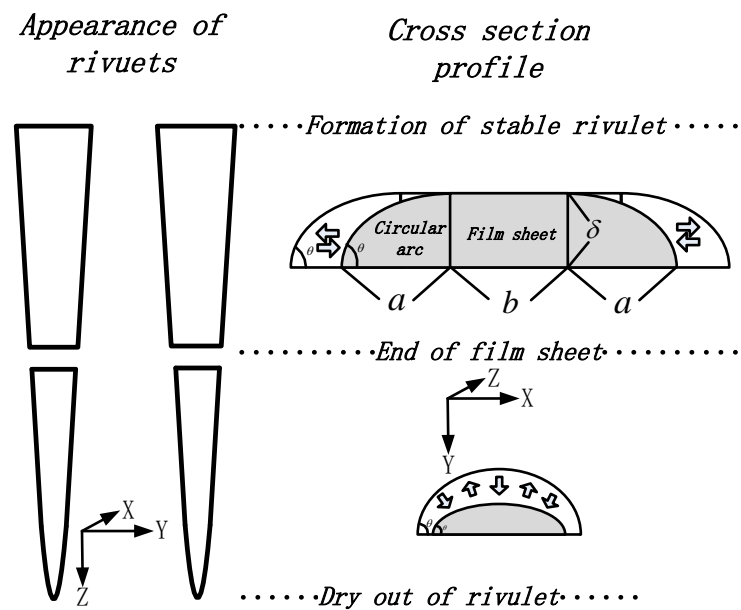


Fig. 3-6 Development of rivulets by reducing mass flow rate

### 3.1.3.2    *Rivulet under shear stress*

When the rivulet is under interfacial shear, Saber et al. [17] showed the prediction of critical thickness and mass flow rate of the rivulet considering inclination of substrate and shear stress. By using a similar method as El-Genk et al. [16] dimensionless semi-empirical correlations are provided concerning the critical state of rivulets. The effect of inclination of the substrate is expressed by:

$$\Delta_{Critical,\alpha} = \Delta_{Critical} \left( \sin \gamma \right)^{-0.4} \tag{3-64}$$

$$\Gamma_{Critical,\alpha} = \Gamma_{Critical} \left( \sin \gamma \right)^{-0.2} \tag{3-65}$$

The effect of counter-current interfacial shear is given by:

$$\Delta_{Critical,\gamma,co} = \Delta_{Critical,\gamma} \left[ 1 + 0.515 U_g^{*2.27} \left( 1 - \cos \theta \right)^{0.651} \right] \tag{3-66}$$

Dimensionless mass flow rate for stable water rivulet under countercurrent shear stress is:

$$\Gamma_{Critical,\gamma,co}$$
$$= \Gamma_{Critical,\gamma} \left\{ 1 + 0.473 \left[ U_g^{*1.938} \left(1 - \cos\theta\right)^{0.556} \right] - 1.331 \left[ U_g^{*9.172} \left(1 - \cos\theta\right)^{2.632} \right] \right\} \qquad (3\text{-}67)$$

Where the dimensionless gas velocity $U_g^*$ is expressed as:

$$U_g^* = u_i \nu_l / \left[ g \left( 15\mu_l^2 \sigma / (\rho_l^3 g^2) \right)^{0.4} \right] \qquad (3\text{-}68)$$

These semi-empirical correlations from Eq. (3-64) to Eq. (3-68) are adopted for the new model to predict the height of rivulets under shear stress.

### 3.1.3.3    Rivulet hysteresis

For any given solid-liquid contact, there exists a range for the contact angle. When the contact line of the rivulet is expanding or contracting, the contact angles are known as advancing contact angle $\theta_A$ or retreating contact angle $\theta_R$ respectively. The advancing contact angle refers to the maximum contact angle by increasing the mass flow and this angle stays invariable during the process of advancing. On the other hand, the retreating contact angle suggests the minimum contact angle in the process of reducing mass flow. Similarly, this contact angle stays constant when the rivulet is retreating. When the contact angle is between these two values, the contact line is stable even though the mass flow rate is increasing or reducing. When rivulets are formed after breakup, the initially formed rivulets are present with the equilibrium contact angle, which is within the range between the advancing and the retreating contact angles. These processes are shown in Fig. 3-7.
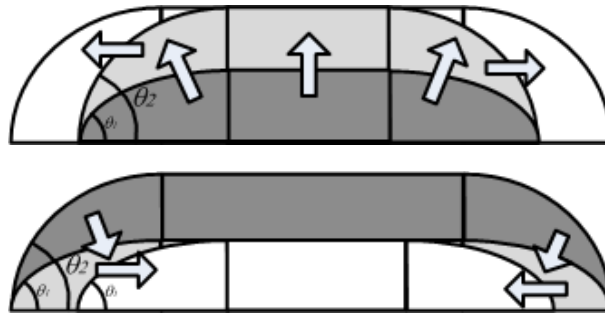


*Fig. 3-7 Rivulet profile change within the range of hysteresis (Upper: advancing; Lower: Retreating)*

In the new film model, it is possible to take the phenomenon of hysteresis into account. When this new feature is activated, the user needs to specify 3 different contact angles: advancing one $\theta_A$; retreating one $\theta_R$ and equilibrium one $\theta$. The contact angle after breakup is considered as at the equilibrium state, thus the contact angle is $\theta$. Afterwards, as the rivulet is being evaporated, the thickness of the rivulet and the contact angle are reducing while the contact line and the coverage rate are unchanged. When the advancing or the retreating contact angles is reached, the motion pattern of the rivulet takes the mode introduced in the last section.

### 3.1.4 Determination of the initial rivulet configuration

At the initial point of film breakup, as suggested by Lan et al. [76], fluids with higher surface tension or with higher contact angle exhibit higher rate of decrease of width in stream wise direction. As a result, the present dry patches will be amplified downwards due to the constriction of rivulets. In an L-P code such as COCOSYS, control volumes are of large size and film sheet is considered converted into stabilized and constricted rivulets directly, and the transition process is neglected.

In order to describe the patterns of rivulet flow, the initial coverage rate of rivulets after the transition process from fully covered film into rivulets after breakup needs to be determined, which determines the effective fraction of film coverage and is defined as:

$$\alpha = \frac{2a+b}{2a+b+\lambda} \tag{3-69}$$

where $\lambda$ represents the width of the dry patch between two rivulets. As shown in Fig. 3-8, which depicts the profile of the cross section after the transition from fully covered film to stabilized rivulets, the rivulet is constricted and its height is increased as the dry patch appears.
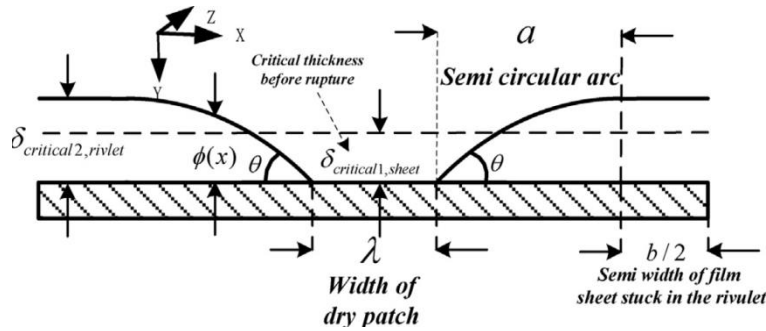


**Fig. 3-8 Transition from fully covered film to rivulets.**

So far, for the initial state of rivulets after breakup, the thickness and profile of rivulets can be determined by specifying a contact angle. Mass flow rate in the film sheet and the circular arc (both parts belong to rivulets) part can be calculated by considering velocity distribution on the cross section and applying empirical correlations.

Once the width of the rectangular part in the middle of the rivulet is fixed, the number of rivulets can be calculated by mass balance. The width of dry patch and subsequently the initial coverage rate of water film after break up is determined. In order to find out the width of the rectangular part of the rivulet, total energy equivalence for the film flow before and after breakup is adopted for the new model and expressed in Eq. (3-70), which indicates that the energy per unit width after breakup is the same as that before the breakup.

$$\frac{dE_{break}}{dx} = \frac{E_{arc} + E_{sheet'}}{2a+b+\lambda} = \frac{E_{arc} + b\left(\dfrac{dE_{sheet'}}{dx}\right)}{2a+b+\lambda} \tag{3-70}$$

Where $\dfrac{dE_{break}}{dx}$ is the per unit width total energy before breakup, and

$$E_{arc} = E_{k,arc} + E_{sur,arc} \tag{3-71}$$

is the total energy of the circular part of the rivulet, while $E_{sheet'}$ is the total energy of the rectangular film sheet in the middle of the rivulet, $2a + b + \lambda$ the width of each rivulet-dry patch system, $a$ the semi-width of circular part of the rivulet, as defined in Eq.

$$a = R\sin\theta = \frac{\sin\theta}{1 - \cos\theta}\delta \tag{3-61},$$

$b$ the width of rectangular film sheet. The energy of rectangular film sheet before breakup equals to the sum of kinetic energy and surface energy.

$$E_{break} = E_{sheet,\delta_{break}} = E_{k,sheet} + E_{sur,sheet} \tag{3-72}$$

Thus,

$$dE_{break} = \int_0^{\delta_{break}} \frac{1}{2}\rho_l u^2(y)dy + \sigma$$
$$= \frac{1}{2}\rho_l \int_0^{\delta_{break}} u^2(y)dy + \sigma \tag{3-73}$$

Since

$$u(y) = \frac{\rho_l g\delta^2}{\mu_l}\left[\frac{y}{\delta} - \frac{1}{2}\left(\frac{y}{\delta}\right)^2\right] + \frac{\tau_i}{\mu_l}y \tag{3-74}$$

Therefore,

$$dE_{break} = \frac{1}{2}\rho_l \int_0^{\delta_{break}} u^2(y)dy + \sigma$$
$$= \frac{\rho_l^3 g^2}{15\mu_l^2}\delta_{break}^5 + \frac{5\rho_l^2 g\tau_i}{24\mu_l^2}\delta_{break}^4 + \frac{\rho_l\tau_i^2}{6\mu_l^2}\delta_{break}^3 + \sigma \tag{3-75}$$

The kinetic energy and the surface tension energy of the arc are expressed as:

$$E_{k,arc} \approx 2a\left(\frac{\rho_l^3 g^2}{15\mu_l^2}\bar{\delta}_{arc}^5 + \frac{5\rho_l^2 g\tau_i}{24\mu_l^2}\bar{\delta}_{arc}^4 + \frac{\rho_l\tau_i^2}{6\mu_l^2}\bar{\delta}_{arc}^3\right) \tag{3-76}$$

$$E_{sur,arc} = \int_{-a}^{a}\left[\sigma\sqrt{1 + \left(\frac{d\phi}{dx}\right)^2}\right]dx = \frac{2a\theta}{\sin\theta}\sigma \tag{3-77}$$

Similarly, the energy of rectangular film sheet consists of two parts,

$$E_{sheet'} = E_{k,sheet'} + E_{sur,sheet'} \tag{3-78}$$

$$dE_{sheet'} = \frac{\rho_l^3 g^2}{15\mu_l^2}\delta_{riv}^5 + \frac{5\rho_l^2 g\tau_i}{24\mu_l^2}\delta_{riv}^4 + \frac{\rho_l\tau_i^2}{6\mu_l^2}\delta_{riv}^3 + \sigma \tag{3-79}$$

where $\delta_{riv}$ is the height of the rivulet calculated according to contact angle.

According to mass and energy balance,

$$\begin{cases} M_{break} = \dfrac{2aM_{riv} + bM_{sheet'}}{2a + b + \lambda} \\ dE_{break} = \dfrac{E_{arc} + b \cdot dE_{sheet'}}{2a + b + \lambda} \end{cases} \qquad (3\text{-}80)$$

The dry patch width and the width of the film sheet can be determined:

$$\begin{cases} \lambda = \dfrac{\left(2aM_{break} - 2aM_{arc}\right)\left(dE_{break} - dE_{sheet'}\right) - \left(E_{arc} - 2a \cdot dE_{break}\right)\left(M_{sheet'} - M_{break}\right)}{dE_{break}\left(M_{break} - M_{sheet'}\right) - M_{break}\left(dE_{break} - dE_{sheet'}\right)} \\ b = \dfrac{2a\left(M_{break} - M_{arc}\right) + \lambda M_{break}}{M_{sheet'} - M_{break}} \end{cases} \qquad (3\text{-}81)$$

Thus, the initial coverage rate, $\alpha = \dfrac{2a + b}{2a + b + \lambda}$ is determined.

With these expressions above, some test calculations have been performed to find out the relationship between the semi-width of the circular segments and the width of film sheet part in the middle b. The results indicate that the ratio between these two widths, $2a/b$, is quite small and negligible for the initial status of the rivulets just after breakup. One example of such calculations is shown in Table 3-2 and Table 3-3.

*Table 3-2 Properties and parameters for the test calculations*

| Parameters | Liquid density | Liquid-gas Surface tension | Viscosity | Wall temperature | Ambient Pressure | $u_g - u_i$ (countercurrent) |
|---|---|---|---|---|---|---|
| Units | kg/m$^3$ | N/m | Pa s | K | Pa | m/s |
| Values | 995 | 0.072 | $7.2 \times 10^{-4}$ | 307 | $1.01 \times 10^5$ | 0.85 |

*Table 3-3 Results of the test calculations*

| Contact angle $\theta$ | Width of circular segment $2a$ | Width of each film sheet in the middle $b$ | Initial coverage rate | Ratio $2a/b$ |
|---|---|---|---|---|
| Degree | m | m | N/A | N/A |
| 90 | $7.12 \times 10^{-4}$ | 0.153 | 0.486 | $4.65 \times 10^{-3}$ |
| 80 | $8.14 \times 10^{-4}$ | 0.161 | 0.550 | $5.06 \times 10^{-3}$ |
| 70 | $9.28 \times 10^{-4}$ | 0.179 | 0.639 | $5.18 \times 10^{-3}$ |
| 60 | $10.6 \times 10^{-4}$ | 0.238 | 0.765 | $4.45 \times 10^{-3}$ |
| 55 | $11.34 \times 10^{-4}$ | 0.342 | 0.848 | $3.32 \times 10^{-3}$ |
| 50 | $12.18 \times 10^{-4}$ | 0.985 | 0.952 | $1.24 \times 10^{-3}$ |

The results indicate that the semi-width of the circular part of rivulet are quite small and are less than 1 percent of the width of the film sheet. Thus, when implementing the model described above into the code, the profile of the circular part can be equalized or even neglected in some processes for simplification.

### 3.1.5   The special condition for breakup

As introduced in the previous sections, in the new model both mass and energy balance have been taken into account for the transition from fully covered water film to rivulets. The height of rivulets in the model is the critical rivulet thickness proposed by El-Genk and Saber, which is calculated by specifying the contact angle between liquid and solid substrate.

This assumption brings about two different situations:

Firstly, if the contact angle between rivulets and the substrate is large enough, the rivulets formed after breakup will have higher thickness than that of the fully covered film at critical state, the constriction of rivulets will take place in this case.

As shown in Fig. 3-9, which is extracted from Xu's work [56], where stainless steel is used as the substrate material, and an obvious decrease of coverage rate occurs after breakup. For this situation, the model introduced in the previous sections is used for the prediction of the critical state of breakup as well as the initial formation of rivulets after the breakup.
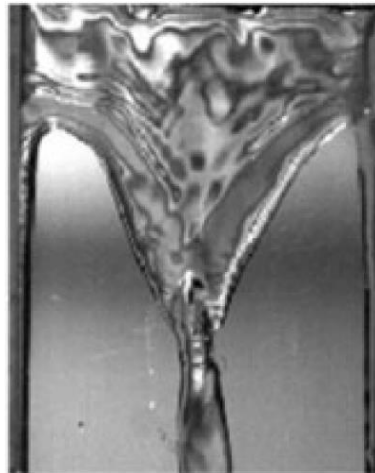


*Fig. 3-9 Sudden constriction of coverage rates [56]*

On the other hand, when the contact angle of the rivulets is quite small, the critical height of the rivulets is even smaller than the thickness of fully covered film at critical state, the coverage rate calculated by considering mass and energy balance might be large than 1.0. In other words, the fully covered water film has reached its critical state in this case, while the rivulets - dry patch pattern on the substrate cannot be formed or maintained. It's assumed in this case that the critical film thickness is smaller than the value predicted with MTE criterion and is in accordance with the critical height of the rivulet on this particular material.

This assumption can be confirmed according to the Yu's experiment [12]. When the liquid mass flow rate is decreasing, it's observed that the water film has gone through an unstable period before the sustainable dry patches are formed. During this period, dry patches are temporarily formed and flooded randomly. It's believed that this unstable period occurs when the critical height of rivulets is smaller than critical thickness of the fully covered film calculated with MTE criterion.

As indicated in Fig. 3-10, which is cited from Yu's experiment [12], the coverage rate doesn't change significantly until the water mass flow rate declines to as low as 35g/m/s, while the critical mass flow rate predicted with MTE theory for the fully covered film is about 103g/m/s. The real minimum thickness of the fully covered film is about 0.21mm while the predicted value is 0.316 mm. The contact angle derived according to El-Genk's correlation is about 21°. This small contact angle reflects the ideal wettability of the substrate and this is believed to be attributed to the surface treatment with special zinc coating for this test. The figure also denotes under this condition that the coverage rate doesn't decrease sharply and the constriction of film doesn't take place.
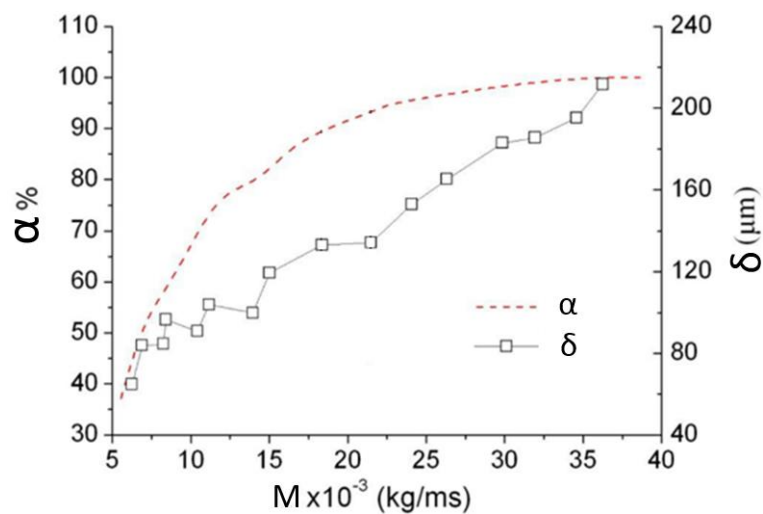


*Fig. 3-10 Relationship between mass flux and coverage rate; average film thickness [12]*

## 3.2 Implementation of the model into the code

In the previous section, the basic methodology to model the falling film progression has been provided. These derivations represent only the local values such as film thickness and rivulet height at a certain elevation. Nevertheless, further processing is still required in order to implement them into COCOSYS.

In COCOSYS, the liquid film is attaching the wall structure. As a lumped parameter code, each structure is of large size and only some averaged values need to be provided and are used for the calculation of other modules, i.e. the averaged surface temperature of the structure covered by film, averaged film thickness used for calculating the temperature and the coverage rate on the entire structure.

Accordingly, the status of the film on the targeted wall structure can be divided into several different situations and the coverage rate and averaged film thickness on the entire structure needs to be considered separately. Three representative situations considered differently are demonstrated as follows.

**Situation 1**

For the first situation, as shown in Fig. 3-11, the structure is fully covered with liquid
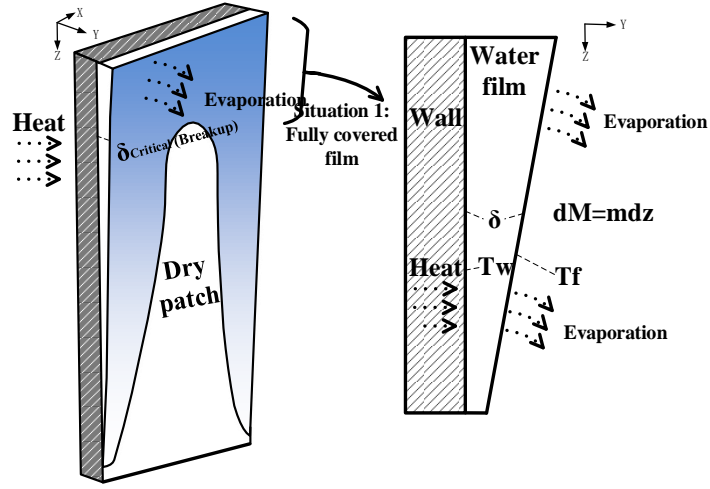
film.



*Fig. 3-11 Situation 1: fully covered film*

As introduced in the previous section, the relationship between film thickness and mass flow rate per unit width is:

$$M = \frac{\rho_l^2 g}{3\mu_l} \delta^3 + \frac{\rho_l \tau_i}{2\mu_l} \delta^2 \tag{3-82}$$

The local mass flow rate at the position $z$ is:

$$M_z = \frac{\rho_l^2 g}{3\mu_l} \delta_z{}^3 + \frac{\rho_l \tau_i}{2\mu_l} \delta_z{}^2 \tag{3-83}$$

The evaporation rate $m$ and in the targeted structure is regarded as constant, then

$$M_z = M_0 + mz = \frac{\rho_l^2 g}{3\mu_l} \delta_z^3 + \frac{\rho_l \tau_i}{2\mu_l} \delta_z^2 \tag{3-84}$$

Where $M_0$ denotes the inlet mass flow rate per unit length at this control volume. The inlet film thickness $\delta_0$ is calculated with Eq. (3-21), then

$$\delta_0 = \sqrt[3]{\frac{3\mu_l M_0}{2\rho_l^2 g} - \left(\frac{\tau_i}{2\rho_l g}\right)^3 + \frac{1}{2\rho_l^2 g} \sqrt{\left(3\mu_l M_0\right)^2 - \frac{3\mu_l M_0 \tau_i{}^3}{2\rho_l g^2}}}$$

$$+ \sqrt[3]{\frac{3\mu_l M_0}{2\rho_l^2 g} - \left(\frac{\tau_i}{2\rho_l g}\right)^3 - \frac{1}{2\rho_l^2 g} \sqrt{\left[3\mu_l M_0\right]^2 - \frac{3\mu_l M_0 \tau_i{}^3}{2\rho_l g^2}}} - \frac{\tau_i}{2\rho_l g} \tag{3-85}$$

And

$$\delta_z = \sqrt[3]{\frac{3\mu_l \left(M_0 + mx\right)}{2\rho_l^2 g} - \left(\frac{\tau_i}{2\rho_l g}\right)^3 + \frac{1}{2\rho_l^2 g} \sqrt{\left[3\mu_l \left(M_0 + mz\right)\right]^2 - \frac{3\mu_l \left(M_0 + mz\right)\tau_i{}^3}{2\rho_l g^2}}}$$

$$+ \sqrt[3]{\frac{3\mu_l \left(M_0 + mz\right)}{2\rho_l^2 g} - \left(\frac{\tau_i}{2\rho_l g}\right)^3 - \frac{1}{2\rho_l^2 g} \sqrt{\left[3\mu_l \left(M_0 + mz\right)\right]^2 - \frac{3\mu \left(M_0 + mz\right)\tau_i{}^3}{2\rho_l g^2}}} - \frac{\tau_i}{2\rho_l g} \tag{3-86}$$

According to Simpson's rule, the averaged film thickness on the targeted film is

approximated as:

$$\overline{\delta} = \frac{\int_0^{z_{max}} \delta(z) dx}{z_{max}} \approx \frac{1}{6}\left(\delta_0 + 4\delta_{z_{max}/2} + \delta_{z_{max}}\right) \qquad (3\text{-}87)$$
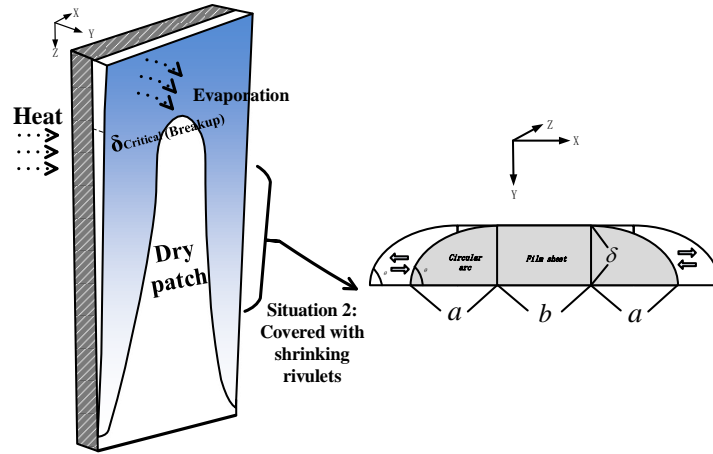
Since the structure is fully covered, the averaged coverage rate,

$$\overline{\alpha} = 1.0 \qquad (3\text{-}88)$$

Then with Eq. (2-31) and Eq. (2-32) as indicated in the previous chapter, the averaged film thickness as well as the film surface temperature are obtained after iteration.

## Situation 2

For the second situation, as shown in Fig. 3-12, the structure is covered with constricting rivulets.



*Fig. 3-12 Situation 2: Covered with shrinking rivulets*

When the targeted structure is covered with constricting rivulets and the film sheet is presented in the middle of the rivulet, then $a$, the semi width of the circular segment can be calculated with Eq. (3-61) according to the specified contact angle. With the inlet width of $b_0$ and coverage rate $\alpha_0$, the coverage rate at position z is calculated as:

$$\alpha(z) = \frac{2a + b(z)}{(2a + b_0)/\alpha_0} \qquad (3\text{-}89)$$

Since the circular part of the rivulet will not be deformed before the film sheet in the middle disappears, thus

$$d\alpha = d\left[\frac{2a+b}{(2a+b_0)/\alpha_0}\right]$$
$$= \frac{2a}{(2a+b_0)/\alpha_0} + \frac{1}{(2a+b_0)/\alpha_0} db \qquad (3\text{-}90)$$

The change of the mass flow rate in the film sheet equals to the evaporation rate of the rivulet.

$$d\left(M_{sheet}b\right)=M_{sheet}db$$
$$=\left(2a\bar{m}_{circ}+bm_{sheet}\right)dz$$

(3-91)

The average evaporation rate over the circular arc is:

$$\int_{Circular}m_xdx=2a\bar{m}_{circ}$$

(3-92)

This leads to

$$\frac{db}{2a\bar{m}_{circ}+bm_{sheet}}=\frac{dz}{M_{sheet}}$$

(3-93)

By integrating Eq.(3-93) gives

$$Ce^{\frac{m_{sheet}}{M_{sheet}}z}=2a\bar{m}_{circ}+b_zm_{sheet}$$

(3-94)

Then

$$b\left(z\right)=\frac{Ce^{\frac{m_{sheet}}{M_{sheet}}z}-2a\bar{m}_{circ}}{m_{sheet}}$$

(3-95)

Because

$$b\left(0\right)=b_0$$

(3-96)

therefore,

$$C=2a\bar{m}_{circ}+b_0m_{sheet}$$

(3-97)

and

$$b\left(z\right)=\frac{\left(2a\bar{m}_{circ}+b_0m_{sheet}\right)e^{\frac{m_{sheet}}{M_{sheet}}z}-2a\bar{m}_{circ}}{m_{sheet}}$$

(3-98)

The parameters $a$ and $b$ at the outlet are:

$$\alpha_{max}=\frac{2a+b_{max}}{\left(2a+b_0\right)/\alpha_0}$$

(3-99)

$$b_{max}=\frac{\left(2a\bar{m}_{circ}+b_0m_{sheet}\right)e^{\frac{m_{sheet}}{M_{sheet}}z_{max}}-2a\bar{m}_{circ}}{m_{sheet}}$$

(3-100)

The coverage rate on the targeted structure:

$$\overline{\alpha} = \frac{1}{z_{\max}} \int_0^{z_{\max}} \frac{2a + b(z)}{(2a + b_0)/\alpha_0} dz$$

$$= \frac{1}{z_{\max}} \int_0^{z_{\max}} \left[ \frac{2a + \dfrac{\left(2a\overline{m}_{circ} + b_0 m_{sheet}\right) e^{\frac{m_{sheet}}{M_{sheet}}z} - 2a\overline{m}_{circ}}{m_{sheet}}}{(2a + b_0)/\alpha_0} \right] dz \qquad (3\text{-}101)$$

$$= \frac{2a\alpha_0}{2a + b_0} - \frac{2a\overline{m}_{circ}\alpha_0}{m_{sheet}(2a + b_0)} + \frac{\alpha_0 M_{sheet}\left(2a\overline{m}_{circ} + b_0 m_{sheet}\right)}{m_{sheet}^2 z_{\max}(2a + b_0)} \left( e^{\frac{m_{sheet}}{M_{sheet}}z_{\max}} - 1 \right)$$

Since $2a$ is negligible compare to $b_0$,

$$\overline{\alpha} \approx \frac{\alpha_0 M_{sheet}}{m_{sheet} z_{\max}} \left( e^{\frac{m_{sheet}}{M_{sheet}}z_{\max}} - 1 \right)$$

$$= \frac{M_{in}}{m_{sheet} z_{\max}} \left( e^{\frac{m_{sheet}}{M_{sheet}}z_{\max}} - 1 \right) \qquad (3\text{-}102)$$

The film thickness under this condition is in accordance with the critical height of rivulets.

$$\overline{\delta} = \delta_{r,\text{crit}} \qquad (3\text{-}103)$$

## Situation 3

For the third situation, when the targeted structure is covered with rivulets and the film sheet is dried out, then the profile of rivulet is only a circular segment, as shown in Fig. 3-13.
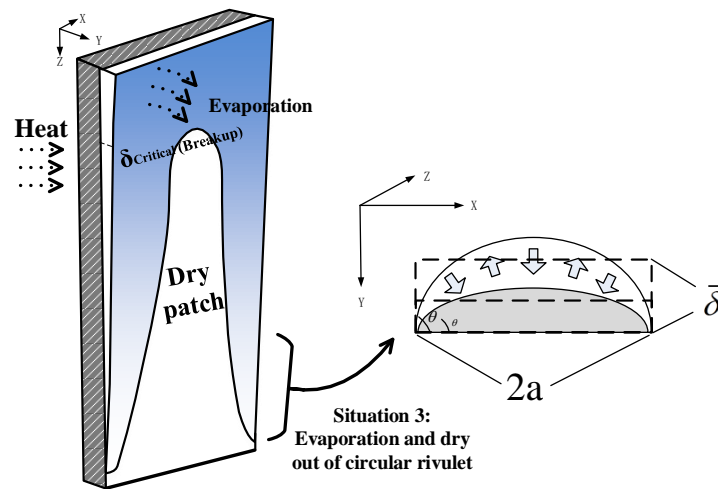


**Fig. 3-13 Situation 3: Covered with rivulets, film sheet is not presented**

Experimental results [59] as well as computing results have shown that, the width of the stabilized rivulets are much larger than the width of the circular rim at each edge of the rivulets, $b \gg 2a$, as indicated in Table 3-3. Therefore, when the film sheet in the middle is completely dried out, the remnant film rivulets are quite small in terms of width and mass flow rate. Accordingly, based on the profile of circular segment introduced in Fig. 3-4, the averaged inlet rivulet height is calculated as:

$$
\begin{aligned}
\delta_0 &= \frac{1}{2a} \int_{-a}^{a} \phi(x) dx = \frac{1}{2a} \int_{-a}^{a} \sqrt{R^2 - x^2} dx + \left( \delta_{critical\,2} - R \right) \\
&= \frac{R\theta}{2\sin\theta} + \frac{R\cos\theta}{2} + \delta_{critical\,2} - R
\end{aligned}
\tag{3-104}
$$

Or

$$
\delta_0 = \delta_{riv,crit} + \frac{\delta_{riv,crit}}{1 - \cos\theta} \left( \frac{\theta}{2\sin\theta} + \frac{\cos\theta}{2} - 1 \right)
\tag{3-105}
$$

The averaged film thickness on the targeted film is approximated according to Simpson's rule as well, as indicated in Eq. (3-87). Then the evaporation rate is approximated with the averaged film thickness $\bar{\delta}$. Nevertheless, the width of the rivulet ($2a$) is too small compare to other stages and doesn't remarkably affect the cooling process, therefore it is negligible.

# 4 VALIDATION AND ASSESSMENT OF THE NEW WATER FILM MODEL

## 4.1 Validation of the new model

Plenty of experimental data concerning falling film behaviors can be found in the open literature and many of these experiments are conducted on test facilities of relatively small scale. Moreover, these experiments are mostly concentrating on one or two particular film behaviors. The new integrated liquid film model in COCOSYS can therefore be validated stage by stage in accordance with different categories of these experiments. Nevertheless some of the phenomena considered in the new model are quite subtle and related test data are not found from literature. Table 4-1 shows the overview of different phenomena which are taken into account in the new film model. The source of the experimental data which are used for validation are presented as well.

*Table 4-1 Status of the model validation*

| Phenomenon/Parameters | Model | Test results |
|---|---|---|
| Thickness of falling film without countercurrent flow | Nusselt's theory (Eq. (2-28)) | Hopf et al. [70], Dukler et al. [69], Roy et al. [71], Ambrosini et al. [38], Zhou et al. [72], Yu et al [12]. |
| Thickness of falling film under countercurrent flow | Newly developed model based on Stephan's drag force factor (Eq. (3-22)) | Yu et al. [12], Roy et al. [71] |
| Critical state of falling film without countercurrent flow | Minimum total energy theory provided by Hartley et al. (Eq. (3-27)) | Hoffmann et al. [33, 74] |
| Critical state of falling film with countercurrent flow | Newly developed model based on Hartley's study (Eq. (3-40)) | N. A. |
| Initial state of newly formed rivulets | Newly developed model considering mass and energy equivalence (Eq. (3-69)) | N. A. |

| | | |
|---|---|---|
| Rivulet height | Theory of El-Genk and Saber (Eq. (3-62) ~ (Eq. (3-66)) | Gajewski et al. [21] |
| Rivulet structure | Assumption widely used | N. A. |
| Phenomenon of hysteresis | Newly developed model considering advancing and retreating contact angle | Gajewski et al. [21], Description from the report of Westinghouse [59] |

### 4.1.1 Film thickness of free falling liquid film

When countercurrent air is not presented, the shear stress on the interface between liquid and air is negligible. As indicated by Dukler and Bergelin [69], when the Reynolds number of liquid film remains small, the time averaged thickness generally complies with Nusselt's theory with only a slight deviation. Nevertheless, as Reynolds number increases, Nusselt's prediction tends to deviate from the test results due to the generation of large scale wave and instability. It is necessary to figure out the range of Re within which this theory is applicable.

Fig. 4-1 shows the comparison of dimensionless film thickness, which is expressed as:

$$\Delta_2 = \delta \left( \rho_l^2 g \sin \gamma / \mu_l^2 \right)^{1/3} \tag{4-1}$$

The comparison between Nusselt's prediction and experimental results from literature, which focus on the water film behaviors on the plate [12, 38, 69-72], reveals that for a relatively low Re of less than 1500, the Nusselt's prediction of film thickness is generally in agreement with most of these experimental data. However, as Re increases, the prediction tends to underestimate the film thickness. The figure clearly demonstrates that for large Re, due to the transition from laminar to turbulent film flow, almost all fitted curves of these experiments exceed Nusselt's prediction. For typical PCCS application, since the largest flow rate is about 27 kg/s [43], Re number is presumably less than 1500 throughout the operation process. Accordingly, Nusselt's theory is available to predict the thickness of free falling water film on a vertical plate in the new model.
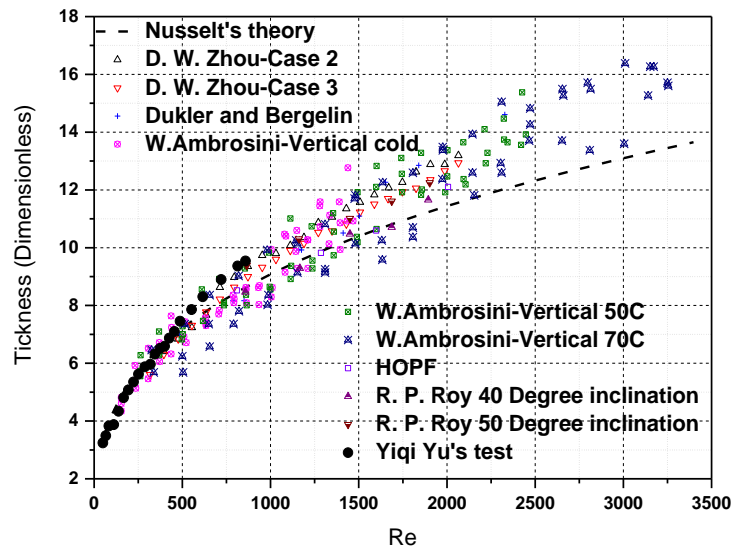
*Fig. 4-1 Comparison of film thickness between Nusselt's prediction and tests*

## 4.1.2 Film thickness under countercurrent air

When the countercurrent air flow is acting at the surface of the water film, the velocity distribution is changed due to the change of boundary condition. As introduced in previous chapter, the shear stress $\tau_i$ can be calculated by considering the relative velocity between gas and film surface. In order to calculate the drag force coefficient $f_i$, Stephan & Mayinger's [55] correlation has been selected for the new model.

The comparison between experimental data and simulation results indicate that most of drag force models, especially those derived from pipe experiments of small scale, tend to overestimate the effect of shear stress on a vertical plate. Calculated film thickness based on Stephan and Mayinger's drag force model is compared with Yu's experiment [12] and Roy's experiment [71] respectively, which have been conducted on steel plates with countercurrent air flow. Acomparison of results is shown in Fig. 4-2 and Fig. 4-3.

In Roy's experiment, characteristics of thin water film flow down a plane surface with and without superposed countercurrent air flow were studied. Experiments were performed initially at zero air flow and then increasing the air flow rate in steps until water entrainment occurred [71]. For each countercurrent air velocity, five film Reynolds numbers were studied.

In Yu's study [12], experimental studies on water film falling and spreading on a large vertical flat plate are carried out. The experiments aim at investigating the flow characteristics of a falling film. In this experiment, countercurrent air is also imposed on the surface of falling film.

As indicated in Fig. 4-2, the Re number in Yu's experiment is completely within the range of PCCS, and in Roy's experiment the Re number is relatively large, as shown in Fig. 4-3. For both cases, the calculated film thickness agrees well with experimental

data. Consequently, Stephan and Mayinger's model is suitable for the prediction of water film thickness on the PCCS external containment shell under countercurrent air flow conditions.
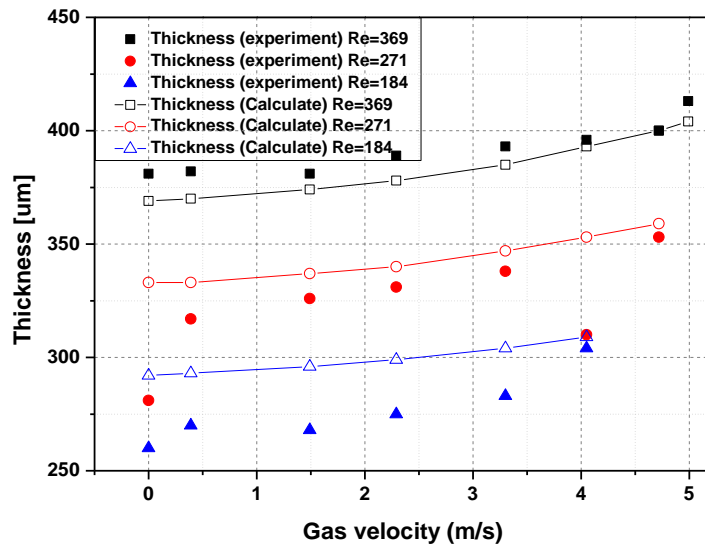


*Fig. 4-2 Film thickness under countercurrent flow conditions (calculated results compared with Yu's experiment [12])*
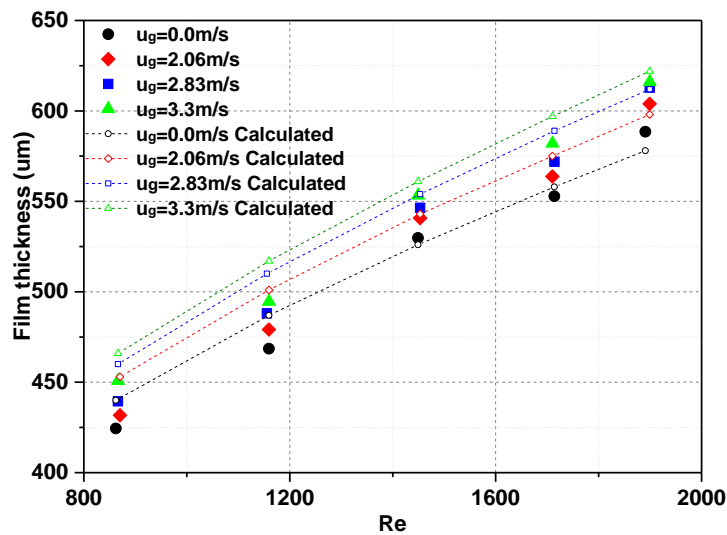


*Fig. 4-3 Film thickness under countercurrent flow conditions (calculated results compared with Roy's experiment [71])*

### 4.1.3  Breakup of free falling film

In the new model, the critical thickness, below which the film starts to break up, is predicted with the minimum total energy criterion introduced by Hartley et al. [13]. The critical film thickness for the fully covered situation is expressed with Eq. (3-26), the critical mass flow rate is therefore calculated with Eq. (3-27). The wetted fraction or coverage rate on the vertical or inclined plate, defined as the ratio of the wetted plate area to the total plate area, is reported in some literature [12, 33, 74]. In Hoffmann's experiment [33, 74], water spreads on a polished steel plate, the coverage rate is measured as the mass flow rate changes.

Square dots in Fig. 4-4 are captured from Hofmann's experimental study [33, 74], which show the coverage rate measured on a steel plate with 60° inclination and without countercurrent air flow. In this experiment, the plate is perfectly covered with water film with large Re number. When Re decreases, the water flow rate on the plate cannot support a fully covered state, and film starts to break up so that coverage rate decreases. The critical Re, as indicated in the figure, is between 630 and 690 while Hartley's correlation, as indicated in Eq. (3-27), gives the value of 498, and under evaluates the critical Re for about 25%. According to Eq. (3-27), the actual critical thickness in the experiment of Fig. 4-4 is between 378 $\mu m$ and 389 $\mu m$, about 10% larger than the predicted value of 350 $\mu m$.
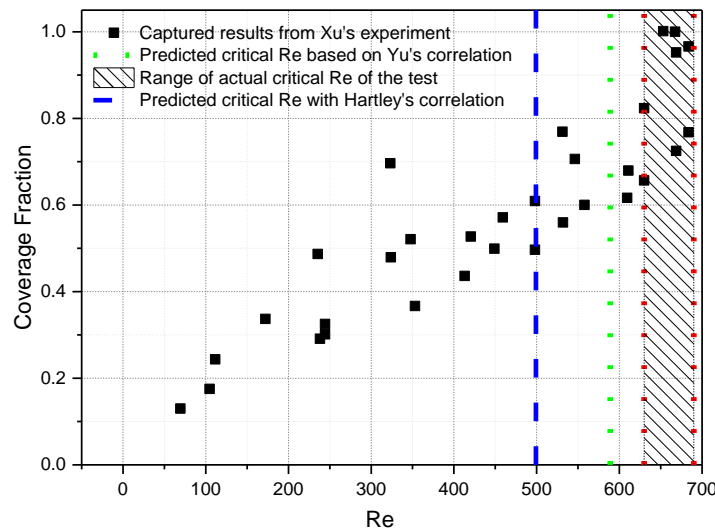


***Fig. 4-4 Change of coverage rate with Re number predicted with minimum total energy criterion***

This deviation is believed to be resulted by the discrepancy between the assumption and the real velocity distribution. Accordingly, Eq. (3-47) and Eq. (3-48) with coefficients proposed by Yu et al. [33] are used to replace Nusselt's expression for the minimum total energy calculation. As shown in Fig. 4-4, compared to the prediction of Nusselt's theory, MTE approach with Yu's coefficients gives a better prediction of the

film critical state. The critical Re number is underestimated for less than 10%. Accordingly, for predicting critical state of fully covered water film, Eq. (3-47) and Eq. (3-48), provide more accurate results.

### 4.1.4 Rivulet behavior

The phenomenon of hysteresis is observed in lots of experiments such as those conducted by Westinghouse [63] and Yu [12]. It's revealed that by increasing or reducing the mass flow rate, the stable rivulets won't be expanded or narrowed before the contact angles have reached typical values. These typical values of contact angle are 'Advancing contact angle' and 'Retreating contact angle' as explained in Chapter 3. However, due to the difficulty of measuring contact angles, very few experimental studies have considered these two factors simultaneously. The only relevant information is found from the experimental data of Andrzej Gajewski [21].

From Fig. 4-5 to Fig. 4-8 the relationship between contact angle and film thickness on aluminum and brass are presented. The experiment data are captured from Andrzej Gajewski's research [21]. In these figures, the rivulet critical thickness, which is proposed by El-Genk et al. [16] in a dimensionless form, is shown as well. It's revealed that the critical thickness predicted with the semi-empirical equation Eq. (3-62) is significantly lower than the measured values. In order to match the experimental data, the expression above is corrected by adjusting the exponent value from 0.22 to 0.045. In the following figures (Fig. 4-5 to Fig. 4-8), the test results and calculated results are presented altogether. It's revealed that the corrected equation improves the results of thickness and flow rate significantly and shows good agreement with experiment data.
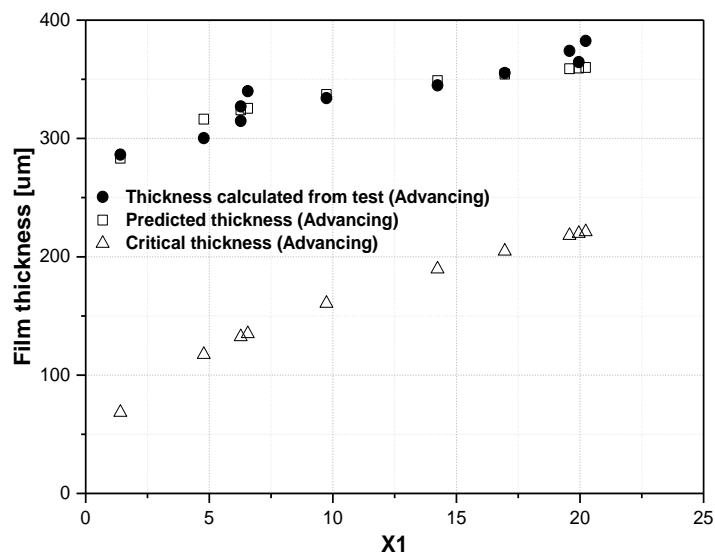


*Fig. 4-5 Thickness vs. contact angle (Increase flow rate, aluminum surface with a roughness of 1.38 μm)*
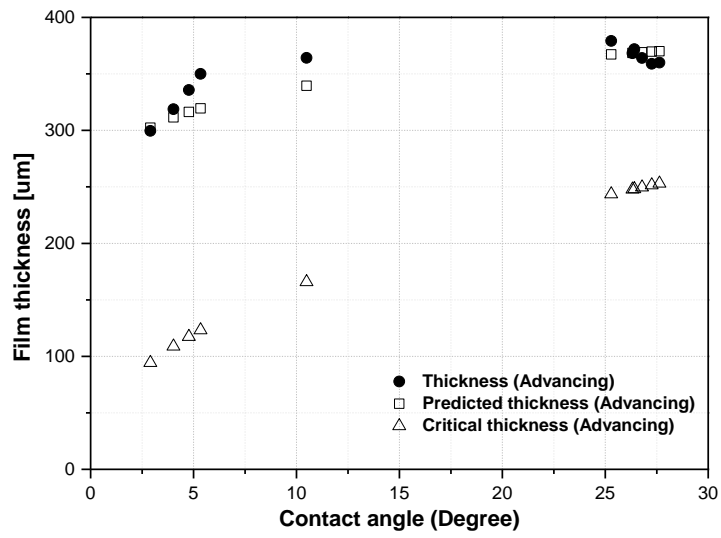
68

*Fig. 4-6 Thickness vs. contact angle (Increase flow rate, brass surface with a roughness of 1.6 μm)*
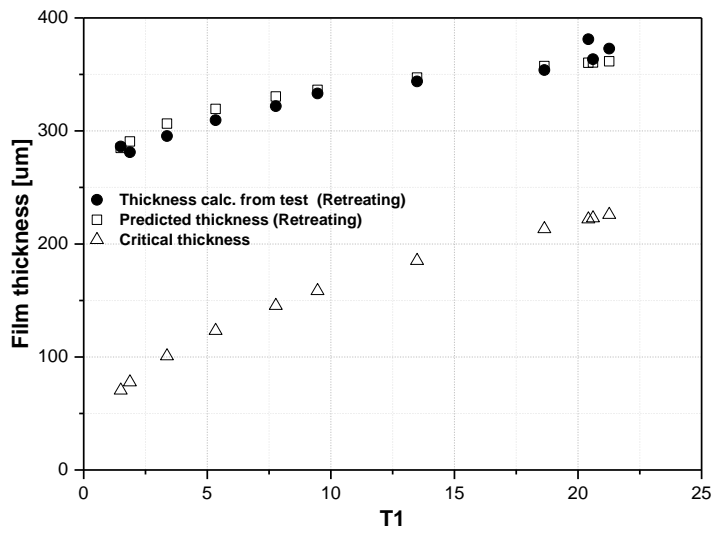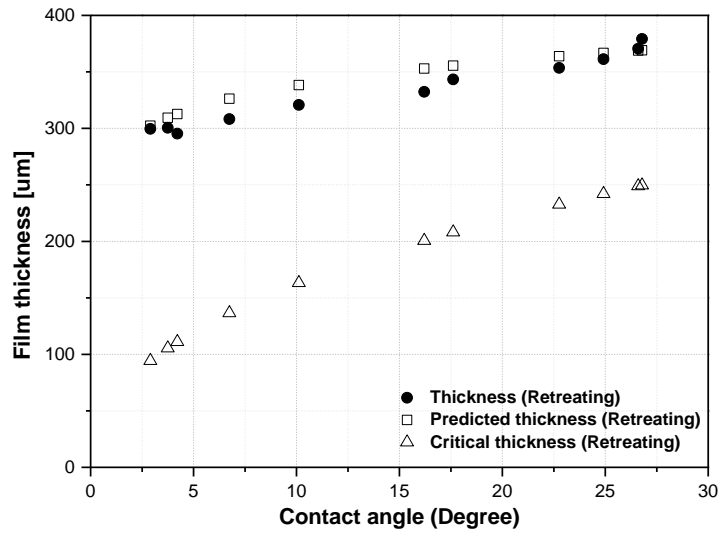


*Fig. 4-7 Thickness vs. contact angle (Reduce flow rate, aluminum surface with a roughness of 1.38 μm)*

*Fig. 4-8 Thickness vs. contact angle (Reduce flow rate, brass surface with a roughness of 1.6 μm)*

## 4.2 Assessment of the integrated film model

In order to verify the new liquid film model, a vertical steel plate connecting a rectangular channel is modelled with COCOSYS. In the test case, the width of the plate is $2\,m$ ; the height of the plate is $5\,m$ . Liquid flow is delivered from the top of the plate to form the liquid film, as illustrate in Fig. 4-9.
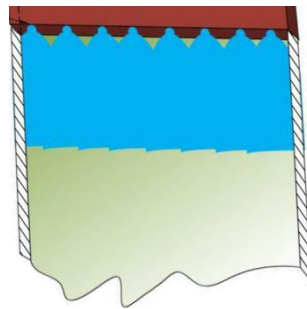


*Fig. 4-9 Schematic of the test case*

The delivered mass flow rate increases up to 0.9kg/s at first and then decreases to 0.04kg/s. Afterwards, the flow rate increases to 0.35kg/s and has been reduced again, as shown in Fig. 4-10. The purpose of varying the flow rate up and down is to capture the details of the development of liquid film and rivulets. In the test case, the advancing, equilibrium and retreating contact angles between rivulets and substrate are set to be 90 °, 70 °and 50 °, respectively, so as to demonstrate the constriction of rivulets and the

process of hysteresis.
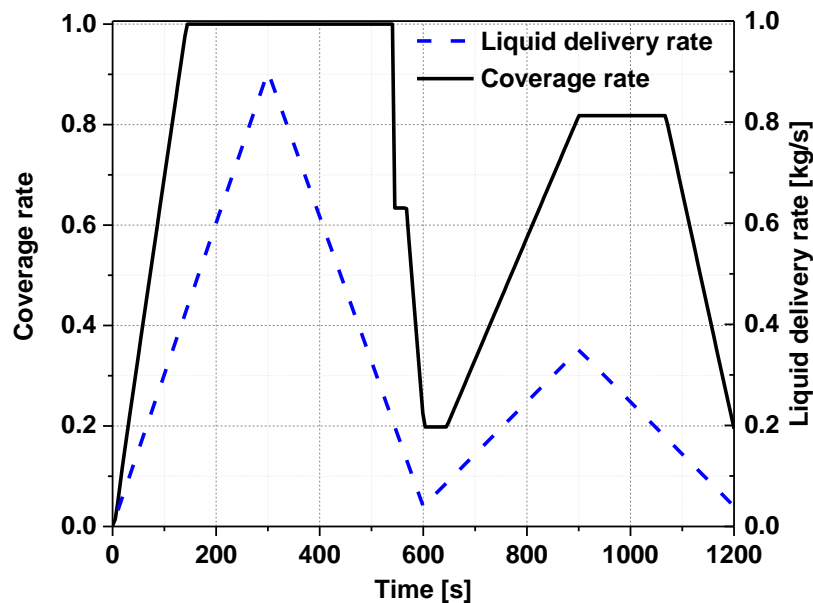


*Fig. 4-10 Delivered mass flow rate and coverage rate of the test case*

The new model has the possibility of providing film coverage rate on the structures. As shown in Fig. 4-10, when the liquid delivery rate increases, the coverage rate of the vertical plate has been gradually increased up to 1.0 and the rivulets are merged together to form the fully covered film.

On the contrary, when the liquid delivery rate decreases, the coverage rate doesn't change smoothly. As indicated in Fig. 4-10, when the film starts to break, the coverage rate decreases sharply to about 0.63 due to film breakup and the constriction of the newly formed rivulets. However, the coverage rate doesn't decrease further but shows a constant value for a short period after the breakup. This is attributed to the hysteresis of rivulets. When the fully covered film breaks up, the rivulets exhibit equilibrium contact angle and the contact lines do not change before the contact angle reduces to the retreating one. Thereafter, when the retreating threshold is reached as the liquid delivery rate keeps reducing, the coverage rate decreases smoothly.

At 600s, the mass flow rate starts to increase again as indicated in Fig. 4-10, the coverage rate doesn't increase immediately also because of the hysteresis, the contact angle of the rivulets increases from retreating value to advancing value in the meantime. After that, the coverage rate increases again but hasn't reach 1.0, since the liquid delivery rate is not large enough. As a result, no film breakup occurs and the coverage rate decreases smoothly after a short span of hysteresis.

Fig. 4-11 shows the change of contact angle and coverage rate over time. The relationship between contact angle and coverage rate is clearly demonstrated. The contact angle exhibits advancing or retreating values as the coverage rate is increasing or smoothly decreasing. When contact angle is changing, the coverage rate stays

71

invariable.

At about 540s, film starts to break up and the coverage decreases to about 0.63 due to the constriction of rivulets and the contact angle jumps to the equilibrium value of 70 °. Then the contact angle decreases further without the change of contact line or coverage rate until the rivulets start to retreat. During the retreating process, coverage rate decreases while the contact angle stays at the retreating value of 50 °. At about 600s, the contact angle starts to increase due to the increase in mass flow rate while the coverage rate is invariable due to hysteresis.
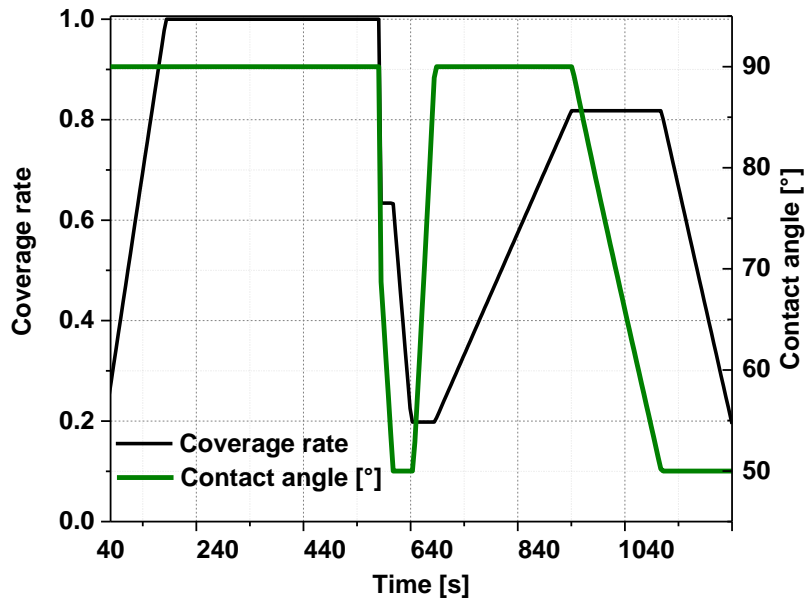


*Fig. 4-11 Change of contact angle and coverage rate over time*

Fig. 4-12 shows the change of film thickness and coverage rate. After the merging of the rivulets, fully covered film is formed and coverage rate reaches 1.0. Then film thickness increases or decreases as the mass flow rate varies. At about 540s, the fully covered film breaks up into rivulets and the film thickness increases abruptly due to the formation of rivulets with the equilibrium contact angle of 70 °. Afterwards, the rivulets do not merge again as the mass flow rate changes and the thickness ranges between the values calculated with advancing and retreating contact angles.
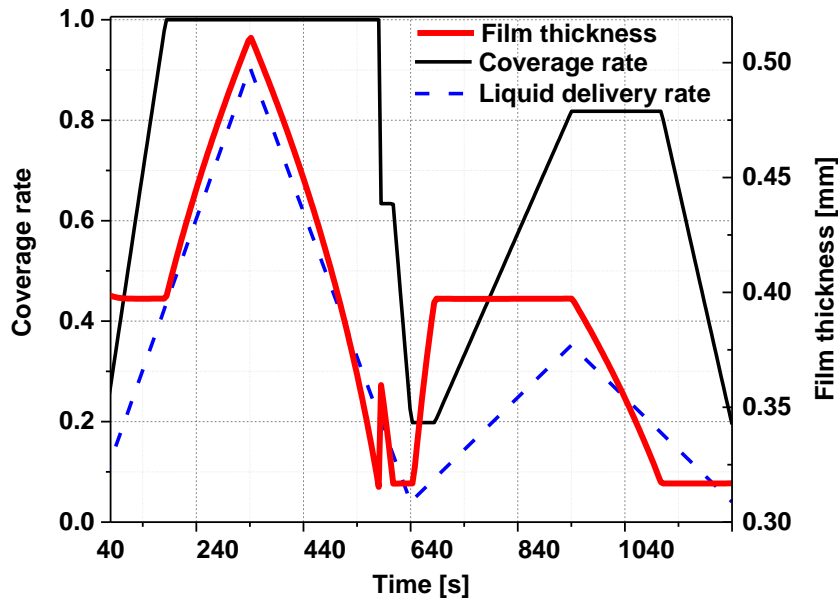
*Fig. 4-12 Change of film thickness and coverage rate over time*

The test case demonstrates the new capabilities of the new film model featuring the water film structure and the phenomenon of hysteresis. However, the falling film on the cool vertical plate of small scale does not reflect the development of fully covered film and rivulets along the hot substrate where evaporation is taking place. On the exterior surface of containment, the temperature could be relatively high during the accident scenario and this leads to a significant evaporation rate. Due to the long distance, the film/rivulet on the surface has to go through before it reaches the bottom of the containment or is completely evaporated, the film/rivulets may display in different forms along the wall at different elevations.

In order to exemplify this phenomenon, a test case applying PCCS film cooling on the AP1000 containment model is selected for assessment of the new model. The AP1000 containment is modeled as displayed in Fig. 4-13, where the geometry data are obtained from the literature which describes general features of AP1000 [77]. The simple nodalization of AP1000 containment based on MELCOR and CONTAIN [43] is taken as reference for the current nodalization strategy. The steel containment above the operating platform is divided into 5 layers. 5 structures of stainless steel are connecting the control volumes inside the containment and the control volumes in the PCCS annular channel, as displayed in Fig. 4-13.
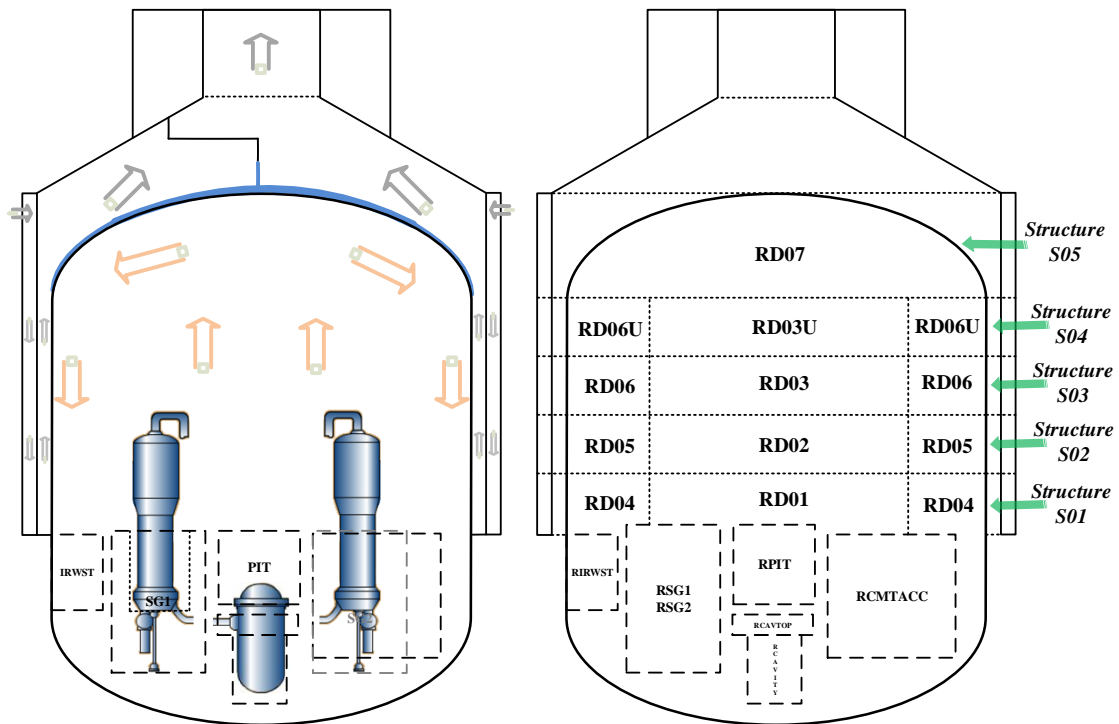
*Fig. 4-13 Simple nodalization of AP1000 passive containment [43]*

The liquid release rate in the steam generator compartment as well as the PCCS injection rate are prescribed arbitrarily, as shown in Fig. 4-14 and Fig. 4-15 (dotted line). The retreating, advancing and equilibrium contact angles are specified to be 60 ° and 90 ° and 75 ° respectively.
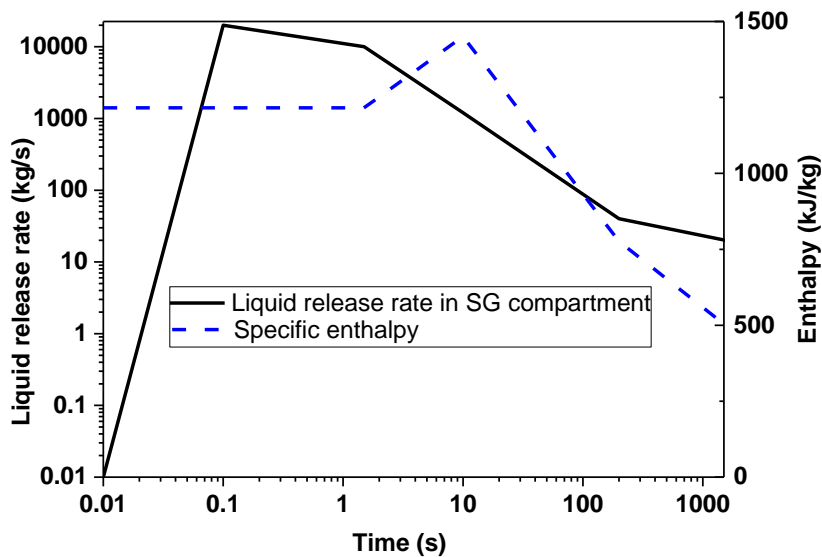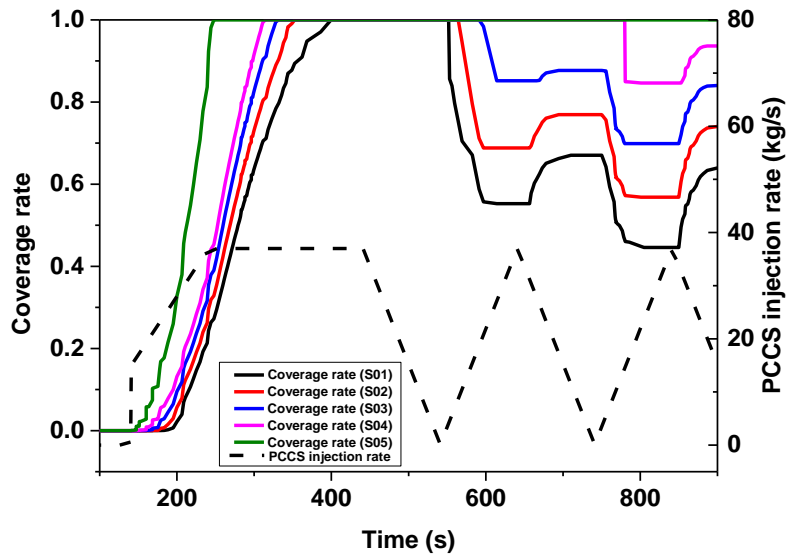


*Fig. 4-14 Liquid injection in SG compartment (Liquid mass flow and specific enthalpy)*

*Fig. 4-15 The PCCS injection rate and coverage rate at different elevations*

The coverage rates at different elevations, as indicated in Fig. 4-15, increases up to 1.0 as the PCCS injection rate increases to 37 kg/s at the beginning. At about 450s, the PCCS injection rate starts to decrease and reaches a very low value at around 550s and then begins to rebound. Afterwards the PCCS injection rate goes up and down periodically. In the meanwhile, after the breakup of film due to low flow rate, different coverage rates are presented at different elevations and the coverage rates at lower regions are always smaller since the falling film is being evaporated on the surface. It's worth noting that during each cycle of the flow rate change, there are plateau areas of the coverage rate, where the coverage rates are not sensitive to the flow rate change, and this is due to the rivulet hysteresis.
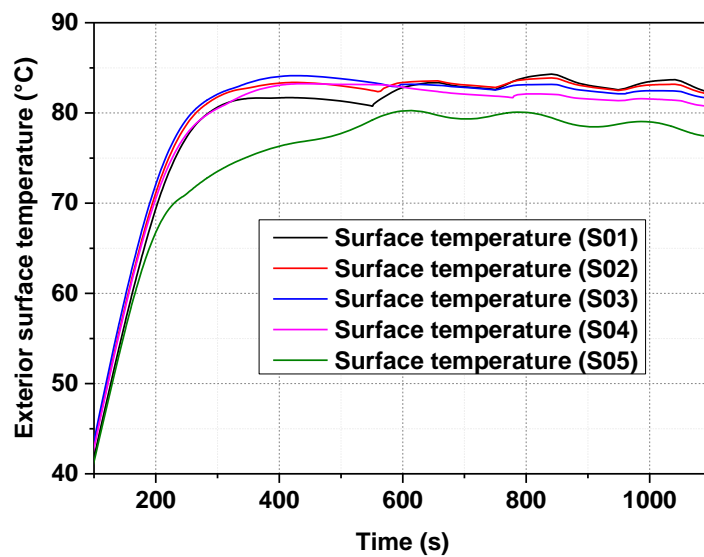


*Fig. 4-16 Containment exterior surface temperature*

75

Fig. 4-16 shows the temperature change at different elevations of containment exterior surface during the accident scenario. The surface temperature rises rapidly after the release of liquid inside the containment and then remains at more than about 83 ℃, which ensures the relatively high evaporation rate on the surface.
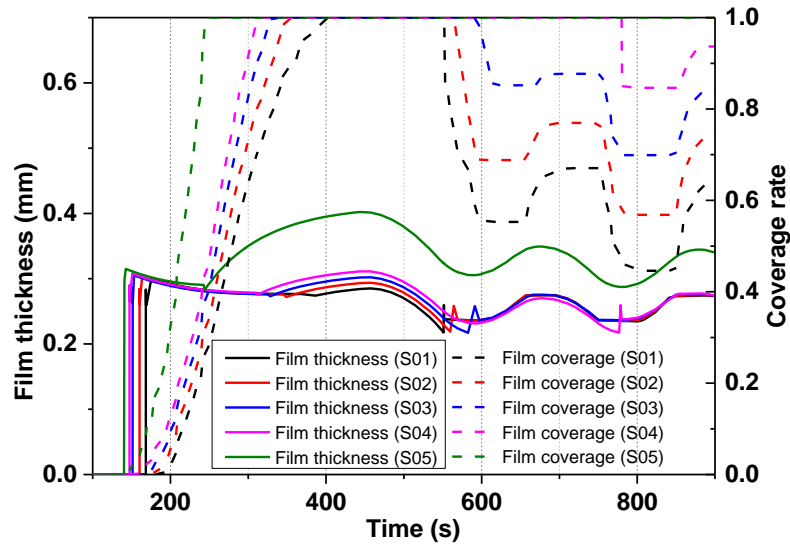


*Fig. 4-17 The film thickness and coverage rate at different elevations*



*Fig. 4-18 Film thickness and contact angle at different elevations*

Fig. 4-17 demonstrates the change of film thickness and the coverage rate at different elevations. After the injection of PCCS cooling water, the rivulet thickness rapidly increases to the value corresponding to the advancing contact angle. Then the rivulets keep advancing while the thickness decreases slightly due to the reduction of liquid

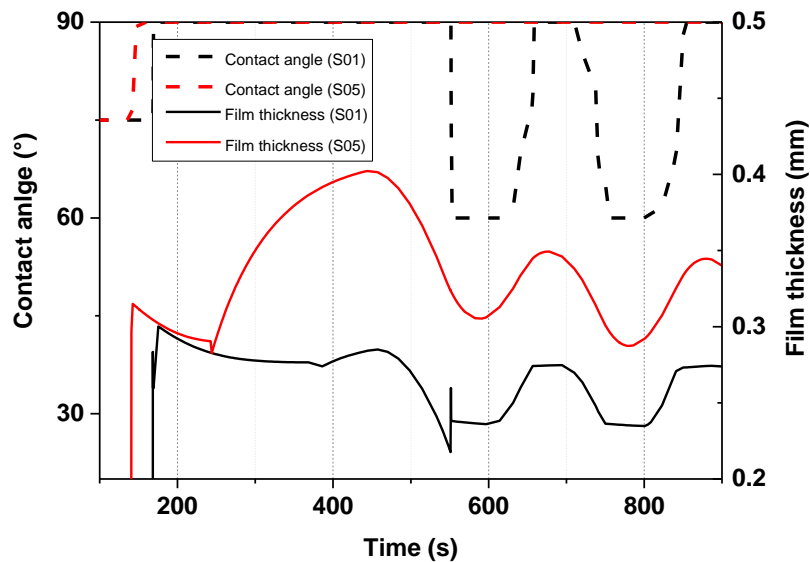viscosity resulted by the rise of surface temperature. Afterwards the film thickness begins to increase after the coverage rate reaches 1.0 or namely the merge of rivulets. Then the film thickness decreases as the PCCS injection rate is reduced. When the mass flow rate decreases to the critical value, the fully covered film breaks and rivulets with equilibrium contact angles are formed and at this moment a sharp increase of film thickness is exhibited. Thereafter, the rivulet thickness goes up and down as the injection rate varies.

Fig. 4-18 exhibits the change of film thicknesses at the upper and bottom regions and the corresponding contact angles. This figure indicates that when the cooling liquid is presented in the form of rivulets the film thickness varies in accordance with the change of contact angle. Additionally, it's observed in both Fig. 4-17 and Fig. 4-18 that the critical thickness of film breakup is significantly lower than the thickness of the rivulets to form the complete coverage. This fact indicates that in order to optimize the coverage, it might be better to employ a large PCCS injection rate at the beginning to ensure the fully coverage.

# 5  APPLICATION OF THE NEW MODEL

## 5.1  Application to PCCS of AP1000

Analyses evaluating the performance of PCCS of AP1000 PWR in case of accidents have been carried out by Sandia National Laboratories (SNL) [43]. In their work, the pressure load inside containment predicted with different codes and geometry models during the double ended cold leg LOCA accident with activation of PCCS have been studied. Moreover, Broxtermann et al. [3] used COCOSYS with original water film model in the code to simulate the same accident scenario. It's concluded that with the original water film model, COCOSYS can deliver results considering accident scenarios in AP1000 with evaporating water film on the exterior surface of containment.

### 5.1.1  Simple nodalization for AP1000 containment

In the current simulation, the nodalization of the AP1000 containment is in accordance with Fig. 4-13, where the geometry data are captured from Lin et al. [77] and the simple nodalization strategy has been taken from Tills et al. [43] as reference. An accident scenario regarding double ended cold-leg (DECL) LOCA accident, which is similar to Sandia National Laboratories (SNL)'s analysis [43] investigating AP1000 PCCS performance has been simulated. The data of mass and energy release are found in AP1000 Design Control Document [4]. Boundary conditions regarding PCCS water film flow rate are acquired from the report of SNL report [43], as shown in Fig. 5-1 and Fig. 5-2.
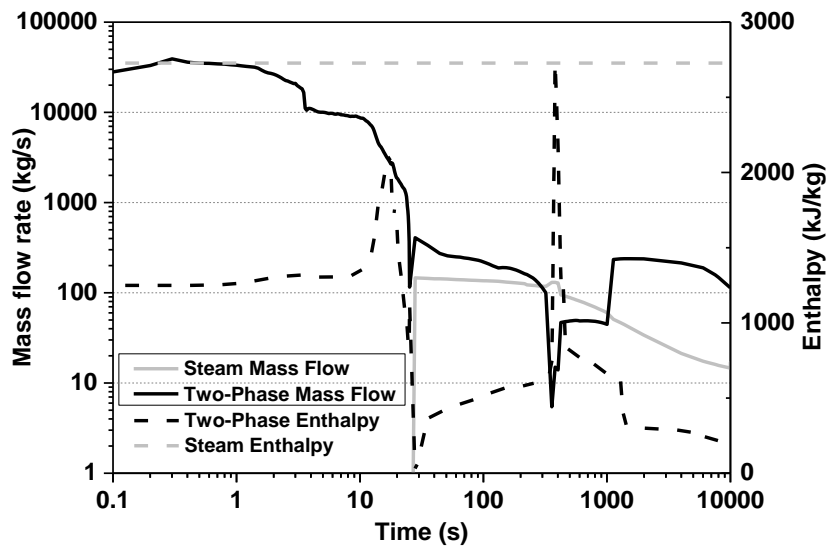
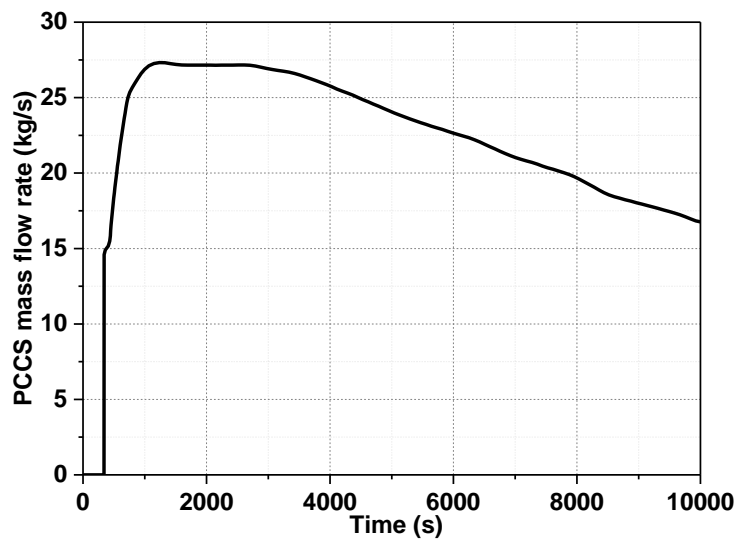*Fig. 5-1 Mass and energy release data for DECL break of AP1000 [43]*



*Fig. 5-2 Outer containment shell mass flow rate for PCCS [43]*

According to the study of Broxtermann et al. [3], the input deck used in COCOSYS for the conservative simulation (COCOSYS_Cons) is based on input data for WGOTHIC. Additionally, a different nodalization (COCOSYS_Plume) for simulating the AP1000 with COCOSYS has been built by Broxtermann et al. [3], in order to achieve more realistic results. It does not take into account the conservative assumptions and includes experience of modelling buoyant plumes above the steam generator compartments.

The pressure response inside containment during the accident scenario of Double-

Ended Cold Leg (DECL) LOCA is depicted in Fig. 5-3, where the red curve indicates the prediction with COCOSYS_Cons nodalization while the blue one denotes the result of COCOSYS_Plume nodalization. The black curve, which is between these two curves, describes the pressure variation calculated with original version of COCOSYS and with current nodalization. Similar trends are observed between these curves. The geometry data used for current input deck are captured from the references [4, 77]. This deviation of pressure responses could be resulted by the inevitable discrepancies of containment geometry as well as boundary conditions between the current case and others. Nevertheless, this input deck has already shown an acceptable deviation, thus confirms the availability of the containment nodalization.
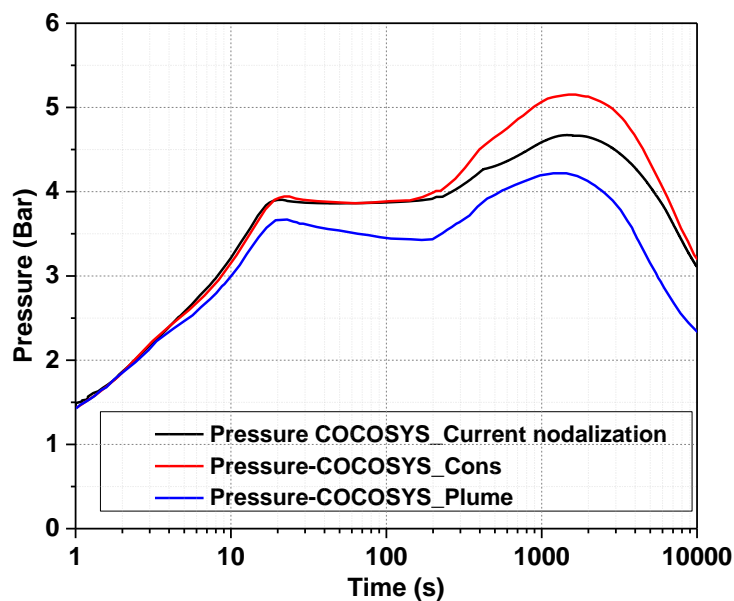


*Fig. 5-3 Containment pressure response to DECL break*

In order to study the influence of modified liquid film model, three different cases in terms of different sets of contact angles are performed. Table 5-1 shows the combinations of the contact angles of these cases.

**Table 5-1 Different sets of contact angles for different cases**

| Case number | Advancing contact angle | Retreating contact angle | Equilibrium contact angle |
|:---:|:---:|:---:|:---:|
| No. 1 | 90 ° | 90 ° | 90 ° |
| No. 2 | 30 ° | 30 ° | 30 ° |
| No. 3 | 90 ° | 30 ° | 60 ° |

Fig. 5-4 presents the comparison of pressure variation between the simulation result with COCOSYS with original water film model and with modified model. Compared

to the result of original film model, pressure loads predicted with modified model tend to be higher. The figure also reveals that the advancing contact angle of the rivulets is a decisive factor for the peak pressure, since a higher advancing contact angle results in higher peak pressure as indicated in case No. 1 and case No. 3, while the retreating contact angle is influential in the long term cooling as denoted by case No. 2 and case No. 3.
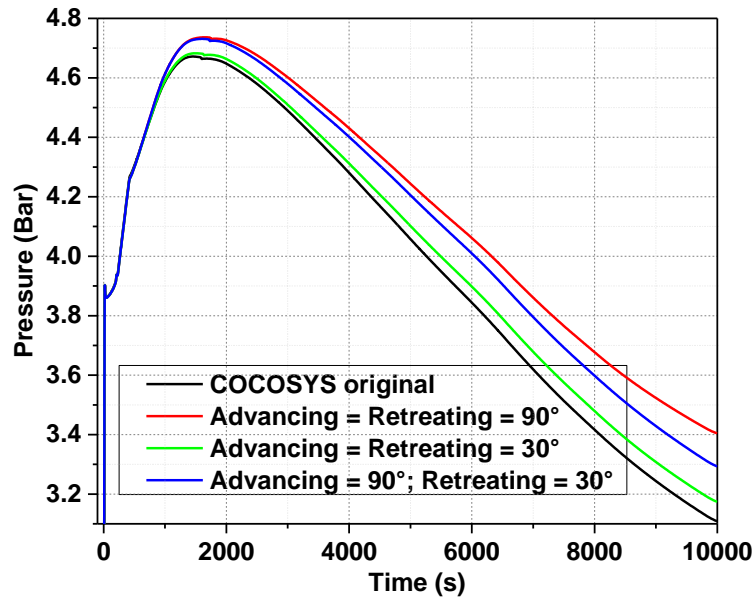


*Fig. 5-4 Pressure responses with different sets of contact angles*

Coverage rate of rivulets on different elevations is demonstrated in Fig. 5-5 and Fig. 5-6. The locations of the structures S01 to S05 are presented in Fig. 4-13. In Fig. 5-5, the coverage rate of case No. 1 and case No. 3 is presented and for case No. 3, since the advancing contact angle is significantly larger than retreating one, the phenomenon of hysteresis can be clearly observed. As shown by the full curves, soon after the blowdown, the coverage rates at different elevations increase rapidly. Then the coverage rates keep unchanged during the long term cooling, even though the PCCS injection rate is gradually decreasing in the meantime. This is in accordance with the phenomenon observed in the experiment [59] that during the long term cooling, the contact lines between the rivulet and substrate are stagnated while the contact angle is ranging between advancing and retreating values. During the blowdown phase of case No. 1, the change of coverage rate is in accordance with that of case No. 3. However, the coverage rates at different elevations varies as the PCCS injection rate and evaporation rate on the surface are changing.

These discrepancies of coverage rate between cases result in the discrepancies of pressure change. The peak pressure of case No. 3 is close to case No. 1 since the advancing contact angle of these two cases are the same and during the blowdown phase the rivulets are advancing due to the rapid increase of PCCS injection rate. This results in the same coverage rates between these two cases at the beginning of the simulation.

During long term cooling, the coverage rates of case No. 3 are generally larger than those of case No. 1, therefore the overall evaporation rate of case No. 3 is larger and the pressure is slightly lower than that of case No. 1 in the latter period, as shown in Fig. 5-4.
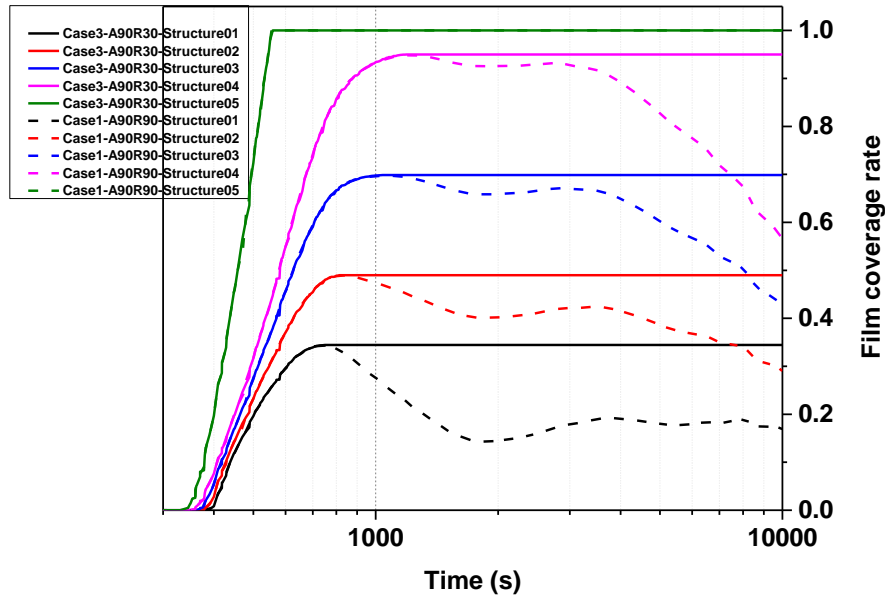


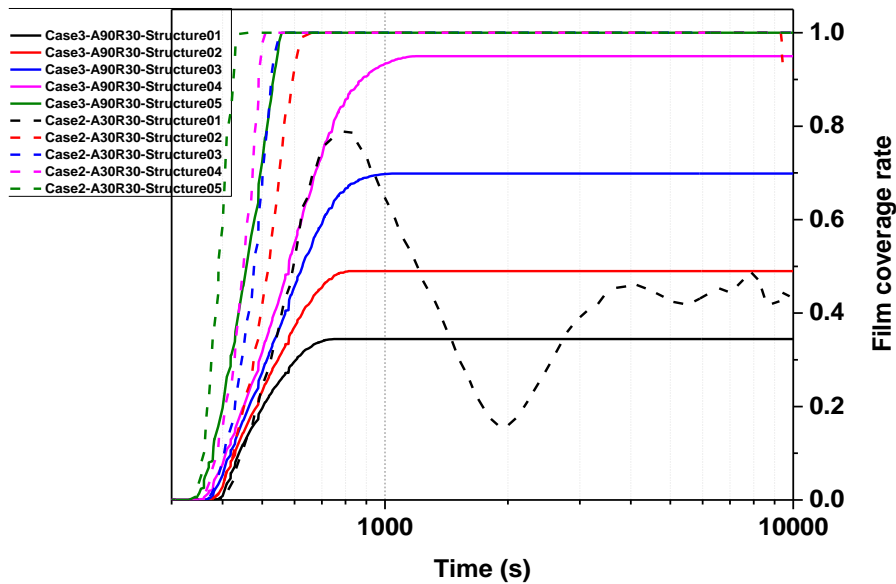*Fig. 5-5 Film coverage rates of case No. 1 and case No. 3 at different elevations*



*Fig. 5-6 Film coverage rates of case No. 2 and case No. 3 at different elevations*

Similarly, Fig. 5-6 implies the reason of smaller peak pressure of case No. 2. During the blowdown phase, the coverage rate of case No. 2 increases faster than that of case

82

No. 1 or case No. 2 due to the smaller advancing contact angle, this results in a better film coverage and a larger evaporation rate, especially at the upper part of the containment where the fully coverage is reached. In the long term cooling the fully coverage at the upper part of the containment is kept and thus ensures better cooling effectiveness compared to other two cases.
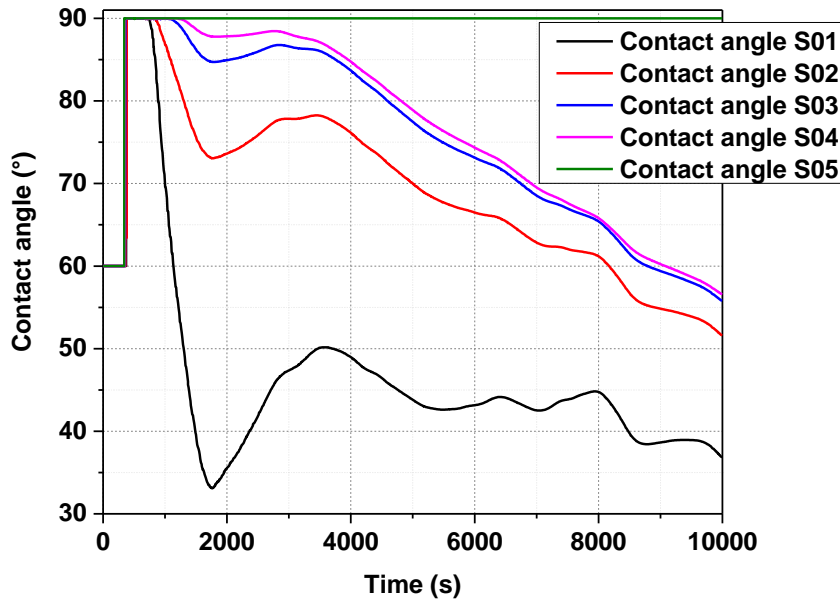


*Fig. 5-7 Change of contact angles at different elevations of case No. 3*

Fig. 5-7 presents the change of contact angles of case No. 3 at different elevations of the containment. At the beginning of PCCS injection, all rivulets are advancing and the contact angle reaches the maximum. When the PCCS injection rate starts to decrease slowly, the rivulets are undergoing the hysteresis and the contact angles decreases and varies according to the change of flow rate and the evaporation rate. It's noteworthy that at the upper part of the containment, the contact angle, as indicated with the green curve in the figure, keeps as the advancing value. This is due to the fully coverage of the rivulets at the upper part of the containment and the breakup doesn't take place in the long term cooling.
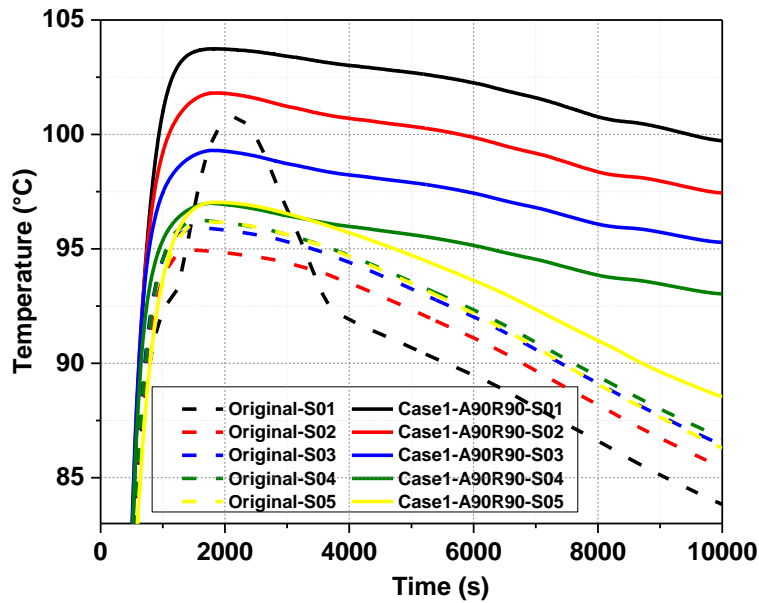
*Fig. 5-8 Change of structure exterior surface temperature at different elevations*

Fig. 5-8 demonstrates the change of containment exterior surface temperature at different elevations. The dash curves indicate the surface temperature calculated with original film model while the full curves represent the surface temperature of case No. 1. Due to the absence of rivulets model in the original film model, the surface is considered to be fully covered before it is completely evaporated and its cooling effect is exaggerated. As shown in the figure, the exterior surface temperature of steel structure predicted with the modified model is generally higher than the results calculated with the original model. This difference results in a discrepancy of internal surface temperature and therefore the discrepancy of pressure response.

As Gaetano Aiello et al. pointed out [18], the contact angle for water steel contact ranges between 70° and 90° according to some experimental results, which is close to the set of contact angle of case No. 1. Therefore, the original film model overestimates the cooling effect of film and under-evaluates the pressure response inside containment during the accident scenario.

### 5.1.2　Refined nodalization for AP1000

In order to achieve more realistic results and to present more detailed thermal-hydraulic phenomena, as well as to study the sensitivity of nodalization strategies, a refined nodalization has been established as shown in Fig. 5-9.
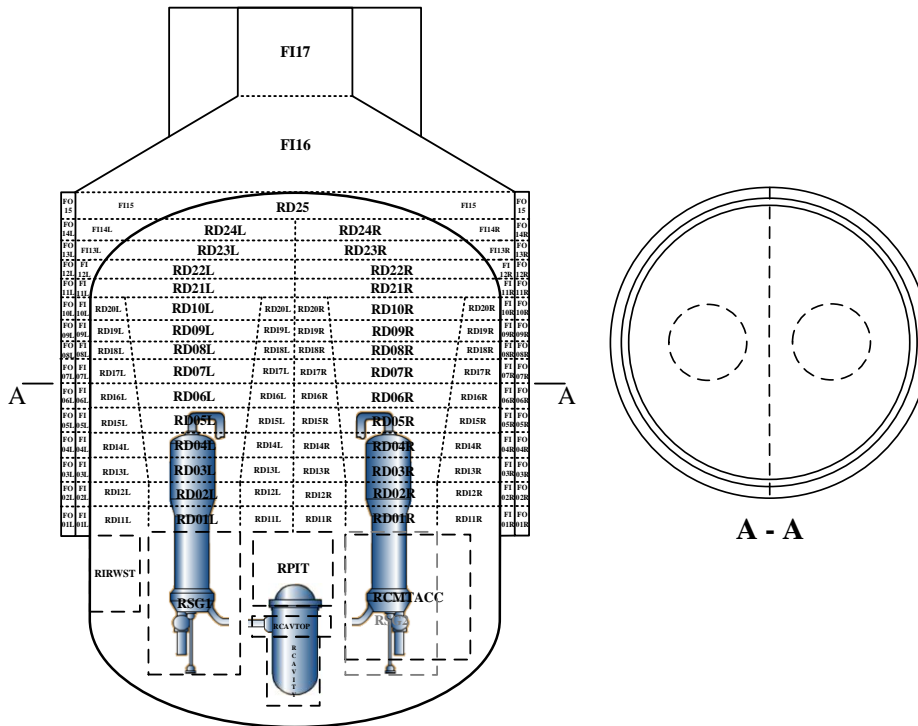
*Fig. 5-9 Refined nodalization of AP1000 passive containment*

In the refined nodalization, buoyant plumes above the steam generator compartments are modeled according to the experiences of other studies [3]. As shown in Fig. 5-9, the top view of the cross section indicates that the containment including the PCCS flow channels are divided into left side and right side. The LOCA takes place in the left SG compartment and therefore some asymmetrical phenomena can be expected. In the refined nodalization, the upper dome of the containment is outlined with several inclined structures while the height and the volume of containment upper dome are kept in line with the simple nodalization, as depicted in Fig. 5-10.
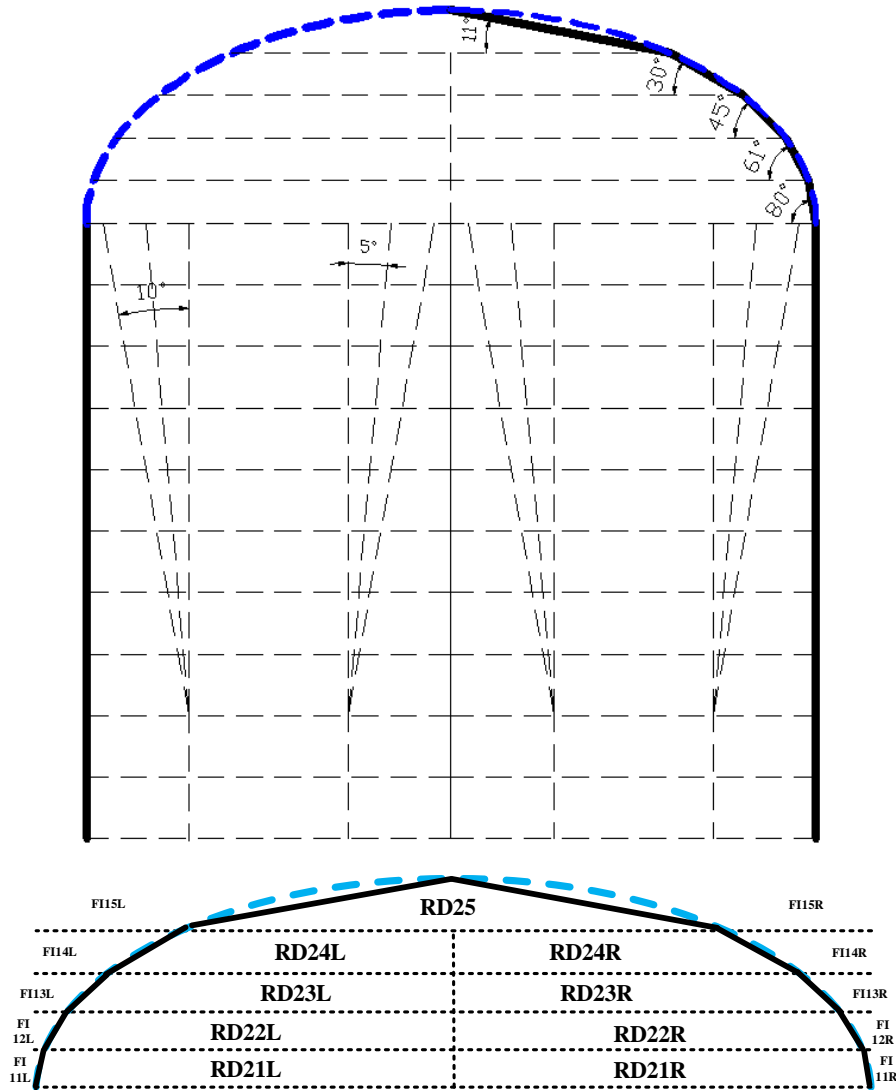
*Fig. 5-10 Plume nodalization and the outline of the upper dome structure*

Fig. 5-11 shows the pressure responses with simple and refined nodalizations, which are calculated with the original film model. 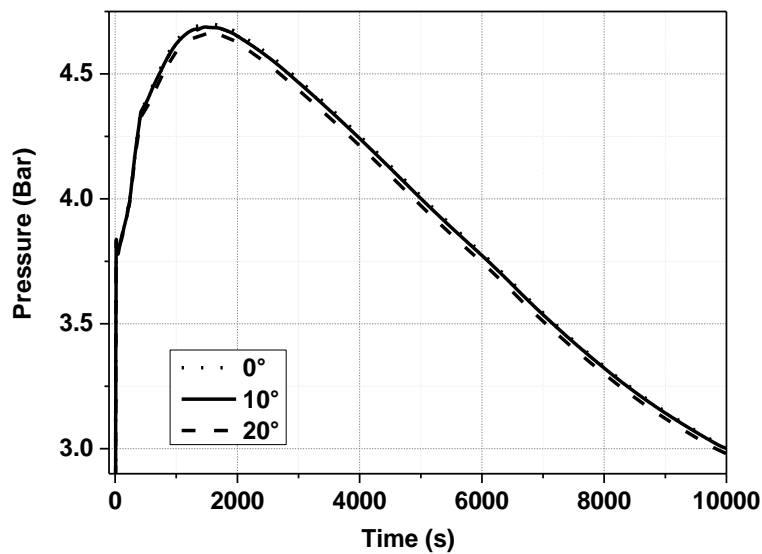With the refined nodalization, the pressure during the long term cooling is slightly smaller than the prediction of the simple nodalization. In order to evaluate the influence of plume nodalization, a sensitivity analysis has been conducted. According to the experience of other studies, the plume nodalization forms an upside cone with an angle of about 20 °[65]. Therefore, the angle of the cone ranges from 0 °to 20 °in the sensitivity analysis. The pressure variations of these simulations are presented in Fig. 5-12. The results indicate that the pressure response tends to be slightly lower as the angle of cone increases. However, the difference is not obvious and therefore the angle of the plume is unlikely to be the main reason of the reduction of pressure compared to the result of simple nodalization.
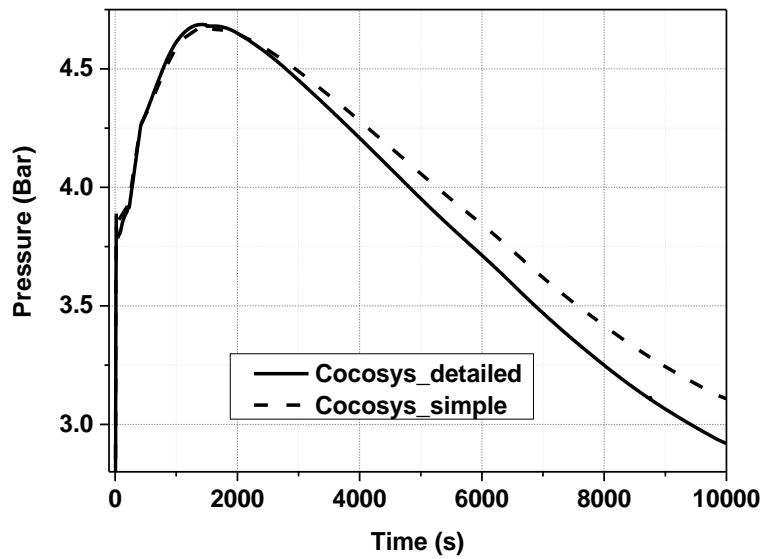
*Fig. 5-11 Pressure responses calculated with original film model with simple and refined nodalization*



*Fig. 5-12 Pressure responses calculated with different angles of plume nodalization*

Similar to the simple nodalization, simulations using different sets of contact angles have been conducted as well based on the refined nodalization and the pressure variation is presented in Fig. 5-13. For the pressure variation, a similar phenomenon has been observed as Fig. 5-4 indicates. Based on the refined nodalization, similar to the results of simple nodalization, it is revealed that the original film model in COCOSY tends to under estimate the peak pressure as well as the pressure variation during the long term cooling. Moreover, the advancing contact angle is decisive for the peak

pressure while the retreating contact angle influences the long term cooling to a certain degree.
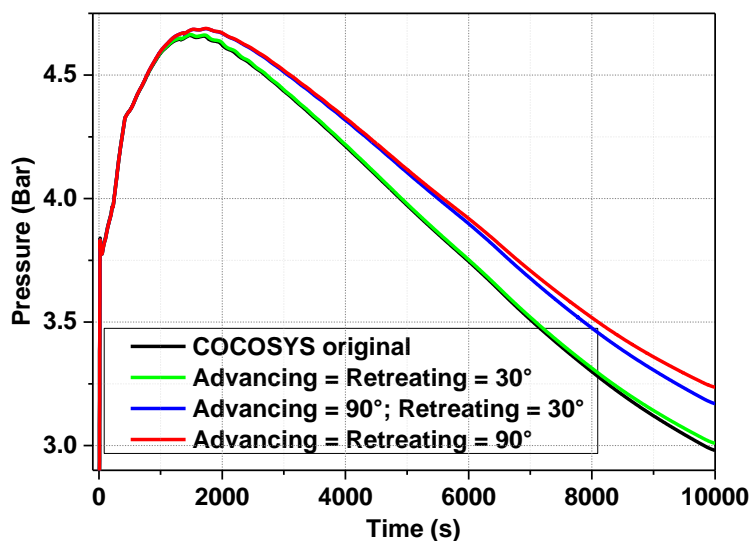


*Fig. 5-13 Pressure responses with different sets of contact angles with refined nodalization*

Fig. 5-14 to Fig. 5-17 have presented the change of coverage rate and contact angle on both left and right side of the containment exterior surface. Three different cases in accordance with Table 5-1 are calculated. The changes of coverage rates are quite similar to the results of simple nodalization. With the refined nodalization, since at LOCA the coolant is discharged in the left steam generator compartment, slight differences of the coverage rate and contact angle between left and right side of the containment exterior surface can be observed, i.e., the coverage rate on the left side of the surface is generally slightly smaller than that on the right side, especially on the lower part of the containment.
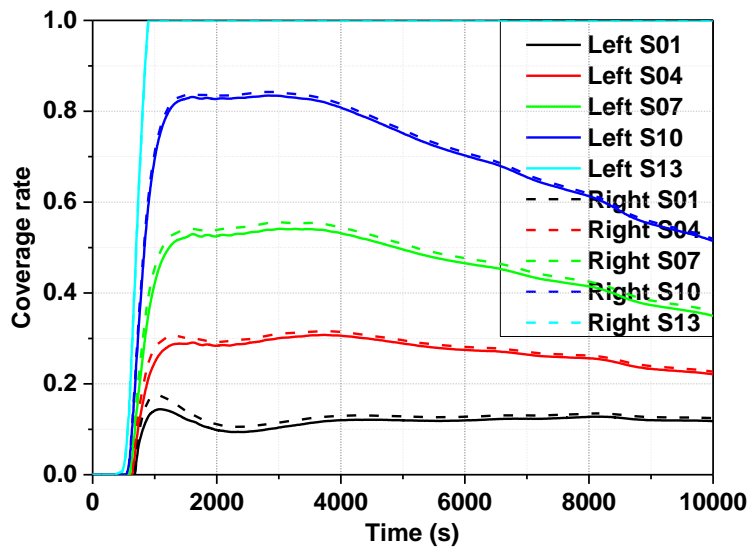
*Fig. 5-14 Film coverage rates of case No. 1 at different elevations and different sides (Advancing contact angle = retreating contact angle = 90 ゜)*



*Fig. 5-15 Film coverage rates of case No. 2 at different elevations and different sides (Advancing contact angle = 90 ゜; retreating contact angle = 30 ゜)*

89

*Fig. 5-16 Film coverage rates of case No. 3 at different elevations and different sides (Advancing contact angle = retreating contact angle = 30 °)*



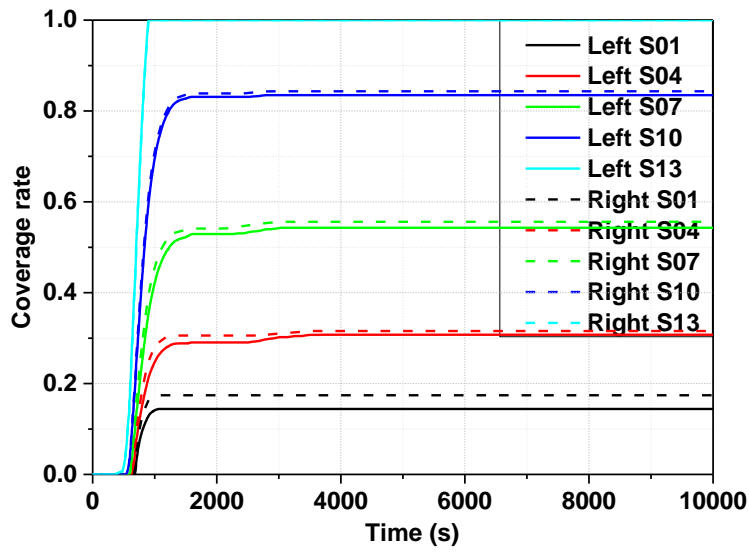*Fig. 5-17 Rivulets contact angle of case No. 2 at different elevations and different sides (Advancing contact angle = 90 °; retreating contact angle = 30 °)*

### 5.1.3   Simulation with 'Jet zones'
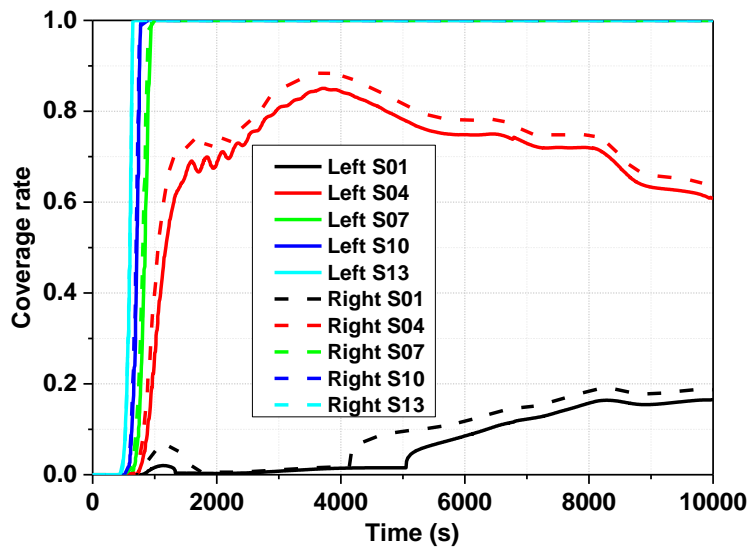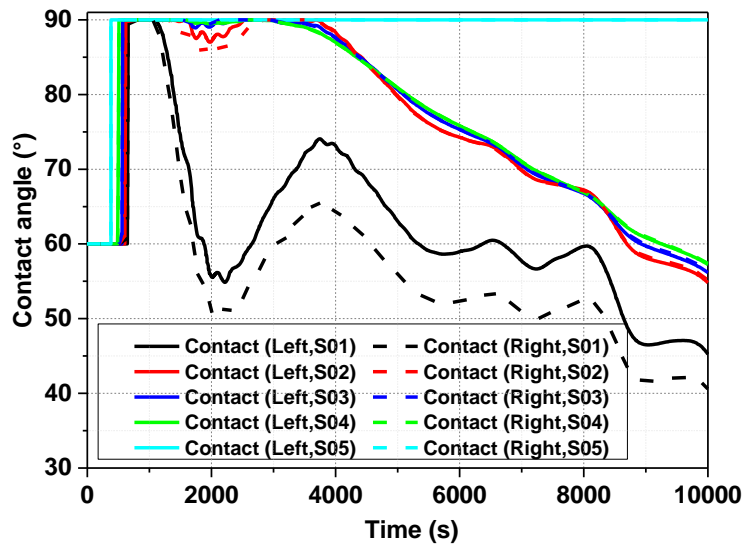
According to the experiences of other studies [65, 78, 79], for simulations of gas/liquid release, it is recommended to use so called 'Jet zones' in addition to the plume nodalization which has been presented in previous section.

In order to establish a set of 'Jet zones', two special zones should be defined above the injection point. One inner zone, which is cylindrical and is surrounded by one outer zone. These two zones together form an upside cone with a specific angle. The inner zone has only one junction at the top while the outer zone has one junction at its top and another at the side. Injected mass flow is divided equally between both zones. The scheme of the "Jet zones" are demonstrated in Fig. 5-18.
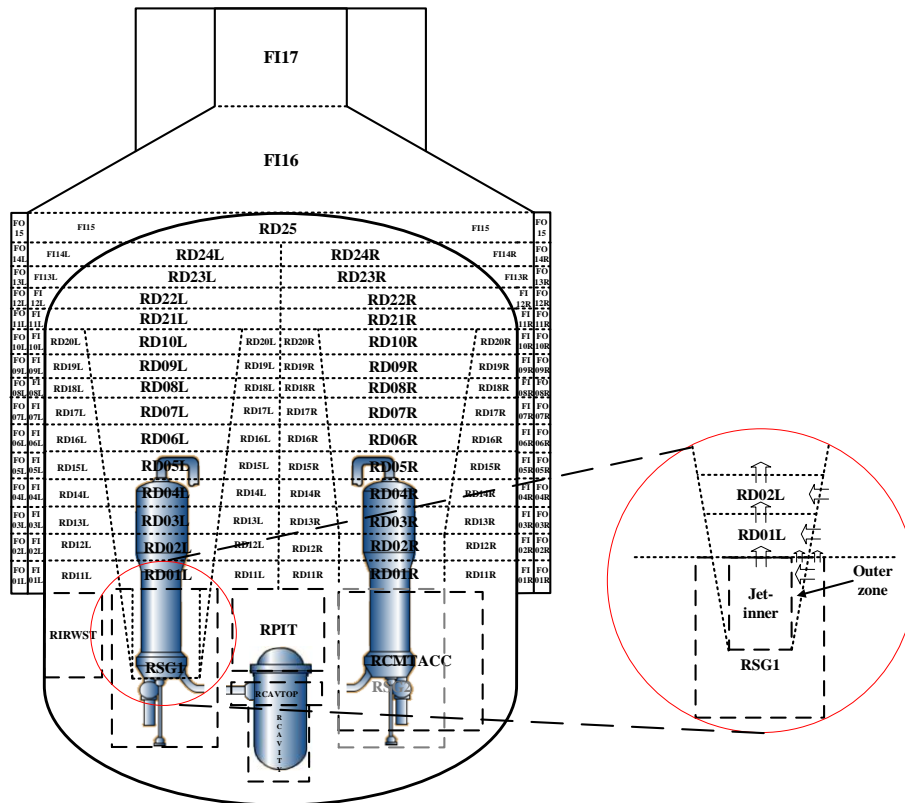


*Fig. 5-18 Rivulets nodalization scheme of 'Jet zones' in addition to plume zones*

In Fig. 5-19, pressure responses calculated with different nodalizations and different film models are presented. The solid curves in the figure indicates the results with modified models while the dash curves are the results calculated with original film model in COCOSYS. It can be observed that the pressure responses calculated with 'Jet zones' in addition to refined nodalization are lower than the results without 'Jet zones'. Accordingly it can be concluded from these curves that both refinement of nodalization and the employment of 'Jet zones' tend to lower the pressure response, especially during the long term cooling.
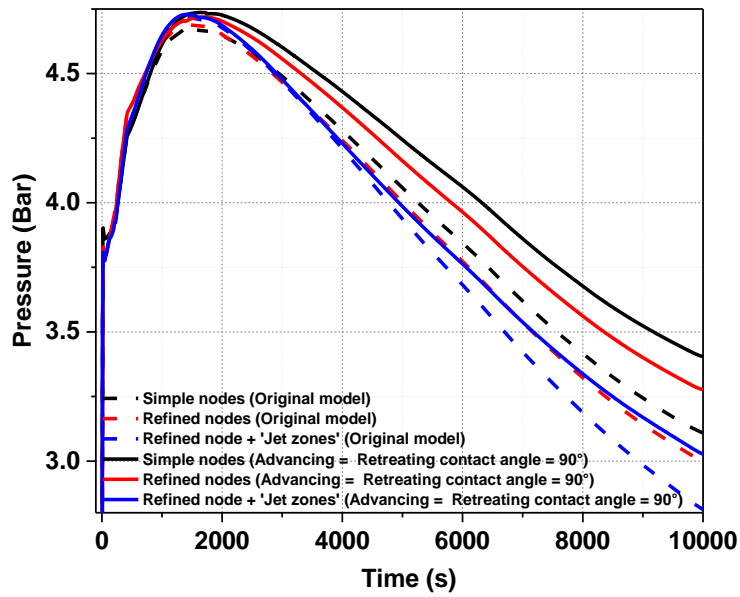
91

*Fig. 5-19 Pressure responses calculated with different nodalizations and different film models*

The influence of the angle of 'Jet zones' and plume nodes can be observed from Fig. 5-20. These results are all calculated with original film model, the only difference is the angle of 'Jet zones' and plume nodes, similar to Fig. 5-12. As a result, it can be concluded that the pressure response is not sensitive to either the angle of 'Jet zones' or the angle of plume nodes.
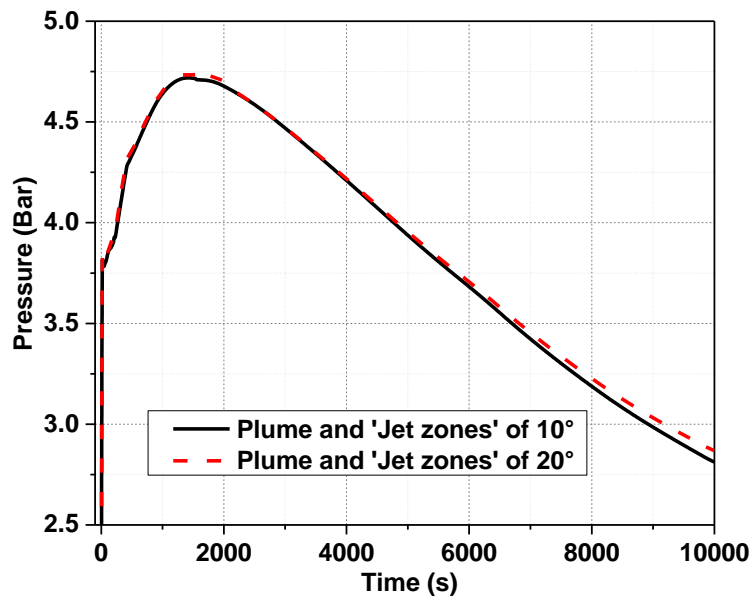


*Fig. 5-20 Predictions of pressure with different angles of plume nodes and 'Jet zones'*

Similar to Fig. 5-4 and Fig. 5-13 in the last section, pressure responses with different

sets of contact angles with refined nodalization and 'Jet zones' are shown in Fig. 5-21. Even though during the long term cooling, the influence of contact angle is similar to the results without 'Jet zones', the peak pressures predicted with the current nodalization doesn't present much difference.
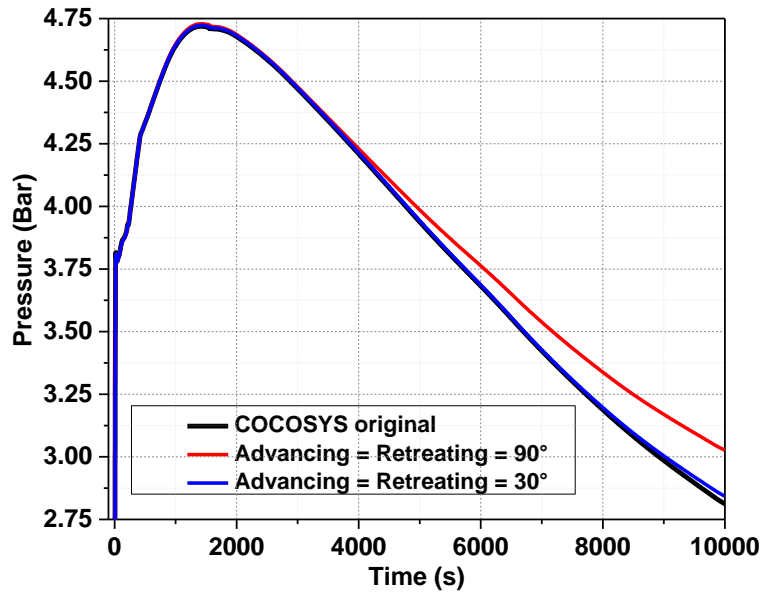


*Fig. 5-21 Pressure responses with different sets of contact angles with refined nodalization and 'Jet zones'*

In order to find out the reason, the film evaporation rate on the entire exterior surface of steel containment is presented in Fig. 5-22. During the first 2800s of the simulation, the total film evaporation rates calculated with original film model and the modified one are almost the same. This implies that during this period, the amounts of heat removed due to film evaporation is almost the same in both cases. Therefore, the peak pressures are very close to each other. During the long term cooling, the evaporation rate calculated with the modified model is lower and thus leads to the higher pressure response during the long term cooling.
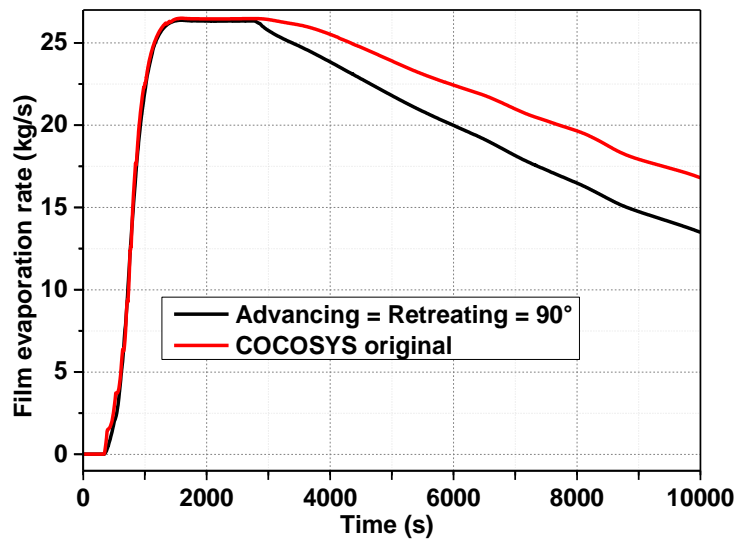
*Fig. 5-22 Film evaporation rate on entire exterior surface of steel containment*

## 5.1.4 Optimization of PCCS injection rate

The study of previous sections reveal that, the surface temperature of containment increases rapidly during the blow down phase of the LOCA accident and the PCCS film coverage rate is small at the lower part of the containment. Additionally, the peak pressures are reached within the first 2000s for all simulations. After that, the containment pressure decreases gradually during the long term cooling.

Assuming that the total amount of PCCS cooling water used in the simulation of 10000s period is a constant, four different cases with different PCCS injection rate, i.e. flow rate adjusted over time, have been calculated. The mass flow rate and the integrated mass of these four cases are shown in Fig. 5-23 and Fig. 5-24. The injection rate 01 indicates the PCCS injection rate used in previous sections as shown in Fig. 5-2. The other 3 cases have the peak injection rate in the blow down phase increased by about 5kg/s, 10kg/s and 15kg/s, respectively while the integrated mass flow at 10000s is a constant as indicated in Fig. 5-24.
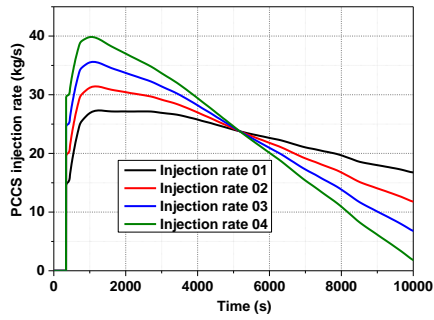
**Fig. 5-23 Different PCCS injection rate**     **Fig. 5-24 Different integrated PCCS mass flow**
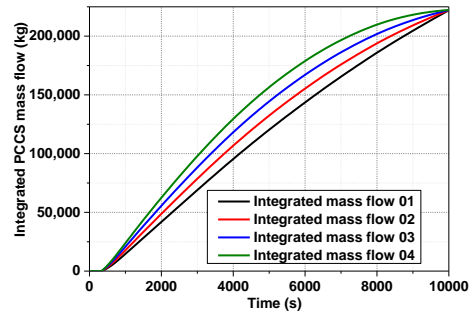
The pressure variations with these different PCCS injection rates are presented in Fig. 5-25. The advancing and retreating contact angles are both specified as 90 °. These curves denote that the peak pressure in the containment can be reduced by increasing the injection rate during the blow down phase.
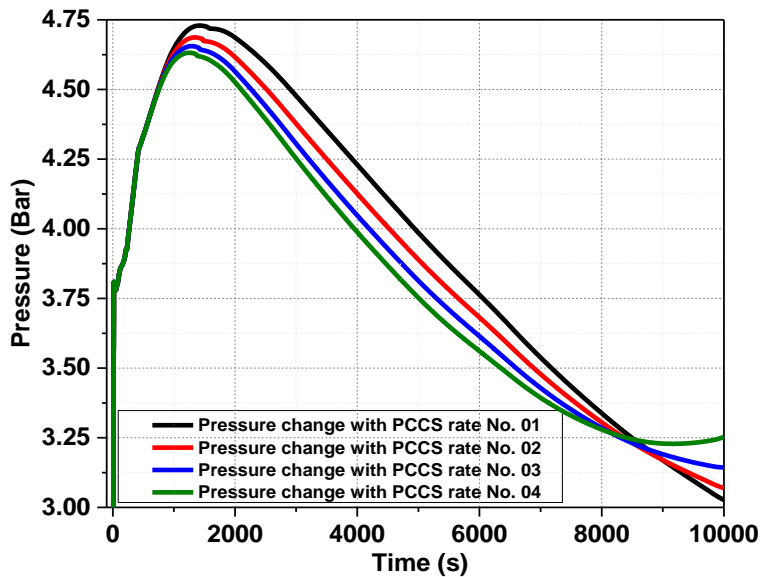


**Fig. 5-25 Pressure variations with different PCCS injection rate (Advancing = retreating contact angle = 90 °)**

The change of coverage rate at the bottom of steel surface and total evaporation rate calculated with different PCCS injection rates during the first 3000s are shown in Fig. 5-26 and Fig. 5-27. In these simulations, the advancing and retreating contact angles are both specified as 90 °. These curves indicate that, the coverage rate at the lower part of steel surface as well as the total evaporation rate on the surface are increased by increasing the injection rate during the blow down phase, and this leads to the reduction of the peak pressure.

95
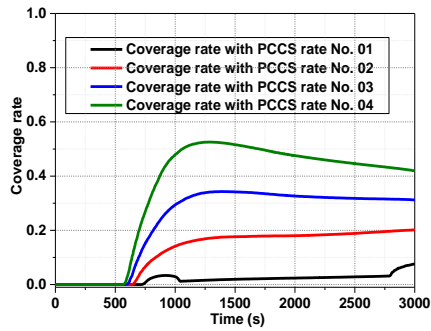
*Fig. 5-26 Coverage rate at the bottom of exterior surface with different PCCS injection rate (Advancing = retreating contact angle = 90 ⁹)*
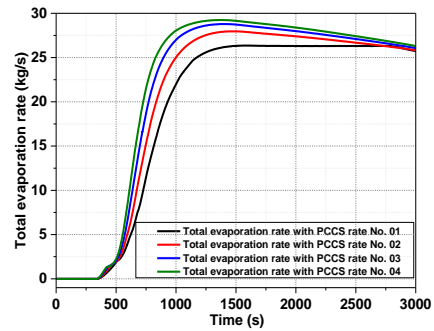


*Fig. 5-27 Total evaporation rate on the exterior surface with different PCCS injection rate (Advancing = retreating contact angle = 90 ⁹)*

Fig. 5-28 demonstrates the pressure response with the PCCS injection rate No. 3 as indicated in Fig. 5-23. Pressure responses simulated with modified water film model are presented to compare with the results calculated with original model. In this case, the peak pressure calculated with the advancing contact angle of 90 ° is slightly larger than the results with original film model. With the smaller retreating contact angle as indicated by the green curve, the pressure decreases more rapidly during the long term cooling. This is due to the lower rivulet thickness during the retreating process with the smaller contact angle which results in a larger coverage rate.
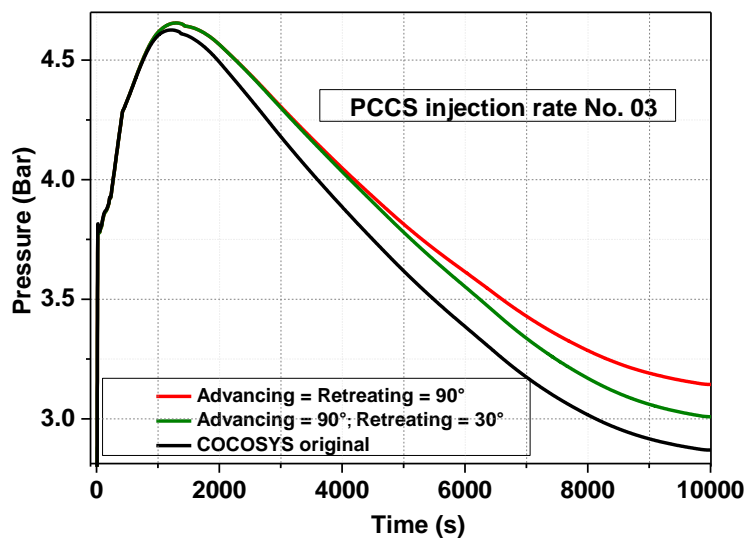


*Fig. 5-28 Pressure responses calculated with original film model and modified model with different sets of contact angles*

96

Fig. 5-29 displays the temperature changes at different elevations of the containment and with different PCCS injection rates. It can be observed in the figure that the surface temperatures are reduced significantly by increasing the PCCS flow rate at the blowdown phase, as indicated in dash curves. In the latter period, in order to maintain the constant integrated PCCS injection, the film flow rate is reduced as shown in Fig. 5-23. During this period, the surface temperatures are increased and finally higher than the surface temperatures calculated with standard PCCS injection rate.
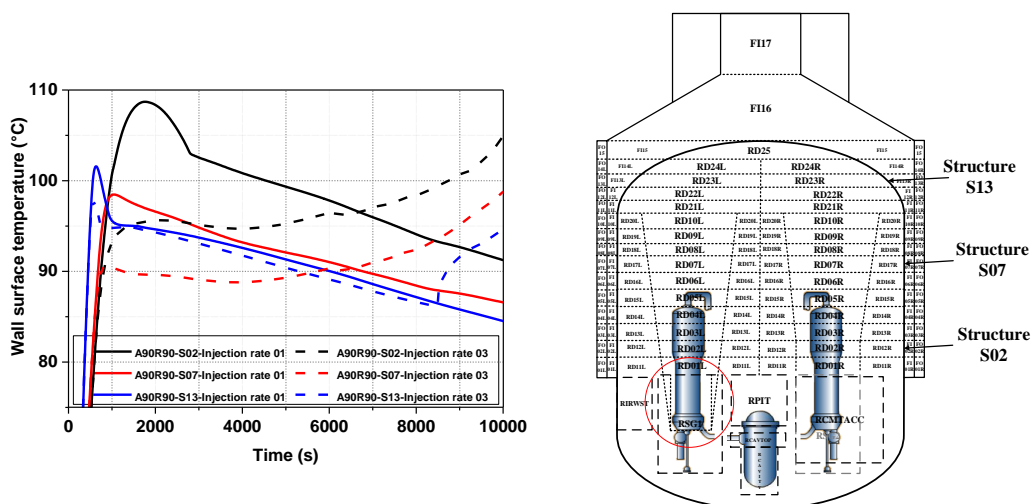


*Fig. 5-29 The temperature changes at different elevations of the containment and with different PCCS injection rate*

## 5.2   Application for generic containment

The modified water film model has also been applied to the Generic Containment, which was proposed in the frame of the European Network of Excellence SARNET2 (Severe Accident Research Network) to compare and to assess different lumped parameter (LP) codes and models [80]. Fig. 5-30 presents the Generic Containment nodalization, based on which the simulation has been carried out, i.e., the in vessel phase of a LOCA accident. As shown in the figure, the upper dome of containment has been refined in order to observe the detailed phenomena of water film and the structure between then containment and the U-dome is replaced with steel.
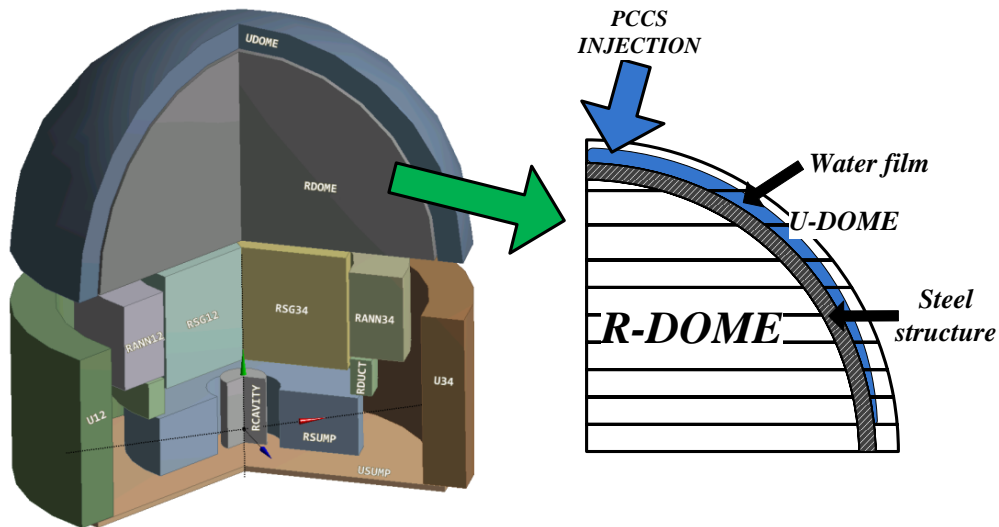
*Fig. 5-30 Refinement of the Generic containment geometry [80]*

PCCS water film injection has been implemented for the test case and the water injection rate is shown in Fig. 5-31. Fig. 5-32 presents the pressure response after implementation of water film cooling. Results predicted with the new water film model of different contact angles have been compared with the prediction of original film model. As indicated in this figure, the pressure load has been significantly reduced by means of film cooling. Moreover, by increasing the contact angle, similarly as the results of previous sections, the peak pressure tends to increase. This implies that the original film model also overestimates film cooling efficiency when the contact angle is large, e.g. the water film covers a hydrophobic surface. Whereas, when the contact angle is small, e.g. when the water film is presented on a hydrophilic surface, due to the better wettability and the resultant larger coverage rate, the discrepancy between the results of original film model and the new model is small.
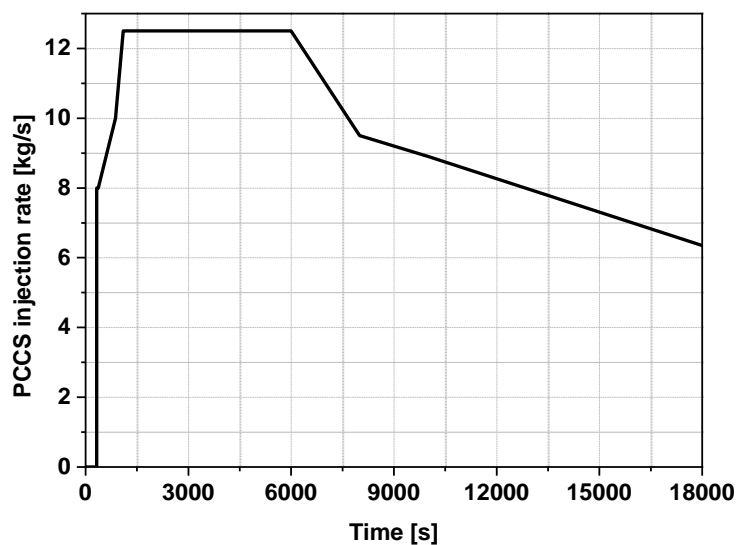


*Fig. 5-31 PCCS injection rate for Generic Containment*

98
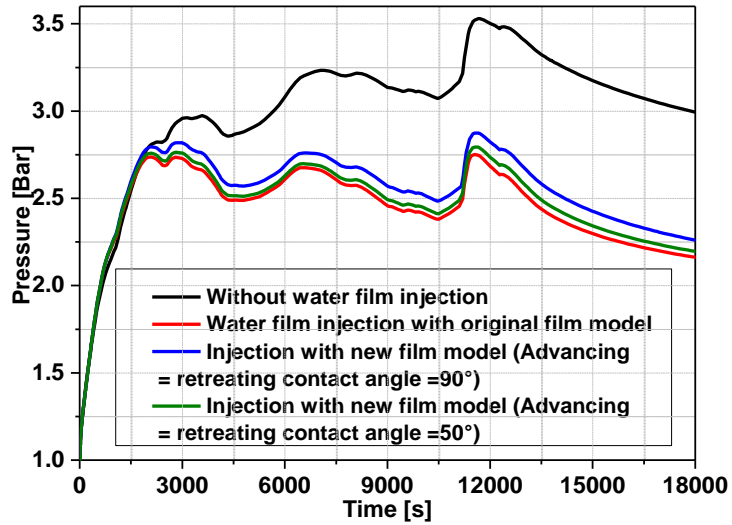
*Fig. 5-32 Pressure response predicted with different film models and contact angles*

With the results presented in this chapter, it can be concluded that the pressure loads predicted with original water film model are underestimated due to the absence of film breakup, rivulets and shear stress model. The sensitivity analyses reveal that the contact angle as well as hysteresis phenomenon play a significant role in film cooling. The results of sensitivity studies also indicate that the injection rate strategy affects strongly the containment pressure peak. Moreover, film cooling with the new water film model is also implemented in this work in the Generic Containment. The pressure load has been reduced significantly by means of film cooling. Similar effect of contact angle on the results is obtained for Generic Containment as for AP1000.

# 6  SUMMARY AND CONCLUSIONS

In the present work, the characteristics and the evolutionary process of a falling film have been investigated. By reviewing the literature of theoretical studies and experiments, the behavior of falling film on the containment is divided into several stages. Models simulating each stage have been proposed and evaluated and based on which, an integrated water film model is introduced.

Thereafter, this integrated model has been adapted to the lumped parameter code and then implemented into the containment code COCOSYS. This new integrated model enables the code to capture phenomena which are not considered before in the original film model including the behaviors of film breakup and generation of rivulets; the change of coverage rate and the development of rivulets; the change of the velocity distribution as well as film thickness due to the interfacial shear stress created by the countercurrent gas flow. The process of hysteresis of rivulets is also taken into account in the modified film model of COCOSYS.

Validation and assessment of the new integrated model is carried out stage by stage on the basis of existing test results and experimental observations.

With the lumped parameter code COCOSYS, the developed water film model is applied to evaluate the performance of PCCS film cooling which is employed in the AP1000 containment. The new model also helps to optimize the water flow rate of PCCS over time. Finally, the modified version of COCOSYS is used for the European Generic containment to study the feasibility and performance of PCCS for this typical containment.

The most important conclusions of the current work are summarized as follows:

The theoretical study of the current work reveals that most of drag force models, especially those derived from pipe experiments of small scale, tend to overestimate the effect of shear stress on a vertical plate. Whereas, based on Mayinger's drag force model, the film thickness on the containment shell under countercurrent air flow is numerically calculated and the predictions agrees well with the experimental data.

In addition, the critical film thickness, which is calculated with MTE principle, is underestimated with the Nusselt's velocity assumption. The deviation is resulted by the change of velocity distribution due to surface waves. Accordingly, by employing Yu's semi-empirical coefficients, the film critical state is calculated by means of MTE principle and it gives better prediction.

Moreover, it is suggested that the countercurrent gas doesn't significantly increase the critical thickness for breakup. Therefore, the contribution of interfacial shear stress can be neglected in predicting the critical state of fully covered film, especially for the

PCCS vertical channel, where the countercurrent air velocity is as low as about 3 m/s.

According to the results of the applications, conclusions can be drawn that the original film model tends to underestimate the pressure loads due to the absence of film breakup, rivulets and shear stress model.

The sensitivity analyses reveal that the contact angle as well as hysteresis phenomenon, which are not considered in the original version of the code, play a significant role in PCCS film cooling. The advancing contact angle of the rivulets is revealed to be a decisive factor for the peak pressure while the retreating contact angle is influential in the long term cooling.

The results of sensitivity studies also suggested the strategy to optimize the injection rate of PCCS. The cooling efficiency of PCCS can be optimized by increasing the PCCS injection rate initially and reducing the flow rate during the late phase, without changing the water inventory in the PCCS storage tank.

Moreover, cooling is also implemented in this work film in the Generic Containment. The PCCS cooling strategy is proven to be effective in restricting the pressure load and with the modified model, similar trend as that of AP1000 has been observed by varying contact angles in the simulations of Generic Containment.

It can be inferred according to the study that the ideal situation is that the water film is reaching the status of complete dry out at the very bottom of the containment. Too large PCCS flow rates may lead to a large film thickness and in such case water could pass the bottom without evaporation and the limited water in the storage tank cannot be sufficiently utilized. Too small PCCS injection rate of water, on the other hand, although being completely evaporated before it reaches the bottom of containment, may result in an inadequate cooling and therefore cannot remove enough heat to restrict the containment pressure. When the PCCS delivery rate is getting close to the ideal condition, the considerations in the modified models is indispensable as the film thickness at the bottom is extremely thin and the film breakup or rivulet flow will take place.

As outlook for the future works, the following points ought to be mentioned:

The wave on the film and rivulets needs to be studied more in detail. The influences of the amplitude and frequency of the wave to the film instability and velocity distribution should be theoretically studied.

The dynamic features and the range of the contact angle between the water and the particular material of the containment needs to be researched.

The features of falling film on the heated substrate needs to be investigated theoretically and experimentally. The film model ought to be further modified by taking into account all these effects.

Test results of large scale experiments should be used in the future so as to evaluate and validate the modified film mode.

# Bibliography

1 Matzie R A, Worrall A. The AP1000 reactor-the nuclear renaissance option[J]. Nuclear Energy, 2004, 43(1): 33-45.

2 Cummins W E, Corletti M M, Schulz T L. Westinghouse AP1000 advanced passive plant[C]//Proceedings of ICAPP '03, Cordoba, Spain, May 4-7.

3 Broxtermann P. Simulation passiver Kühlsysteme des Sicherheitsbehälters. PhD thesis, RWTH Aachen University, 2013.

4 Westinghouse, L. L. C. Westinghouse AP1000 Design Control Document. Westinghouse Electirc Company LLC, 2008.

5 Yan G, Ye C. Passive safety systems of advanced nuclear power plant: AP1000[C]//18th International Conference on Nuclear Engineering. American Society of Mechanical Engineers. Xi'an, China, 17–21 May 2010. Paper no. ICONE18-29521.

6 Klein-Heßling W. COCOSYS V2. 4 User's Manual[J]. COCOSYS V2. 4 Program Reference Manual, 2009.

7 Bergeron K, Cole Jr R, Elsbemd A, et al. Progress on the MELCOR Code[C]. NUREG/CP-0149, Proceedings of the USNRC Twenty-Third Water Reactor Safety Information Meeting, US Nuclear Regulatory Commission, Washington, DC, 1996.

8 Povilaitis M, Urbonavičius E, Rimkevičius S. Modeling of atmosphere stratification in containments of nuclear power plants using lumped-parameter code[J]. Nuclear Engineering and Design, 2011, 241(8): 3111-3120.

9 Klauck M, Beck S, Allelein H J, et al. Generic Containment: Detailed comparison of containment simulations performed on plant scale[J]. Annals of Nuclear Energy, 2014, 74: 165-172.

10 Blocken B, Derome D, Carmeliet J. Rainwater runoff from building facades: a review[J]. Building and Environment, 2013, 60: 339-361.

11 Sun, J. G., W. T. Sha, and Y. S. Chen. Development of liquid-film tracking models for analysis of AP-600 passive containment cooling system. No. ANL/MCT/CP--78784. Argonne National Lab., IL (United States), 1993.

12 Yu Y. Experimental and Numerical Study on Film Flow Behavior on Large Scale Flat Plate, PhD thesis, Shanghai Jiao Tong University, 2012.

13 Hartley D E, Murgatroyd W. Criteria for the break-up of thin liquid layers flowing isothermally over solid surfaces[J]. International Journal of Heat and Mass Transfer, 1964, 7(9): 1003-1015.

14 Doniec A. Flow of a laminar liquid film down a vertical surface[J]. Chemical engineering science, 1988, 43(4): 847-854.

15 Doniec A. Laminar flow of a liquid rivulet down a vertical solid surface[J]. The Canadian Journal of Chemical Engineering, 1991, 69(1): 198-202.

16 El-Genk M S, Saber H H. Minimum thickness of a flowing down liquid film on a vertical surface[J]. International Journal of Heat and Mass Transfer, 2001, 44(15): 2809-2825.

17 Saber H H, El-Genk M S. On the breakup of a thin liquid film subject to interfacial shear[J]. Journal of Fluid Mechanics, 2004, 500: 113-133.

18 Aiello G, Ciofalo M. Natural convection cooling of a hot vertical wall wet by a falling liquid film[J]. International Journal of Heat and Mass Transfer, 2009, 52(25): 5954-5961.

19 Gauntt R O, Cole R K, Erickson C M, et al. MELCOR Computer Code Manuals, Vol. 1: Primer and Users' Guide, Version 1.8. 5 May 2000[R]. NUREG/CR-6119.

20 Nusselt N, Die Oberflachenkondensation des wsserdanofes, Zeit. Ver. D. Ing. [J] 60: 541-569, 1916.

21 Gajewski, A., 2008. Contact angle and rivulet width hysteresis on metallic surfaces. Part I: With heated surface. Int. J. Heat Mass Transfer 51 (25), 5762–5771.

22 J. Kern, Untersuchungen u ̈ber die Hydrodynamik der Rinnsal, Dissertation, Technische Universit ät Berlin, 1970.

23 J. Kern; Zur Hydrodynamik der Rinnsale. Verfahrenstechnik, 3 (1969), pp. 425–430.

24 Al-Khalil K M, KEITH T G J R, de Witt K J. Hydrodynamic and thermal analysis of rivulet flow down a vertical solid surface[J]. International Journal of Numerical Methods for Heat & Fluid Flow, 1991, 1(1): 63-76.

25 Bentwich M, Glasser D, Kern J, et al. Analysis of rectilinear rivulet flow[J]. AIChE Journal, 1976, 22(4): 772-779.

26 Shi M G, Mersmann A. Effective interfacial area in packed columns[J]. German chemical engineering, 1985, 8(2): 87-96.

27 Shi M G, Mersmann A. Effektive Austauschfl äche in F üllk örperkolonnen[J]. Chemie Ingenieur Technik, 1984, 56(5): 404-405.

28 Rocha J A, Bravo J L, Fair J R. Distillation columns containing structured packings: a comprehensive model for their performance. 1. Hydraulic models[J]. Industrial & engineering chemistry research, 1993, 32(4): 641-651.

29 Rocha J A, Bravo J L, Fair J R. Distillation columns containing structured packings: a comprehensive model for their performance. 2. Mass-transfer model[J]. Industrial & engineering chemistry research, 1996, 35(5): 1660-1667.

30 Bankoff S G. Minimum thickness of a draining liquid film[J]. International Journal of Heat and Mass Transfer, 1971, 14(12): 2143-2146.

31 Mikielewicz J, Moszynskl J R. Minimum thickness of a liquid film flowing vertically down a solid surface[J]. International Journal of Heat and Mass Transfer, 1976, 19(7): 771-776.

32 Towell G D, Rothfeld L B. Hydrodynamics of rivulet flow[J]. AIChE Journal, 1966, 12(5): 972-980.

33 Yu Y Q, Cheng X. Three-dimensional simulation on behavior of water film flow with and without shear stress on water–air interface[J]. International Journal of Heat and Mass Transfer, 2014, 79: 561-572.

34 Moran K, Inumaru J, Kawaji M. Instantaneous hydrodynamics of a laminar wavy liquid film[J]. International Journal of Multiphase Flow, 2002, 28(5): 731-755.

35 Park C D, Nosoko T. Three-dimensional wave dynamics on a falling film and associated mass transfer[J]. AIChE Journal, 2003, 49(11): 2715-2727.

36 Nosoko T, Yoshimura P N, Nagata T, et al. Characteristics of two-dimensional waves on a falling liquid film[J]. Chemical Engineering Science, 1996, 51(5): 725-732.

37 Chang H. Wave evolution on a falling film[J]. Annual review of fluid mechanics, 1994, 26(1): 103-136.

38 Ambrosini W, Forgione N, Oriolo F. Statistical characteristics of a water film falling down a flat plate at different inclinations and temperatures[J]. International Journal of Multiphase Flow, 2002, 28(9): 1521-1540.

39 Jiang,Z.And Yan,W.,Experimental Studies on Surface Wave Characteristics of Free-Falling Liquid Films.Heat Transfer Science and Technology 1996,Proceedings of the 4th International Symposium on Heat Transfer,Edited by Wang B.,Higher Education Press,Beijing,200-205,1996.

40 Takahama H, Kato S. Longitudinal flow characteristics of vertically falling liquid films without concurrent gas flow[J]. International Journal of Multiphase Flow, 1980, 6(3): 203-215.

41 Brauer, G. H. 1956. "Strömung und Wärmeübergang bei. Rieselfilmen." VDI (Ver.Deut. Ingr.))Forschungsheft 457,. VDI-Verlag GMBH, Düsseldorf, Germany

42 Karapantsios T D, Paras S V, Karabelas A J. Statistical characteristics of free falling films at high Reynolds numbers[J]. International journal of multiphase flow, 1989, 15(1): 1-21.

43 Tills J, Notafrancesco A, Phillips J. Application of the MELCOR code to design basis PWR large dry containment analysis[R]. SAND2009-2858, Sandia National Laboratories, Albuquerque, New Mexico, 2009.

44 Kang Y M, Park G C. An experimental study on evaporative heat transfer coefficient and applications for passive cooling of AP600 steel containment[J]. Nuclear engineering and design, 2001, 204(1): 347-359.

45 FM White, Viscous Fluid Flow, McGraw-Hill, New York (1974).

46 Moeck E O, Stachiewicz J W. A droplet interchange model for annular-dispersed, two-phase flow[J]. International Journal of Heat and Mass Transfer, 1972, 15(4): 637-653.

47 Grolmes, M.A., Lambert, G.A., Fauske, H.K., 1974. Flooding in vertical tubes. Inst. Chem. Eng. Symp. Ser. 38, 1–15.

48 Drosos E I P, Paras S V, Karabelas A J. Counter-current gas–liquid flow in a vertical narrow channel—Liquid film characteristics and flooding phenomena[J]. International journal of multiphase flow, 2006, 32(1): 51-81.

49 Wallis G B. Phenomena of liquid transfer in two-phase dispersed annular flow[J]. International Journal of Heat and Mass Transfer, 1968, 11(4): 783-785.

50 Zapke, A., Kröger, D.G., 2000. Countercurrent gas–liquid flow in inclined and vertical ducts − I: Flow patterns, pressure drop characteristics and flooding. Int. J. Multiphase Flow 26 (9), 143.

51 Bharathan D, Wallis G B. Air-water countercurrent annular flow[J]. International Journal of Multiphase Flow, 1983, 9(4): 349-366.

52 Vijayan M, Jayanti S, Balakrishnan A R. Effect of tube diameter on flooding[J]. International journal of multiphase flow, 2001, 27(5): 797-816.

53 Fore L B, Beus S G, Bauer R C. Interfacial friction in gas–liquid annular flow: analogies to full and transition roughness[J]. International journal of multiphase flow, 2000, 26(11): 1755-1769.

54 Maharudrayya S, Jayanti S. Investigation of postflooding conditions in countercurrent gas–liquid flow[J]. AIChE journal, 2002, 48(2): 212-220.

55 Stephan M, Mayinger F. Experimental and analytical study of countercurrent flow limitation in vertical gas/liquid flows[J]. Chemical engineering & technology, 1992, 15(1): 51-62.

56 Xu Y Y, Paschke S, Repke J U, et al. Portraying the Countercurrent Flow on Packings by Three-Dimensional Computational Fluid Dynamics Simulations[J]. Chemical engineering & technology, 2008, 31(10): 1445-1452.

57 FUKANO T, ITO A, ODAWARA H, et al. Liquid Films Flowing Concurrently with Air in Horizontal Duct: 5th Report, Interfacial shear stress[J]. Bulletin of JSME, 1985, 28(244): 2294-2301.

58 Hobler, T. 1964 Minimum surface wetting (in Polish). Chemia Stosow. 2B, 145

59 Westinghouse Electric Company, 2004, March. WCAP-15862, WGOTHIC Application to AP600 and AP1000, (Non-proprietary), Revision 1, Pittsburgh.

60 Chung, J.C., Bankoff, S.G., 1980. Initial breakdown of a heated liquid film in concurrent two-component annular flow: II. Rivulet and dry patch models. Chem. Eng. Commun. 4 (4–5), 455–470.

61 Roy R P, Jain S. A study of thin water film flow down an inclined plate without and

with countercurrent air flow[J]. Experiments in fluids, 1989, 7(5): 318-328.

62 Huang X G, Yang Y H, Hu P. Experimental study of falling film evaporation in large scale rectangular channel[J]. Annals of Nuclear Energy, 2015, 76: 237-242.

63 Woodcock J, Andreychek T S, Conway L. WGOTHIC Application to AP600 and AP1000 (WCAP-15862, Class3)[J]. PA: Westinghouse Electric Company LLC, 2004.

64 Andreani M, Paladino D, George T. Simulation of basic gas mixing tests with condensation in the PANDA facility using the GOTHIC code[J]. Nuclear Engineering and Design, 2010, 240(6): 1528-1547.

65 Povilaitis M, Urbonavičius E, Rimkevičius S. Modeling of atmosphere stratification in containments of nuclear power plants using lumped-parameter code[J]. Nuclear Engineering and Design, 2011, 241(8): 3111-3120.

66 Allelein H J, Arndt S, Klein-Heßling W, et al. COCOSYS: status of development and validation of the German containment code system[J]. Nuclear Engineering and Design, 2008, 238(4): 872-889.

67 Klein-Hessling, W., 2000. COCOSYS V1. 2 Program Reference Manual. GRS-P-3/2. Gesellschaft fur Anlagen-und Reaktorsicherheit (GRS) mbH.

68 Schmuki P, Laso M. On the stability of rivulet flow[J]. Journal of Fluid Mechanics, 1990, 215: 125-143.

69 Dukler, A.E., Bergelin, O.P., 1952. Characteristics of flow-in falling liquid films. Chem. Eng. Prog. 48 (11), 557–563.

70 Hopf, L., 1910. Turbulenz bei einem Flusse. Ann. Phys. 32, 777–808.

71 Roy R P, Jain S. A study of thin water film flow down an inclined plate without and with countercurrent air flow[J]. Experiments in fluids, 1989, 7(5): 318-328.

72 Zhou D W, Gambaryan-Roisman T, Stephan P. Measurement of water falling film thickness to flat plate using confocal chromatic sensing technique[J]. Experimental Thermal and Fluid Science, 2009, 33(2): 273-283.

73 Xu Y Y, Paschke S, Repke J U, et al. Computational Approach to Characterize the Mass Transfer between the Counter-Current Gas-Liquid Flow[J]. Chemical engineering & technology, 2009, 32(8): 1227-1235.

74 Hoffmann A, Ausner I, Wozny G. Detailed investigation of multiphase (gas–liquid and gas–liquid–liquid) flow behaviour on inclined plates[J]. Chemical Engineering Research and Design, 2006, 84(2): 147-154.

75 Baehr H D, Stephan K. Wärme-und Stoffübertragung[M]. Berlin: Springer, 1994.

76 Lan H, Wegener J L, Armaly B F, et al. Developing laminar gravity-driven thin liquid film flow down an inclined plane[J]. Journal of Fluids Engineering, 2010, 132(8): 081301.

77 Lin, C., Yu, Z., Ou, Y., Chengge, L., Zusheng, Y., Yangyu, O., 2008. Passive Safety Advanced Nuclear Power Plant AP1000. Atomic Energy Press, Beijing, 2000, ISBN-

10:7502242279; ISBN-13: 978-7502242275.

78 Schwarz S.: "Simulation of free jets and buoyant plumes". Gesellschaft für Anlagen- und Reaktorsicherheit (GRS), München, Juli 2004.

S. Schwarz Hints and recommendations, Simulation of free jets and buoyant plumes. COCOSYS User Forum, July 2004. Internet address on April 22, 2005: http://domino.grs.de/cocosys/userforumcocosys.nsf?OpenDatabase

79 Povilaitis M, Urbonavičius E, Rimkevičius S, et al. Sensitivity and uncertainty analysis of atmosphere stratification modelling in MISTRA using lumped-parameter code COCOSYS[J]. Nuclear Engineering and Design, 2013, 265: 108-119.

80 Klauck M, Beck S, Allelein H J, et al. Generic Containment: Detailed comparison of containment simulations performed on plant scale[J]. Annals of Nuclear Energy, 2014, 74: 165-172.

81 Yaminsky V V. Molecular mechanisms of hydrophobic transitions[J]. Journal of adhesion science and technology, 2000, 14(2): 187-233.

82 Whyman G, Bormashenko E, Stein T. The rigorous derivation of Young, Cassie–Baxter and Wenzel equations and the analysis of the contact angle hysteresis phenomenon[J]. Chemical Physics Letters, 2008, 450(4): 355-359.

83 Ni, Qi, et al. "Studying of Contact Angle Friction and Contact Angle Hysteresis (CAH) Though Force Measurements." ASME 2012 International Mechanical Engineering Congress and Exposition. American Society of Mechanical Engineers, Nov 9-15 Houston, Texas, 9-15 Nov., 2012.

84 Blake T D. The physics of moving wetting lines[J]. Journal of Colloid and Interface Science, 2006, 299(1): 1-13.

85 Eral H B, Oh J M. Contact angle hysteresis: a review of fundamentals and applications[J]. Colloid and polymer science, 2013, 291(2): 247-260.

86 Ataki A. Wetting of structured packing elements-CFD and experiment, PhD thesis, TU Kaiserslautern, 2006.

87 Yu Y Q, Cheng X. Experimental study of water film flow on large vertical and inclined flat plate[J]. Progress in Nuclear Energy, 2014, 77: 176-186.

88 Yu Y Q, Wei S J, Yang Y H, et al. Experimental study of water film falling and spreading on a large vertical plate[J]. Progress in Nuclear Energy, 2012, 54(1): 22-28.